THESIS FOR THE DEGREE OF DOCTOR OF PHILOSOPHY

High Temperature Corrosion of FeCrAl Alloys in Biomass- and Waste-fired Boilers

The Influence of Alloying Elements in Prediction and Mitigation of Corrosion in Harsh Environments

Johan Eklund

CHALMERS

Department of Chemistry and Chemical Engineering

CHALMERS UNIVERSITY OF TECHNOLOGY

Gothenburg, Sweden 2020

High Temperature Corrosion of FeCrAl Alloys in Biomass- and Waste-fired Boilers
The Influence of Alloying Elements in Prediction and Mitigation of Corrosion in Harsh Environments
Johan Eklund
ISBN 978-91-7905-394-9

Doktorsavhandlingar vid Chalmers tekniska högskola
Ny serie nr 4861
ISSN 0346-718X

Department of Chemistry and Chemical Engineering
Chalmers University of Technology
SE-412 96 Gothenburg
Sweden
Telephone + 46 (0)31-772 1000

Cover: Illustration of the influence of Cr and Si content on the corrosion resistance of FeCrAl alloys in laboratory set-up and in a waste-fired boiler.
Upper left: SEM-BSE image of Fe10Cr4Al after exposure in lab, Bottom left: SEM-BSE images of Fe10Cr3Al after exposure in waste-fired boiler, Middle left and right: Schematic illustrations of the spinel crystal structure, Upper right: SEM-BSE image of Fe15Cr3Al2Si after exposure in lab, Bottom right: SEM-BSE images of Fe15Cr3Al2Si after exposure in waste-fired boiler, Upper middle: Schematic of the thermobalance set-up, Bottom middle: Schematic illustration of a BFB boiler (produced by Jesper Liske [2])
Background: Taken from https://ypard.net/zh-hans/2018-01-19/biomass-energy-influence-environmental-footprint (CC-BY)

Printed by Chalmers Digitaltryck
Göteborg, Sweden 2020

High Temperature Corrosion of FeCrAl Alloys in Biomass- and Waste-fired Boilers
The Influence of Alloying Elements in Prediction and Mitigation of Corrosion in Harsh Environments

Johan Eklund
Department of Chemistry and Chemical Engineering
Chalmers University of Technology

Abstract

Combustion of biomass and waste for heat and power production is an alternative to fossil fuels and can be an important step towards a more sustainable future. The electrical efficiency of the fuel-to-energy conversion process is largely dependent on the steam parameters (temperature and pressure) of the combined heat and power (CHP) plants. Meanwhile, the boiler environment when utilizing these fuels is complex and can be characterized by high levels of corrosive species, such as water vapor and alkali chlorides. These species contribute to highly corrosive conditions that results in rapid material degradation of boiler components and limits the operating temperature.

Stainless steels are commonly used to reduce material degradation in these types of corrosive environments because of their high temperature corrosion resistance. This is attributed to their ability to form a protective chromium-rich oxide scale. However, in the highly corrosive environment of biomass- and waste-fired boilers these scales have been found to rapidly break down and result in the formation of less protective iron-rich oxide scales. The present thesis elucidates the potential of improving the corrosion resistance by introducing alumina-forming alloys (FeCrAl alloys) and/or improving the properties of the fast-growing oxide scales formed after breakaway oxidation.

The results show that the oxidation process can be divided into a primary and a secondary corrosion regime, i.e. the corrosion behavior before and after breakaway oxidation. This concept was utilized when investigating the influence of alloying elements on the corrosion resistance of FeCr(Al) model and coatings in a broad range of corrosive environments. Cr, Al and Si was found to significantly influence the corrosion behavior of FeCr(Al) alloys in both the primary and secondary corrosion regime. However, the criteria for a high corrosion resistance differed for the two corrosion regimes. HVAF-sprayed and overlay-welded coatings demonstrated the potential of providing high corrosion resistance within the primary and secondary corrosion regime, respectively. The applicability of the findings was shown to extend from simplified laboratory environments to the complex conditions of a waste-fired boiler.

The novel insights, presented in this work, contribute to new perspectives on high temperature corrosion resistance, which are valuable in material development and corrosion prediction in harsh environments.

Keywords: High Temperature Corrosion, Breakaway Oxidation, Biomass, Waste, FeCrAl alloys, Silicon, Coatings, HVAF, Overlay Welding

List of publications

The thesis is based on the following papers:

Paper I:
A. Persdotter, J. Eklund, J. Liske, T. Jonsson
Beyond breakaway corrosion - Influence of Cr, Ni and Al on corrosion of Fe-based alloys at 600 °C
Corrosion Science, Volume 177, 2020, Article 108961
https://doi.org/10.1016/j.corsci.2020.108961

Paper II:
J. Eklund, A. Persdotter, I. Hanif, S. Bigdeli, T. Jonsson
Secondary Corrosion Protection of FeCr(Al) model alloys at 600 ° C– The influence of Cr and Al after breakaway corrosion
(Manuscript)

Paper III:
J. Eklund, B. Jönsson, A. Persdotter, J. Liske, J-E. Svensson and T. Jonsson
The influence of silicon on the corrosion properties of FeCrAl model alloys in oxidizing environments at 600 °C
Corrosion Science, Volume 144, 2018, Pages 266-276
https://doi.org/10.1016/j.corsci.2018.09.004.

Paper IV:
V. Asokan, J. Eklund, S. Bigdeli, T. Jonsson
The influence of Si on the primary protection of lean FeCrAl model alloys in O_2 and O_2+H_2O at 600 °C – A microstructural investigation
(Submitted 2020, Corrosion Science)

Paper V:
J. Eklund, I. Hanif, T. Jonsson
High temperature corrosion behaviour of FeCrAlSi alloys in the presence of water vapour and KCl at 600 °C – The influence of Cr content
(Manuscript)

Paper VI:
J. Eklund, J. Phother-Simon, E. Sadeghimeresht, S. Joshi, J. Liske
High-Temperature Corrosion of HVAF-Sprayed Ni-Based Coatings for Boiler Applications
Oxidation of Metals, Volume 91, 2019, Pages 729–747
https://doi.org/10.1007/s11085-019-09906-0

Paper VII:
J. Eklund, M. Dolores Paz, B. Jönsson, J. Liske, J-E. Svensson, T. Jonsson
Field exposure of FeCrAl model alloys in a waste-fired boiler at 600°C: The influence of Cr and Si on the corrosion behaviour
Materials and Corrosion, Volume 70 (8), 2019, Pages 1476-1485
https://doi.org/10.1002/maco.201810618

Statement of the author's contribution

With the exception of Paper I and Paper IV, I was the main author of all appended papers and responsible for the scientific writing of these. I performed the majority of the sample preparation, corrosion tests and SEM analysis in the appended papers.

In Paper II, Amanda Persdotter performed TEM sample preparation and TEM analysis. In Paper III Amanda Persdotter performed FIB preparation and imaging of sample cross sections. The TEM preparation and analysis in Paper IV was performed by Dr Vijay Asokan. The EBSD analysis and TEM preparation and analysis in Paper V was performed by Dr Imran Hanif.

The HVAF-sprayed coatings in Paper VI were produced at University West under the responsibility of Esmaeil Sadeghi and Shrikant Joshi. Esmaeil Sadeghi was also responsible for the sample preparation of the coatings. Me and Julien Phother performed equal parts of the experimental work in Paper II.

The probe exposures in Paper VII was performed by both me and Dr Maria Dolores Paz.

Related work and technical reports not included in this thesis

Sadeghimeresht E, Eklund J, Phother Simon J, Liske J, Markocsan N, Joshi S.
Effect of water vapor on the oxidation behavior of HVAF-sprayed NiCr and NiCrAlY coatings
Materials and Corrosion, Volume 69, 2018, Pages 1431-1440.

M. A. Olivas-Ogaz, J. Eklund, J.-E. Svensson, J. Liske and T. Jonsson
Microstructural Study of the Influence of KCl and HCl on Preformed Corrosion Product Layers on Stainless Steel
Oxidation of Metals, Volume 87, 2017, Pages 801-811.

M. A. Olivas-Ogaz, J. Eklund, A. Persdotter, M. Sattari, J. Liske, J-E. Svensson, T. Jonsson
The influence of oxide scale microstructure on KCl(s) induced corrosion of a low-alloyed steel at 400 °C
Oxidation of Metals, Volume 91, 2018, pages 291–310.

L. Mikkelsen, T. Jonsson, L. Paz, J. Eklund, J. Liske, B Jönsson, N. Israelsson, S. Selin, J. Hernblom, J. Högberg, J. Nockert Olovsjö
Increased steam temperature in grate fired boilers – Steamboost
KME report 2018

T. Sand, A. Edgren, C. Geers, V. Asokan, J. Eklund, T. Helander, J.-E. Svensson, L.-G. Johansson
Exploring the silicon effect on the high temperature corrosion behaviour of FeCrAl alloys in humid air
Submitted to Oxidation of Metals, 2020

Acknowledgements

First of all I would like to thank my supervisors, Professor Jan-Erik Svensson, associate professor Jesper Liske and associate professor Torbjörn Jonsson for introducing me to the amazing field of high temperature corrosion and for giving me the opportunity to embark on the adventure that these past five years have been. I would also like to thank them for all their support, advice and inspiring discussions.

In addition, I would like to thank Sandra Gustafson, Anna Oskarsson and Christina Andersson for assistance with administrative matters. I would also like to thank Esa Väänänen, Torbjörn Jönsson and Erik Brunius for technical support regarding laboratory systems and material preparation. Further, I would like to thank Mohammad Sattari, Anders Kvist and Stefan Gustafsson for technical support regarding microscopy.

Furthermore, I would also like to acknowledge the High Temperature Corrosion Centre (HTC), the Consortium for Material Technology regarding Thermal Energy Processes (KME), the Swedish Energy Agency (SEA), Västra Götalandsregionen as well as their member companies for supporting and funding these interesting projects that I have been working with. Special thanks to Kanthal, for producing the wide range of alloys that the majority of this of this work is based on. Many thanks to Bo Jönsson for all the advice and interesting discussions.

Moreover, I would like to thank Esmaeil Sadeghi, Shrikant Joshi and Nicolaie Markocsan at University West for the collaboration and for producing the HVAF-sprayed coatings used in this work.

Special thanks to Andrea Olivas for introducing me to the joy of sample preparation in the beginning of my PhD, which allowed me to perfect the craft 😉I would also like to take the opportunity to thank my colleague's Dr Imran Hanif, Dr Vijay Asokan and Amanda Persdotter for all the help with detailed microstructural analysis included in this work. Many thanks to Loli Paz for all the help involving field studies. I also want to thank all my other colleagues at Environmental Inorganic Chemistry for creating a great work environment with a lot of laughs and fun activities both within and outside of work and for always being open to discussing and helping with work-related issues.

Finally, I would like to thank my parents for supporting me and my decisions at all times. Special thanks to my wife, MyLan Truong, for always being there for me when things get tough, cheering me up when I'm down and for motivating me to get back up on my feet. You are my light when everything else seems dark.

Table of Contents

1 Introduction

Since around 1960, the average global temperature has been increasing at an alarming rate, see Figure 1a [1]. As a result of this, glaciers and polar ice are melting, sea levels are rising [3] and extreme weather such as heat waves, droughts, floods and hurricanes has increased [4]. Climate change is posing a serious threat to the biodiversity on our planet as well as human health. There is strong evidence that most of the rise in temperature is caused by increased levels of greenhouse gases in the atmosphere, caused by human activities [5-7]. The main greenhouse gases are carbon dioxide (CO_2), methane (CH_4), nitrous oxide (N_2O) and fluorinated gases. Among these, carbon dioxide is the most abundant. The increase in the average global temperature has been shown to correlate with the increased amount of carbon dioxide in the atmosphere (see Figure 1b), which increased drastically around 1960.

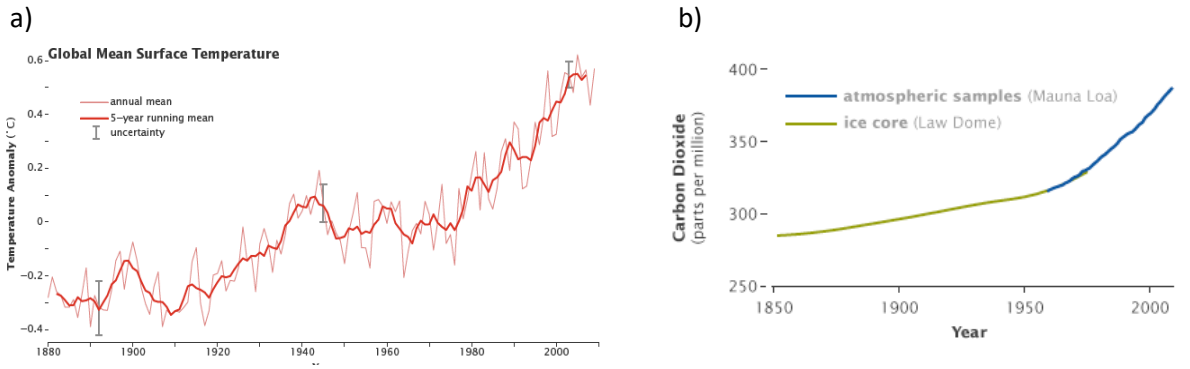

Figure 1: (a) Graph showing the increase in the global mean surface temperature and b) a graph showing the increase in the carbon dioxide concentration in the atmosphere [1].

The increase in pollution from CO_2 is mainly a result of the combustion of fossil fuels but also due to deforestation, which has reduced our planets ability to absorb CO_2. Fossil fuels are primarily used in automotive vehicles, in heat production for houses and for electricity production in power plants. Concurrently, the need for electricity is becoming larger in today's society due to the increased amount of industrial processes and more widespread use of electrical devices along with the electricity these devices demand. The substitution of fossil fuel-based vehicles with electrical vehicles in recent years has also led to an increased need for electricity, which makes electricity production even more crucial. In addition to the environmental impacts, fossil fuels are of limited supply and are not renewable. It is therefore of utmost importance to develop renewable and more CO_2-neutral energy sources to substitute for fossil fuels.

Biomass and certain types of waste are examples of alternative fuels that are both renewable and relatively CO_2 neutral. These can be combusted in a Combined Heat and Power (CHP) boiler to produce steam for use in turbines which subsequently generates electricity as and/or warm water for district heating. Negative CO_2-emissions would be possible to achieve by combining a biomass-fired boiler with a Carbon Capture and Storage (CCS) process, called BECCS (Bio Energy Carbon Capture and Storage). The use of biomass and waste as fuels has already been implemented in Sweden and other Scandinavian countries. However, this has been shown to result in major technical challenges in comparison to the more common coal-fired boilers. These challenges include high maintenance costs and a reduction in the electrical efficiency of the boiler process.

Biomass and waste generally contain high amounts of alkali- and chlorine containing species as well as a rather high amount of water compared to fossil fuels. When combusted, these species are released in the boiler, which results in a complex and severely corrosive environment. This can lead to high

material degradation of critical metallic components in the boiler, which significantly reduces their lifetime. The superheaters in the boiler, exhibits higher material temperatures than most components of the boiler, which results in an even more corrosive environment. To increase the lifetime and reduce maintenance costs for the superheaters, boiler operators have been forced to reduce the steam temperature. However, the electrical efficiency of the boiler is reduced in doing so, which decreases electrical output, and thus the substitution for fossil fuels is challenging. Since the composition of biomass and waste is not always the same, and the ratio between biomass and waste varies, the harshness of the boiler environment normally fluctuates with time.

Low-alloyed steels and stainless steels are commonly used for superheaters because of their good mechanical properties and fabricability along with the corrosion properties of the latter. However, in order to facilitate an increase in steam temperature to improve electrical efficiency, more corrosion resistant materials are needed. Stainless steels generally contain about 12% Cr in order to form a protective Cr-rich oxide layer. However, in the complex environment of a biomass- and/or waste-fired boiler that contains high amounts of alkali salts and high levels of water vapor, the Cr-rich oxide scale has been found to break down [8-11] through different corrosion mechanisms.

Alumina-forming alloys, such as FeCrAl alloys, are commonly used at high temperatures (above 900 °C) in various different applications, including ignitors, furnace rollers and electrical elements of gas burners. These alloys have been found to exhibit excellent corrosion resistance in environments containing oxygen and water vapor at temperatures up to 1300 °C [12-14]. The high oxidation resistance of FeCrAl alloys at higher temperatures is attributed to the formation of an α-alumina layer. The α-alumina scale is highly protective and slow-growing because of its high degree of stoichiometry. The vapor pressures of the volatile species over α-alumina are much lower than those over chromia in the presence of water vapor. The α-alumina scale has also been found to remain protective in the presence of KCl [15] and other alkali containing compounds. However, at lower temperatures (below 900 °C) the formation rate of α-alumina is significantly slower and thus, transient forms of alumina have often been observed at temperatures as low as 600 °C [16]. These have been reported to contain small amounts of Fe and Cr [17], and therefore, may not be as resistant towards water vapor and alkali containing compounds as the thermodynamically stable form. Thus, in harsh environments, a fast-growing iron-rich oxide scale forms and results in a rapid increase in material degradation.

A recent study has presented a novel approach to the utilization of different material classes (FeCr, FeCrAl, FeCrNi) in both mild and harsh environments [18]. This approach is based on several studies that showed the possibility of altering the protectiveness of both the thin slow-growing oxide scales (chromia/alumina) and the fast-growing iron-rich oxide scales by increasing the amounts of different alloying elements (Cr, Al, Ni, Si etc.) [19-25]. These two types of corrosion protection/behaviors are defined as the primary (chromia/alumina) and secondary (iron-rich oxide) protection/regime. For applications associated with harsh environments, the primary protection of stainless-steel is often impossible to retain during long-term operation. To increase the corrosion resistance, operators may choose an alloy with a better primary protection by increasing the Cr and/or Al content of the alloy. This could extend the incubation time, i.e. the time before breakdown of the primary protection. However, in these types of environments, this generally only has a minor influence on the incubation time and therefore does not significantly increase the lifetime of the component. Considering that the metallic components will be within the secondary corrosion regime during the majority of the operating timespan, choosing an alloy with a better performing secondary protection may be a viable option.

Lifetime predictive tools are of great interest for operators of different types of applications to gage the maintenance costs for different types of components and how changing a material may influence

the material degradation. For applications exhibiting harsh environments in which the mechanisms of material degradation are complex, predicting the lifetime of a component may be difficult. However, the novel approach, in which the corrosion process is separated into different regimes, is of great importance in the future development of a lifetime predicting tool.

While increasing the amounts of certain alloying elements can significantly improve both the primary and secondary protection of stainless steels, such an increase is also associated with several drawbacks. The cost of the material is one important aspect that can be highly influenced by certain alloying elements, Ni being one example. Certain elements may also influence the mechanical properties such as creep strength, ductility and machinability (elevated amount of Cr, Al and Si) [26-28]. It is therefore important to find a balance between good corrosion properties, good mechanical properties, and price.

A way to avoid the difficulties regarding mechanical properties as well as the high cost that can be associated with highly alloyed steels is to use coatings. In this way, both high corrosion resistance and good mechanical properties can be achieved by spraying a highly alloyed coating on a low-alloyed steel as substrate (with good mechanical properties). Since a smaller amount of the expensive alloy is used when applied as a coating, this approach is usually more economically favorable. Previous use of coatings for improved corrosion resistance at high temperatures has encountered problems, such as porosity and poor adherence to the substrate, resulting in failure of the coating. However, new spraying techniques have recently been developed in which denser and more adherent coatings can be achieved [29, 30]. The high velocity air fuel (HVAF) technique is among these. Applying a coating through overlay welding is another viable option which facilitates repairs on-site.

Combining the novel approach of distinguishing between the different corrosion regimes (primary and secondary) of alloys with the recent development in the application of coatings introduces a wide range of opportunities for reducing material degradation in harsh environments. In addition, the novel approach also plays an important role in the future development of a lifetime prediction tool. This study focuses on expanding the knowledge about the influence of certain alloying elements on both primary and secondary protection (but mainly the latter) and the mechanisms behind these effects. The relevance of this novel approach in biomass- and waste-fired boilers is also investigated along with the pros and cons of coatings to gage the possibility of utilizing these in harsh environments.

2 Combustion of biomass and waste for power generation

Combustion of a fuel in a boiler is a widely used concept for generating power and heat. Globally, the majority of fuels are fossil-based, such as coal, but recently, with increasing awareness of the negative effects of greenhouse gases, the less environmentally friendly fuels are being phased out and substituted with renewable and more CO_2-neutral fuels. An example of such fuels are biomass and waste which, similar to coal, can be combusted in a boiler. The design and size of boilers differ (Grate-fired boilers and Fluidized Bed boilers are the most commonly used), but the fundamental concept is the same and is based on converting the energy stored within the fuel into heat energy, which in turn is transformed into mechanical work for generating electricity by using turbines. During the combustion of the fuel, a hot flue gas is produced that heats water that circulates in heat exchangers. As a result of this, the water evaporates but is further heated until it reaches a temperature far above the saturation temperature inside superheaters. Superheated steam is pressurized in a confined space and therefore contains a large amount of internal energy. This is utilized as the steam enters the turbine where the steam can expand, which enables the turbine to drive an electric generator. The low-pressure steam from the turbine is later condensed and can be recycled in the process or used for district heating. This is known as the Rankine cycle, illustrated in Figure 2.

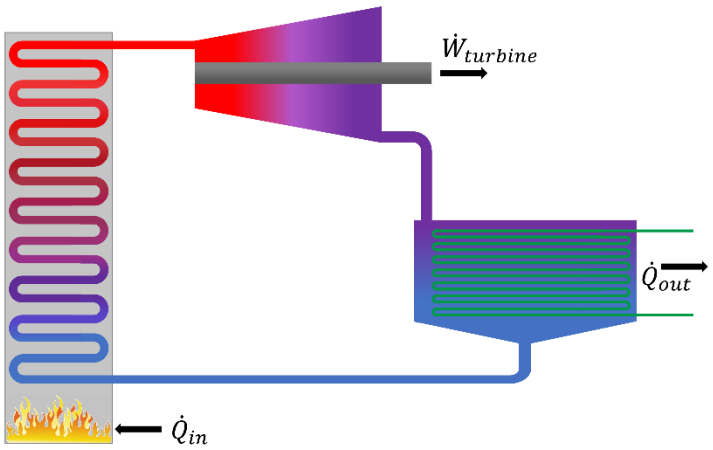

Figure 2: Schematic illustration of the Rankine cycle.

The efficiency of this process is dependent on the temperature and pressure of the superheated steam that enters the turbine [31]. Consequently, the temperature of the steam in the superheaters should be maximized to improve the efficiency of the process. However, as the steam temperature increases, several problems regarding the material of the superheater can occur. Firstly, the mechanical properties of metals in general, such as tensile strength and creep strength, decrease with temperature. Simultaneously, the pressure of the superheated steam increases with increasing temperature, which results in higher requirements on the mechanical properties of the superheater material. Secondly, corrosion reactions occur at a higher rate at higher temperatures, which can result in severe degradation of the material. Combining both good mechanical properties and good corrosion behavior is challenging and finding a balance between these two is crucial. This will be further discussed in chapter 3.

One of the major problems with the combustion of biomass and waste as an alternative to coal is the altered composition of the flue gas. When combusting biomass and waste, the amounts of several corrosive species, such as water vapor, HCl(g), and alkali salts (NaCl and KCl) are significantly increased [32-35]. Thus, in addition to the high temperatures the superheaters are exposed to, the increased corrosiveness of the flue gas results in severe corrosion attacks and rapid material degradation. For this reason, boiler operators are forced to reduce the temperature of the superheated steam, which

consequently reduces the electrical efficiency of the process. Two alternative approaches to reduce the material degradation is changing the fuel composition (for example through sulfur additives [33, 34, 36, 37]) or changing the material of the boiler components. The latter will be discussed in the next chapter.

3 Materials

The material properties required for different applications can vary greatly. Mechanical properties are of utmost importance in load-bearing applications, such as infrastructure. These include mechanical strength, ductility and creep strength. Physical properties, such as electrical conductivity, are essential in applications involving electrical equipment. A material's thermal conductivity is vital to the transportation of heat through high temperature fluids and gases (heat exchangers such as superheaters) in power generating applications. The high temperature corrosion resistance of materials is increasingly important at elevated temperatures to reduce the maintenance costs of the power plant. For some components, such as superheaters, pressure bearing capabilities are crucial as well and a balance between the most important properties must be established. The materials currently in use for superheaters are low-alloyed steel and stainless steels due to the high mechanical strength of the former and the high corrosion resistance of the latter. As described in chapter 2, the environment in a biomass- and waste-fired boiler is highly corrosive, especially in the conditions to which the superheaters are exposed. This generally results in accelerated corrosion for both low-alloyed and stainless steels (because of rapid breakdown of the protective oxide scale). Thus, other material solutions are needed to reduce maintenance costs and increase the electrical efficiency of a boiler. Two alternative material approaches will be described in the following sections.

3.1 FeCrAl alloys

FeCrAl alloys are ferritic iron-based alloys with a body-centered cubic (bcc) crystal structure. Commercial FeCrAl alloys generally contain roughly 20 wt% Cr and 1-5 wt% Al and are most commonly used in high-temperature applications (900-1300 °C), such as ignitors, furnace rollers, heating elements in industrial furnaces. The reason for this is their superior oxidation resistance at higher temperatures due to their ability to form an α-Al_2O_3-layer. α-Al_2O_3 is a highly stoichiometric oxide and is therefore slow growing and highly protective.

The material temperature of the different components in power production applications varies but is generally below 900 °C. This is not necessarily positive since the formation of α-Al_2O_3 below this temperature is very slow. Analysis of FeCrAl alloys after exposure at medium-high temperatures (below 800 °C) have shown transient forms of alumina (γ-, δ- and θ-Al_2O_3) instead, which means that α-Al_2O_3 was not able to form during the limited timespan of the exposure. The transient alumina scale can be protective enough to withstand humid environments and the presence of alkali salts if they have a high enough Al content. However, because the Cr content increases with decreasing temperature, these forms generally do not provide an equally high corrosion resistance as the thermodynamically stable form [12, 17].

Since the reason behind the great corrosion properties of FeCrAl alloys is their ability to form an alumina scale, the high presence of Cr in the alloy may seem confusing. FeAl alloys can also form the same type of protective alumina scale, but they have been shown to experience internal oxidation and nitridation due to the low activity of Al, even at a relatively high temperature (1300 °C) [38]. Increasing the Al content of these alloys reduces the degree of internal oxidation/nitridation but also has negative impacts on the mechanical properties of the alloy, such as fabricability [39] and reduced high-temperature strength. This limits the amount of Al that can be added to the alloy for applications that need good pressure-bearing properties. However, upon the addition of Cr to the FeAl alloy, the amount of Al needed to form an α-Al_2O_3 scale is reduced [40] and thus, so is the issue of internal oxidation/nitridation. In harsh environments at medium-high temperatures, FeCrAl alloys tend to lose their protective scale which results in rapid formation of iron-rich oxide. This generally leads to high material degradation and thus, high maintenance costs. However, recent studies have shown that altering the composition of different alloying elements reduces the growth rate of the iron-rich oxides

scale and thereby improves its corrosion resistance. This introduces a whole new range of opportunities for reducing material degradation in harsh environments. This approach and the potential implementations will be further discussed in Chapter 5.

Even though FeCrAl alloys display promising corrosion resistance at elevated temperatures, their pressure-bearing properties are generally insufficient for integrating them into use in components such as the superheaters in power generation boilers. Increasing the amount of other corrosion resistance enhancing elements, such as Cr and Si, has also been shown to negatively affect the mechanical properties of the alloy, resulting in embrittlement and further negative effects on fabricability (increased deformation resistance and ductile-to-brittle transition temperature (DBBT)) [27, 28, 41]. Decreasing the Al and Cr contents in the alloy to levels at which sufficient mechanical properties are achieved would result in poor corrosion resistance. One viable solution to this problem would be to use a compound tube, which is a tube consisting of an outer and an inner component that are mechanically bonded through hot extrusion. By selecting a corrosion resistant outer component (such as a FeCrAl alloy) and an inner component with good mechanical properties, these properties can be combined. However, the interdiffusion of elements may occur at elevated temperatures between materials of different composition that are in physical contact. The interdiffusion of Al and Cr from the outer component to the inner component during long-term operation may have negative impacts on the mechanical properties of the material, such as embrittlement. Another solution to combining corrosion resistance with good mechanical properties is the use of a coating, which will be described in the following section.

3.2 Coatings

In many applications, utilizing coatings is a good way to protect or add specific surface properties to a material. These kinds of properties can range from functional properties, such as adhesion, wettability and even electrical conductivity, to protective properties, such as wear resistance and corrosion resistance. In this study, coatings were used to increase the corrosion resistance of low-alloyed steels.

Coatings can be applied to a surface in several different ways, depending on the application requirements. The density of the coatings is of utmost importance for corrosion protection. A coating with a low degree of porosity is essential to prevent the underlying substrate from being exposed to the surrounding atmosphere. The state-of-the-art thermal spraying technique HVAF (High Velocity Air-Fuel) has been shown to produce coatings with a low degree of porosity, low oxide content [29, 30] and high bond strengths compared to other thermal spraying techniques. This is because of the much higher particle velocity (1100-1200 m/s) and lower particle temperature (1500 °C) [42] in the HVAF-spraying process than for other spraying techniques, such as HVOF (High Velocity Oxy-Fuel) and APS (Atmospheric Plasma Spraying), for which the powder particles exhibit velocities of 550 m/s [43] and 300 m/s [44], respectively, and temperatures of 3000 °C [43] and 15000 °C (flame temperature) [44], respectively.

As mentioned in the previous section, the disadvantage of high-alloyed steels is their relatively poor mechanical properties and fabricability, which limits the addition of corrosion resistance enhancing elements. The use of corrosion protective coatings eliminates these kinds of limitations and enables the use of higher amounts of such elements. As previously mentioned, the coating density is greatly improved with the HVAF spraying technique. However, in relation to applications in which metallic components are exposed to extremely harsh environments, even very low degrees of coating porosity may be problematic. As mentioned in Chapter 2, the flue gas in biomass- and waste-fired boilers contain large amounts of alkali salts (along with alkali chlorides) and HCl (g). A small degree of open porosity (interconnected network of pores) can be enough to enable the transport of these species to the substrate. Most applications have maintenance stops to repair or exchange components. This is

especially problematic when utilizing coatings. The reason for this is that the thermal expansion coefficients of the substrate and the coating may differ significantly. This can result in mechanical stresses during temperature fluctuations (for example, during maintenance stops) and may lead to spallation of the coating. The HVAF-sprayed coatings in this study were produced by University West. In order to assess the potential of using HVAF-sprayed coatings for corrosion protection in harsh environments, the performance of these was investigated in both a laboratory environment, mimicking the environment in a biomass- and waste-fired boiler, and in a real biomass-fired boiler.

Another type of coating technique is overlay welding. This is a welding process for depositing one or several layers of metal/alloy and chemically bonding these to a substrate in order to improve desirable properties, such as corrosion resistance (weld cladding) or wear resistance (hardfacing). Overlay welding generally results in denser coatings than thermal spraying, which is highly advantageous from a corrosion resistance perspective. In addition, overlay welding is more practical when working with large components since the welding equipment is relatively lightweight and portable compared to the equipment for thermal spraying. A disadvantage with overlay welding that can be crucial depending on the tolerances and dimensions of the component is the higher heat impact than for thermal spraying techniques, which can induce thermal distortions of the component. Additionally, the criterium of weldability can be a limiting factor when it comes to choosing the alloying composition [45, 46]. In this study, the performance of different overlay welded materials produced by Kanthal, was investigated in a simplified laboratory environment, mimicking the environment in a biomass- and waste-fired boiler, for up to 500 hours.

3.3 Corrosion challenges at high temperatures

Most high-temperature applications are associated with different degrees of corrosion challenges. In order to find viable solutions to these challenges, such as altering the design (or fuel) of the application, and selection of materials it is of utmost importance to understand why oxidation/corrosion occurs and what mechanisms are involved. The fundamentals of oxidation/corrosion of metals will be explained in the following chapter.

4 Oxidation of metals

Most metals and alloys are thermodynamically unstable in an oxygen-containing atmosphere and therefore spontaneously react with the environment, thereby forming different oxides. The oxides that form depends on several factors in the environment the metal is exposed to [12]. Temperature is one of the main factors, as the rate of oxidation reactions increase with temperature [40]. However, not only is the rate of the oxidation reactions affected by the temperature, but also the spontaneity of the reactions that determines which oxides form. The stability of an oxide is also dependent on the oxygen partial pressure, p(O_2), in the surrounding atmosphere.

The oxidation resistance of a metal and/or alloy is dependent on the formation of a slow growing and well-adherent oxide scale. Thus, the surrounding environment and alloy chemistry are crucial factors to take into consideration when choosing a material for a specific application.

4.1 Thermodynamics

The chemical reaction between a metal (M) and oxygen gas (O_2) can be written as:

$$xM(s) + \frac{y}{2}O_2(g) \rightleftharpoons M_xO_y(s) \qquad \text{(Reaction 4.1)}$$

The spontaneity of Reaction 4.1 is determined by the second law of thermodynamics, which can be written in terms of the Gibbs free energy (G) of a system if assumptions of constant temperature and pressure apply:

$$G = H - TS \qquad \text{(Equation 4.1)}$$

where H and S are the enthalpy and the entropy of the system, respectively, and T is the temperature. For the above conditions (constant temperature and pressure), the reaction is spontaneous if ΔG has a negative value. The reaction is instead thermodynamically unfavorable if the value of ΔG is positive, and the reaction is at equilibrium if ΔG is equal to zero [47]. On a basis of one mole O_2, Reaction 4.1 can be written as in Reaction 4.2:

$$\left(\frac{2x}{y}\right)M(s) + O_2(g) \rightleftharpoons \left(\frac{2}{y}\right)M_xO_y(s) \qquad \text{(Reaction 4.2)}$$

Using the relation between ΔG and the activities of the species involved, ΔG for Reaction 4.2 can be expressed as:

$$\Delta G = \Delta G^\circ + RT\ln\left(\frac{{a_{M_xO_y}}^{2/y}}{({a_M}^{2x/y})(a_{O_2})}\right) \qquad \text{(Equation 4.2)}$$

where ΔG° is the Gibbs free energy at standard conditions, R is the universal gas constant, and a is the activity of the reactants and products in Reaction 4.2. At all temperatures and pressures, the activities of pure solids are equal to 1, and by definition, $a_{O_2} = p_{O_2}$ (oxygen partial pressure). Considering the dissociation of an oxide into oxygen gas and metal at equilibrium, where $\Delta G = 0$, Equation 4.2, can be simplified as follows:

$$\Delta G^\circ_{O_2} = RT\ln p_{O_2} \qquad \text{(Equation 4.3)}$$

where p_{O_2} can be interpreted as the dissociation pressure of oxygen, i.e. the lowest oxygen partial pressure at which the oxide is thermodynamically stable at a given temperature. A convenient way of displaying this for several types of oxides is by means of an Ellingham diagram, see Figure 3.

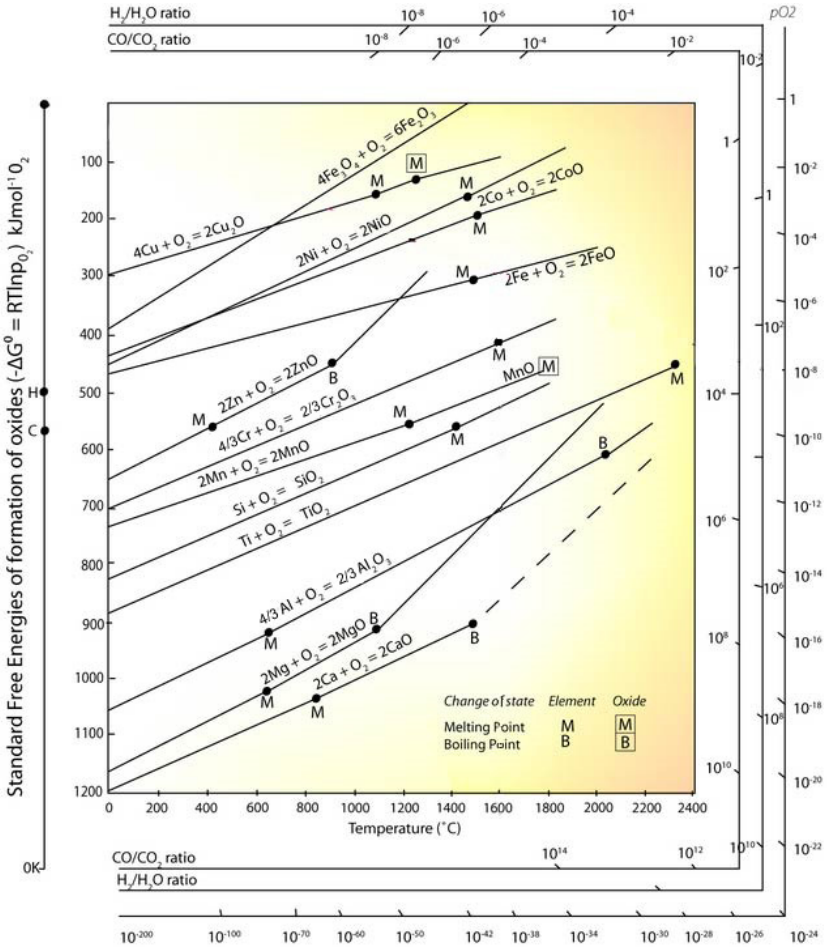

Figure 3: Ellingham diagram displaying the temperature dependence of oxide stability for several metals [48].

4.2 Oxide formation

4.2.1 Initiation of oxide formation

For the initial oxide formation to take place, oxygen in the atmosphere must be adsorbed onto the metal surface and subsequently reduced to O^{2-} ions, see Figure 4. A reaction occurs when the oxygen anions come into contact with the metal cations, and the oxide formation is thus nucleated. The oxide nuclei continue to grow laterally until a continuous oxide layer has formed on the metal surface [12]. The adsorption of oxygen onto the metal surface and the oxide scale formation are affected by factors such as surface preparation, impurities and defects on the metal surface.

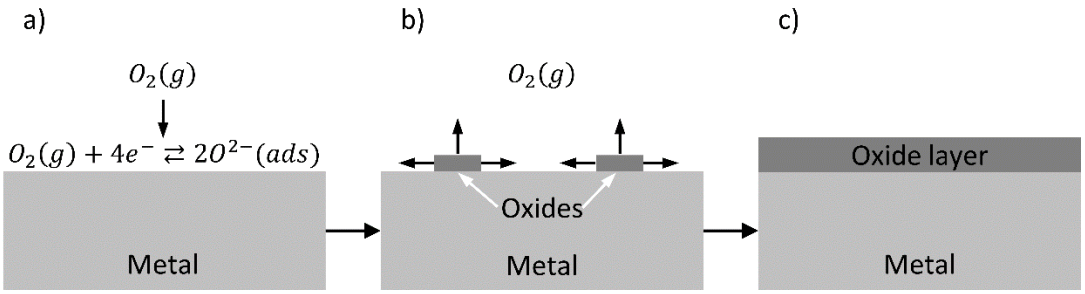

Figure 4: Illustration of initial oxide formation on a metal surface, initiated by the adsorption of oxygen (a), followed by oxide nucleation (b) and finally the formation of a continuous oxide scale (c).

Once a continuous oxide scale has formed, the metal is no longer in direct contact with the atmosphere (assuming the absence of pores or micro cracks in the oxide). At room temperature, this generally means that the oxide formation process has been fully inhibited since the diffusion of ions through the oxide scale is very slow. However, as the temperature increases, the diffusion rate of ions within the oxide scale rapidly increases [12].

4.2.2 Oxide defects

Above absolute zero temperature, all crystalline materials, such as oxides, contain defects in their crystal structure, which are essential for ion and electron transport through the material. The types of defects can be divided into two groups[12, 49]:

1. Point defects
2. Line and surface defects

The first type of defects, point defects, are imperfections in the crystal structure that are limited to one lattice site, such as vacancies or interstitial atoms. Impurities, such as foreign atoms, are also considered point defects. The number of cations and anions in stoichiometric crystals are in balance, resulting in a low defect concentration. However, there are other point defects that do not disturb the stoichiometric balance; these are Schottky and Frenkel defects, see Figure 5 and Figure 6, respectively.

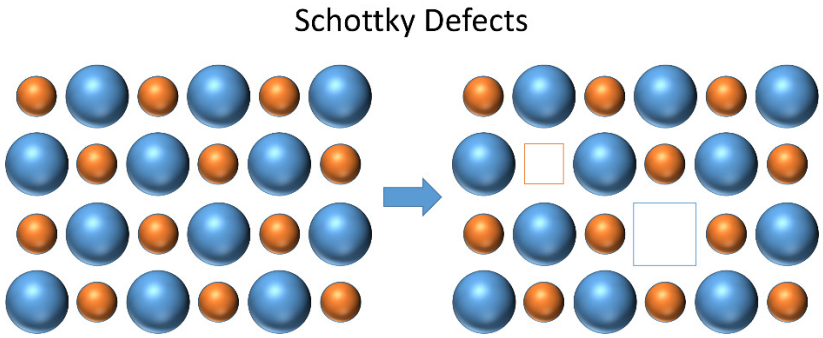

Figure 5: Schematic illustration of Schottky defects.

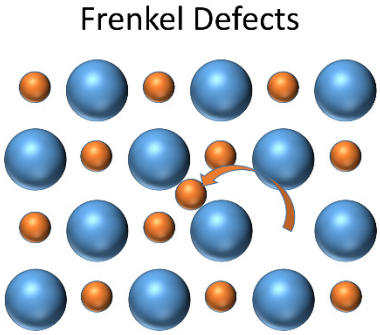

Figure 6: Schematic illustration of Frenkel defects

Schottky defects involve the formation of a cation vacancy that is balanced by an anion vacancy to maintain charge neutrality. Frenkel defects, in contrast, involve the relocation of a cation to an interstitial lattice site, leaving behind a cationic vacancy. Both of these defects increase the ion mobility in the crystalline material but do not provide a mechanism by which electrons can be transported [47].

The defect concentration in non-stoichiometric oxides is higher than in stoichiometric oxides, and the former can be classified as semiconductors, i.e. a material that has an electrical conductivity value somewhere between a conductor and an insulator. These oxides can behave as either p-type or n-

type semiconductors. P-type semiconductors have a deficiency of metal or an excess of oxygen in the crystal structure in the form of metal vacancies or interstitial oxygen. These defects result in a negative charge that is compensated by positive electron holes. N-type semiconductors have either a metal excess or an oxygen deficiency in the form of interstitial metal ions or oxygen vacancies. These results in a positive charge that is compensated by excess electrons [12, 47].

The second group, line and surface defects, comprises several types of defects. One of them is edge dislocation in which a plane of atoms is terminated in the middle of a crystal. Grain boundaries are important interfacial defects in which grains with different crystallographic orientations are separated, see Figure 7.

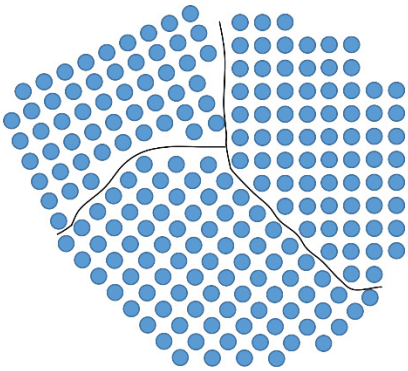

Figure 7: Schematic illustration of grains with different crystallographic orientation resulting in grain boundaries.

The irregularity along a grain boundary results in a higher energy state of the bonded atoms, which causes a higher chemical reactivity than within the grains [49]. For this reason, impurities tend to preferentially segregate along grain boundaries.

4.2.3 Diffusion

As mentioned in the previous section, the transportation of ions through any crystalline material, such as oxides, occurs through defects present in the crystal structure of the material. There are several different diffusion paths and mechanisms that can take place depending on the type(s) of defects that are present. The mechanisms can be divided into two groups [12]:

- Lattice diffusion
- Short-circuit diffusion

These types of diffusion have different diffusion coefficients, depending on the element, the phases present and the temperature [12]. This is described in Equation 4.4:

$$D = D_0 e^{-\frac{Q_D}{RT}} \qquad \text{(Equation 4.4)}$$

where D is the diffusion coefficient, D_0 is the frequency factor (temperature independent) and Q_D is the activation energy for diffusion.

4.2.3.1 Lattice diffusion

Transport of ions through lattice diffusion occurs by means of point defects, described in section 4.2.2. The main mechanisms for lattice diffusion are illustrated in Figure 8 [12].

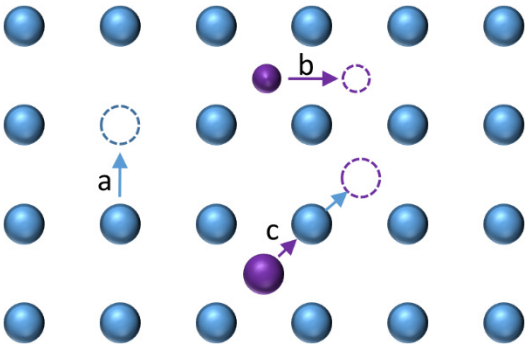

Figure 8: Schematic illustration of the three main mechanisms of lattice diffusion; a) vacancy diffusion, b) interstitial diffusion and c) interstitialcy diffusion.

Vacancy diffusion occurs due to the presence of vacancies in the crystal structure. The mechanism consists of the movement of an atom or ions from a regular lattice site to an adjacent vacancy, resulting in another vacancy.

Interstitial diffusion is most common for smaller atoms or ions that are situated at an interstitial lattice site and involves the movement from one interstitial site to an adjacent vacant interstitial site. The mechanism can occur for larger atoms or ions as well but can result in distortions in the crystal structure.

Interstitialcy diffusion consists of the dislocation of an interstitial atom or ion to an occupied regular lattice site, forcing the atom or ion to move to an adjacent interstitial lattice site.

4.2.3.2 Short-circuit diffusion

Line defects, such as grain boundaries, were described in section 4.2.2. These are especially important when it comes to the diffusion of ions in oxides at lower temperatures (below 600 °C). This is because of the much greater flux of atoms and ions along the grain boundaries than within the grain at lower temperatures. This can be explained by the higher energy state of the atoms bonded along the grain boundaries, which leads to a significantly lower activation energy than with lattice diffusion. Thus, the transport of ions through an oxide scale at lower temperatures is dominated by grain boundary diffusion [49, 50]. As the temperature increases, the importance of lattice diffusion increases, and thus the contribution of lattice diffusion to the total ion diffusion approaches that of grain boundary diffusion. However, this also depends on the defect concentration and the grain size in the crystalline material (smaller grains result in larger grain boundary area). In highly stoichiometric oxides with low defect concentrations, such as α-alumina, grain boundary diffusion is dominant even at higher temperatures.

4.3 Oxidation kinetics

The weight of the metallic material increases throughout the oxidation process due to the uptake of oxygen during oxide formation. Because of this, the oxidation rate of a metal can be measured with continuous or discontinuous (at certain intermediate time points of the oxidation process) weighing. The oxidation rate can generally be described with three different kinetic laws, namely the linear, parabolic and logarithmic rate laws [12], illustrated in Figure 9.

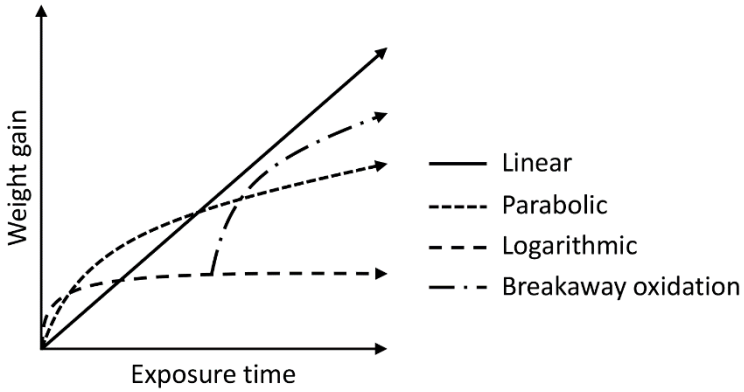

Figure 9: Schematic representation of the three most common kinetic rate laws during oxidation and breakaway oxidation.

Investigating the kinetics of the oxidation process is vital to obtain valuable information about the oxide formation, the properties of the oxide scale(s) and the oxidation mechanisms involved. In reality, the kinetic laws largely depend on factors such as temperature, oxygen partial pressure in the present environment, surface preparation, pre-treatments, the alloy chemistry (determines what oxides may form) and rate-determining mechanisms. In some cases, it is not possible to describe the oxidation rate with only one kinetic equation but a combination of two or more. This also gives valuable information about the oxidation process.

4.3.1 Linear rate law

In some cases, the oxidation process can be described with the linear rate equation (Figure 9), i.e., when the oxidation rate is constant with time. The linear rate equation is expressed as [12]:

$$\frac{dx}{dt} = k_l \qquad \text{(Equation 4.5)}$$

$$x = k_l t + C \qquad \text{(Equation 4.6)}$$

where x is the oxide thickness, t is the amount of time from the beginning of the oxidation process, k_l is the linear rate constant and C is the integration constant. Since the oxide thickness, x, is assumed to be equal to zero at the beginning of the oxidation process (t=0), C is equal to zero. If the oxidation rate can be described by the linear rate equation, the rate determining step can be a surface or phase boundary process or a reaction [12]. This can involve a steady-state reaction that is limited by the adsorption of oxygen at the oxide/gas interphase when diffusion through the oxide scale is rapid. This mostly occurs when the oxide scale is thin (i.e. at the beginning of the oxidation process) and the oxygen partial pressure is low or when the formed oxide scale is highly porous, leaving the metal surface exposed.

4.3.2 Parabolic rate law

Many metals have been found to follow a parabolic time dependence (see Figure 9) when oxidized at elevated temperatures. The parabolic rate equation is given by:

$$\frac{dx}{dt} = \frac{k_p'}{x} \qquad \text{(Equation 4.7)}$$

$$x^2 = 2k_p' t + C = k_p t + C \qquad \text{(Equation 4.8)}$$

where k_p' and k_p are the parabolic rate constants, and C is the integration factor (mostly equal to zero, see section 4.3.1). Parabolic oxidation behavior was first recognized by Carl Wagner in the 1930s [51]. A parabolic oxidation rate at high temperatures is indicative of a diffusion-controlled process. This can include the diffusion of oxygen ions, metal ions or both through the growing oxide scale. As the oxide

scale thickens, the diffusion distance of the reactants increases, resulting in a continuously decreasing oxidation rate with time. Wagner made some additional assumptions:

- The oxide layer is compact and adherent.
- Thermodynamic equilibrium is established throughout the oxide as well as at the gas/oxide and oxide/metal interface.
- Oxygen solubility in the metal can be neglected.

Some alloys can form oxide scales that instead grow at a sub-parabolic rate, which means that the oxidation rate slows down faster than at a parabolic oxidation rate. This can indicate that other mechanisms, in addition to the increasing distance that ions need to diffuse, limit the oxidation rate. The order of parabolicity (the value of α in x^{α}) can be attained by plotting the logarithmic value of the mass change against the logarithmic value of time. If the oxide scale grows with the same parabolicity throughout the entire oxidation process, this will result in a straight line with a constant incline. The value of α can be extracted from the incline:

$$incline = \frac{1}{\alpha} \quad \text{(Equation 4.9)}$$

α will have a value of 2 for oxide scales that grow parabolically, while higher values indicate sub-parabolic growth. An oxide scale grows linearly if α has a value of 1.

4.3.3 Logarithmic rate law

The oxidation process of many metals at lower temperature (generally below 300-400 °C) displays a logarithmic behavior, distinguished by the relatively rapid initial oxidation rate followed by a deceleration to negligible oxidation rates. This kind of corrosion behavior is often described by the logarithmic rate equations [12]:

Direct logarithmic (Figure 9): $x = k_{log} \log(t + t_0) + A$ (Equation 4.10)

Inverse logarithmic: $\frac{1}{x} = B - k_{il} \log(t)$ (Equation 4.11)

where x represents the oxide thickness, t denotes the time k_{log} and k_{il} represents the rate constant for the direct logarithmic and inverse logarithmic rates respectively and A and B are constants. The mechanisms responsible for the logarithmic behavior are not completely clear, but there are several hypotheses, including rate determining chemisorption, the rate determining transport of ions or electrons due to electric fields in or across an oxide scale, and cavity formation in the oxide [12].

4.3.4 Breakaway oxidation

Metals or alloys that are able to form highly protective and slow-growing oxide scales are generally desired in most applications to reduce material degradation and thus, maintenance costs. As long as these types of oxide scales remain intact, the oxidation rate will be very low. However, under certain conditions, these oxide scales can degrade due to reactions with specific species in the surrounding environment, causing them to break down and lose their protective properties, followed by a sudden increase in corrosion rate. This degradation can also be caused by physical defects, such as cracks, or thermal stresses, causing delamination of the oxide layer. In some cases, the broken-down oxide scale regrows and eventually regains its protectiveness. However, the loss of the protective oxide scale can instead lead to the formation of more fast-growing oxide scales, which results in a drastic acceleration of the corrosion process, see Figure 9. The sudden transition from one kinetic behavior to another is commonly known as breakaway oxidation. In most applications, breakaway oxidation signifies the failure of the component and the need to replace it. The majority of studies on high temperature corrosion have focused on improving the protectiveness of slow-growing oxide scales and prevent

their breakdown. However, preventing the breakdown of the protective oxide scale is generally not possible in applications with a harsh environment. A novel approach to increasing the protectiveness of faster growing oxide scales will be explained and discussed in chapter 5.

4.4 Corrosion products

Metals and alloys can form various types of corrosion products. The type(s) formed are largely dependent on temperature (see Ellingham diagram in section 4.1), the environment (oxygen partial pressure, present species) and the chemical composition of the alloy. As described in the previous sections, metals are generally thermodynamically unstable in an oxygen-containing environment in which each metal oxide is thermodynamically stable. These, along with other types of corrosion products, will be described in the following sections.

4.4.1 Oxides

Metals and alloys form oxide scales at both low and high temperatures. These oxide scales can be seen as natural protection against further corrosion. The diffusion of ions through the oxide scale at low temperatures is, and therefore, the growth rate of the oxide scales is relatively low. However, the diffusion through the oxide scale at high temperature occurs at a much higher rate, and the properties of the formed scales are increasingly important to achieve a good corrosion behavior. An oxide scale should meet the following requirements to achieve protective behavior at higher temperatures [52]:

- Thermodynamic stability
- Highly stoichiometry – low defect concentration resulting in slow ion diffusivity
- Thermal expansion coefficient similar to the metal
- High melting temperature
- Well adherent to the alloy
- High plasticity at high temperature

As previously mentioned, the types of oxide scales that can form on an alloy surface mainly depend on the chemical composition of the alloy, the surrounding temperature and gas composition. The properties of each oxide type vary largely and determine the corrosion resistance of a material.

It is generally known that iron-based chromia-forming alloys (FeCr, FeCrNi) are able to form a slow-growing Cr-rich oxide (chromia), while iron-based alumina forming alloys (FeAl, FeCrAl) have the ability to form a slow-growing Al and/or Cr-rich oxide (alumina/chromia). Both of these contribute to good corrosion resistance. Breakdown of the protective oxide generally results in the rapid formation of an iron-rich oxide scale, consisting of outward-growing iron oxide and an inward-growing spinel [53, 54]. This phenomenon is often referred to as breakaway oxidation (described in section 4.3.4). The oxide scale prior to breakaway oxidation is usually called a protective oxide scale, while the thick iron-rich oxide after breakaway oxidation is called a non-protective oxide scale. The structure and properties of the most commonly occurring oxides of iron-based and nickel-based chromia/alumina-formers will be described in the following sections.

4.4.1.1 Iron (Fe) oxides

Iron can form three different types of oxides: wüstite ($Fe_{1-y}O$), magnetite (Fe_3O_4) and hematite (Fe_2O_3). Each of these oxides has a different crystal structure, which largely affects their properties. Wüstite has a rock salt structure (NaCl), magnetite has a spinel structure and hematite has a corundum structure.

Wüstite

Wüstite is only stable at temperatures above 570 °C and at very low oxygen activities. Wüstite is a non-stoichiometric oxide and is metal deficient, as is indicated by the formula ($Fe_{1-y}O$). Thus, Wüstite is a p-type semiconductor. Its crystal structure consists of cubic close-packed oxygen ions with iron ions occupying the octahedral interstices. Because of the low degree of stoichiometry, the ion diffusion through wüstite is fast, and thus the growth of this oxide scale is rapid, resulting in a thick oxide scale at high temperatures [12]. The wüstite formation is inhibited by the presence of Cr in the alloy by shifting the thermodynamical stability to higher temperatures [55].

Magnetite

The crystal structure of magnetite is spinel. A spinel oxide consists of cubic close-packed oxygen ions with metal ions occupying the tetrahedral and octahedral sites. The valency of a metal ion determines the site occupancy. Divalent metal ions occupy tetrahedral sites, while trivalent metal ions occupy the octahedral sites. Since iron can be both in the divalent (Fe^{2+}) and trivalent (Fe^{3+}) state, it can occupy both the tetrahedral and octahedral sites. In alloys containing several divalent and trivalent elements (of similar size), a spinel-type solid solution can form when oxidized. The divalent metal ions in such an oxide, compete for the tetrahedral sites, while the trivalent metal ions compete for the octahedral sites, resulting in a large range of combinations in element distribution. Examples of such spinel oxides are $(Fe,Cr,Ni)_3O_4$, $(Fe,Cr,Al)_3O_4$, $(Cr,Mn)_3O_4$.

Magnetite has a higher degree of stoichiometry than wüstite, resulting in slower ion diffusion through the oxide scale and a lower oxide scale growth rate. However, at higher oxygen partial pressures, magnetite is metal deficient (metal deficiency increases with temperature) and has oxygen excess at lower oxygen partial pressures [12]. Thus, magnetite behaves as a p-type semiconductor.

Hematite

The crystal structure of hematite is corundum. The corundum structure consists of hexagonally close-packed oxygen ions with metal ions occupying 2/3 of the octahedral sites [12]. Other examples of oxides that have a corundum structure are chromia (Cr_2O_3) and alumina (Al_2O_3).

Hematite has the highest degree of stoichiometry of all the iron oxides which results in the slowest ion diffusion of the different iron oxides [40] and therefore a low oxide scale growth rate. Thus, hematite is considered the most protective of the iron oxides. Being oxygen deficient, hematite behaves as an n-type semiconductor in the range of 650-800 °C [12]. However, at higher temperatures, hematite behaves as a p-type semiconductor.

4.4.1.2 Chromium (Cr) oxide

The only solid form of chromium oxide that is stable at high temperatures is chromia, Cr_2O_3. Like hematite, chromia has a corundum structure with oxygen ions hexagonally close-packed and Cr ions occupying 2/3 of the octahedral sites. Because of its high degree of stoichiometry, a chromia scale grows very slowly even at elevated temperatures (up to 1000 °C) [12]. Thus, it is considered a protective oxide and is desired in high-temperature applications to prevent further corrosion.

Measurements of bulk chromia have indicated that the defect structure is metal deficient, meaning that chromia will behave as a p-type semiconductor. However, it has been shown to behave as an n-type semiconductor at low oxygen partial pressures [56]. This suggests that chromia behaves as a p-type semiconductor closer to the oxide surface where the oxygen partial pressure is high, but behaves as an n-type semiconductor close to the oxide/metal interface at which the oxygen partial pressure is low. [12]

Relying on the formation of a chromia scale has several disadvantages even though the chromia scale grows very slowly at temperatures up to 1000 °C. The reason for this is the tendency of chromia to react with certain species at elevated temperatures. The chromia scale can be subjected to the phenomenon known as Cr evaporation in humid environments, in which the Chromia scale is depleted in Cr [8]. If the depletion of Cr is faster than the bulk diffusion of Cr to the chromia scale, this can eventually result in the loss of the protective properties of the chromia scale. Cr evaporation can occur in the absence of water vapor at elevated temperatures (above 900 °C) due to the volatilization of CrO_3 [57, 58]. High-temperature applications, in which alkali-containing compounds are present, tend to be severely detrimental to the protective behavior of chromia. The alkali ions tend to react with the Cr in the chromia scale, resulting in the formation of alkali chromates and generally leading to the loss of the chromia scale [9]. Both of these phenomena will be further described in sections 4.5.1 and 4.5.2.

4.4.1.3 Aluminum (Al) oxide

The only stable form of aluminum oxide is alumina, Al_2O_3, which can exist in several variations. The most commonly occurring forms are the α- and γ-phases. γ-Al_2O_3 is usually observed after exposure to temperatures below 900 °C and is a transient oxide (not thermodynamically stable). At 900-1000 °C, it transforms into α-Al_2O_3, which is the only thermodynamically stable form of alumina. α-Al_2O_3 forms at a very low rate while remaining stable at temperatures below 900 °C, which is why it is generally not found in lower temperature ranges. α-Al_2O_3 has a very high degree of stoichiometry due to its large bandgap and high lattice energy, which result in a very low defect concentration [12]. Thus, ion diffusion through the oxide scale is very slow even at elevated temperatures and results in a very low growth rate. For this reason, a α-Al_2O_3 scale has outstandingly high corrosion resistance that prevents the metal/alloy from further corrosion.

Similar to hematite and chromia, α-Al_2O_3 has a corundum structure with hexagonally close-packed oxygen ions with 2/3 of the octahedral sites occupied by Al ions. Because it has the same crystal structure as both chromia and hematite (α-Fe_2O_3), the initial formation of these favors the nucleation of α-Al_2O_3 [39], which is one of the reasons why the combinations of Fe, Cr and Al in FeCrAl alloys are beneficial. α-Al_2O_3 is a highly inert oxide that is beneficial to corrosion resistance in complex environments containing various corrosive compounds. As previously mentioned, Cr_2O_3 is sensitive to water vapor and alkali-containing compounds because of the Cr-depleting reactions involved in the presence of these. However, these reactions do not occur for α-Al_2O_3, which generally remains protective in such environments as long as the oxide scale remains intact. However, the high temperature needed for rapid formation of an α-Al_2O_3 scale is a major drawback for applications involving temperatures below 900 °C in which corrosion protection must rely on the formation of other less corrosion resistant oxide scales.

4.4.1.4 Silicon (Si) dioxide

Minor traces of Si are generally found in iron-based alloys because of the presence of Si (in the form of silica (SiO_2)) in iron ore. For this reason, more energy has to be put into the process to remove the remaining Si. However, this is often unnecessary. Sometimes, small amounts of Si are added to steels for its positive effects on the corrosion resistance. Si-containing alloys has been shown to form SiO_2 (often amorphous) in the form of a dense discontinuous or continuous layer when exposed to high temperatures [19, 22, 59-61]. This layer may act as a diffusion barrier, inhibiting the diffusion of ions which in turn prevents further corrosion attack.

4.4.2 Chromates and metal chlorides

As mentioned in chapter 2, the combustion of biomass and waste results in a flue gas with high concentrations of alkali- and chloride-containing compounds. These are involved in corrosion reactions

that are detrimental for the material lifetime of several important components of the boiler. The mechanisms for these reactions will be further described in sections 4.5.2 and 4.5.3.

The presence of alkali-containing compounds, such as KCl, K_2CO_3, NaCl, is especially unfavorable to the performance of chromia-forming alloys because of the reaction between chromia and alkali species, resulting in the formation of alkali chromates. These forms as porous crusts on the alloy surface (see Figure 10) and do not contribute to the corrosion resistance of the alloy but instead deplete the chromia scale of Cr, eventually resulting in the loss of its protective properties.

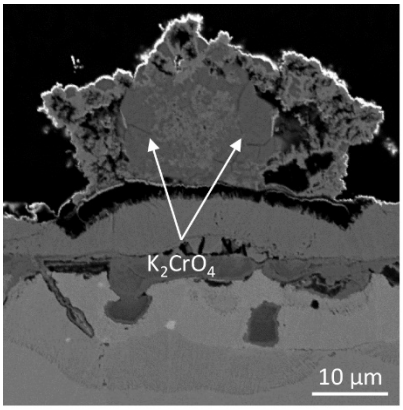

Figure 10: SEM-BSE cross-section image of a crust of K_2CrO_4 formed after 168 hours of exposure to 5% O_2 + 20% H_2O + N_2 with KCl present.

The presence of chloride-containing species at high temperatures, often leads to a severe corrosion attack on surrounding metals and alloys. One of the corrosion products associated with this is metal chlorides, such as $FeCl_2$, $FeCl_3$, $CrCl_2$, $CrCl_3$ and $NiCl_2$. Which of these that are able to form depends on the alloy chemistry, chlorine/chloride activity and oxygen activity. Metal chlorides are formed at low oxygen partial pressures [62] and are therefore usually detected close to the oxide/metal interface, see Figure 11.

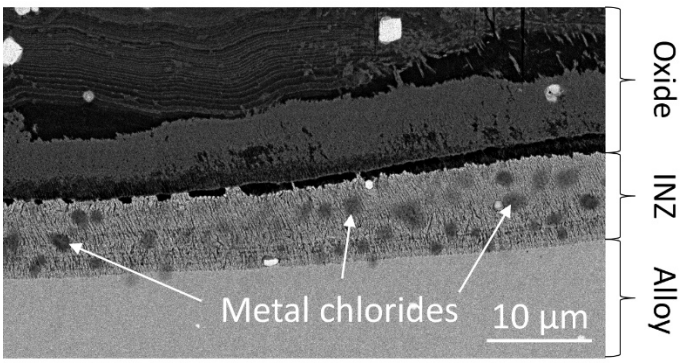

Figure 11: SEM-BSE cross-section image displaying metal chloride formation in the internal nitridation zone on Fe5Cr3Al after exposure at 600 °C in the presence of KCl.

Due to their volatility in combination with their instability at higher oxygen activities, metal chlorides often diffuse up through the oxide scale, causing them to decompose when a higher oxygen partial pressure has been reached. Because of this, metal chlorides are often difficult to detect and analyze.

4.5 Corrosion mechanisms

Various kinds of reactions can occur depending on the environmental parameters that a metal/alloy is exposed to. Apart from oxide formation, these reactions generally reduce the material lifetime of metallic components by increasing the corrosion rate and breaking down protective oxide scales. Some of the most important corrosion mechanisms associated with the environment in biomass- and waste-fired boilers will be described in the following sections.

4.5.1 Cr evaporation

As mentioned in chapter 2, the flue gas in a biomass- and waste-fired boiler contains higher amounts of water vapor than the flue gas in coal-fired boilers. It is well known that the presence of water vapor drastically accelerates the oxidation rate of chromia forming steels [12]. Various hypotheses have been put forth about the mechanism involved in the corrosive effect of water vapor. However, the one that has become the most accepted in oxygen-containing environments is the hypothesis of the volatilization of Cr from the chromia scale [8, 63, 64]. In this mechanism, the protective chromia scale reacts with oxygen and water vapor to form chromic acid according to Reaction 4.3:

$$\frac{1}{2}Cr_2O_3(s) + \frac{3}{4}O_2(g) + H_2O(g) \rightleftharpoons CrO_2(OH)_2(g) \qquad \text{(Reaction 4.3)}$$

$\Delta G = 81.1 \frac{kJ}{mol}$, p($CrO_2(OH)_2$)=$2.97 * 10^{-7} atm$ (calculated with the following parameters and K_{eq} from Factsage; T=600°C, pO_2=0.05, pH_2O=0.2)

Despite the positive value of ΔG, this reaction has been shown to occur at significant rates at temperatures as low as 600 °C in systems with flowing gases. This is because the equilibrium shifts to the right when the chromic acid is transported away from the metal surface. As long as the diffusion of Cr from the alloy to the surface (replenishing the Cr in the chromia scale) is higher than the evaporation of Cr, the chromia will remain protective. However, if Cr evaporation occurs at a higher rate than the alloy is able to resupply the surface with Cr, the reaction will eventually result in the breakdown of the protective chromia scale. This would be followed by a rapid increase in oxidation rate because of formation of faster growing oxide scales (iron oxide for iron-based alloys). The transition between protective behavior and rapid oxidation rate is commonly termed “breakaway oxidation”.

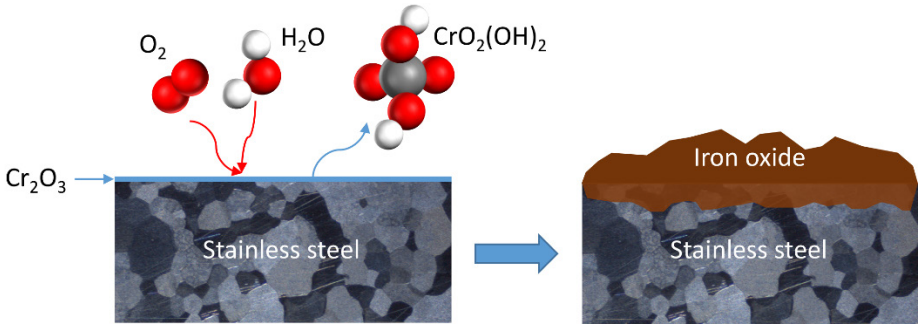

Figure 12: Schematic illustration of the breakdown of the protective chromia scale on iron-based stainless steel due to Cr evaporation.

4.5.2 Chromate formation

As mentioned in chapter 4.4.2, chromates are often found in high-temperature environments containing alkali species. The formation of alkali chromates often leads to the breakdown of the protective Cr-rich scale on chromia-forming steels. The mechanism behind this has been proposed by Petterson et al [65, 66], who suggest that the alkali-containing species, such as KCl and K_2CO_3, reacts with the chromia layer to form K_2CrO_4 according to the following reactions:

$$\frac{1}{2}Cr_2O_3(s) + 2KCl(s) + H_2O(g) + \frac{3}{4}O_2(g) \rightleftharpoons K_2CrO_4(s) + 2HCl(g) \quad \text{(Reaction 4.4)}$$

$\Delta G = 145.6\frac{kJ}{mol}$,p(Cl_2)=$1.04 * 10^{-6} atm$ (calculated with the following parameters and K_{eq} from Factsage; T=600°C, pO_2=0.05, pH_2O=0.2)

$$\frac{1}{2}Cr_2O_3(s) + K_2CO_3(s) + \frac{3}{4}O_2(g) \rightleftharpoons K_2CrO_4(s) + CO_2(g) \quad \text{(Reaction 4.5)}$$

$\Delta G = 72.5\frac{kJ}{mol}$, p(HCl)=$9.87 * 10^{-4} atm$ (calculated with the following parameters and K_{eq} from Factsage; T=600°C, pO_2=0.05, pH_2O=0.2)

Similar to Reaction 4.3, the values of ΔG of reaction 4.4 and 4.5 are positive, implying that the reaction is not thermodynamically spontaneous. However, the equilibrium vapor pressure of HCl is significant, which means that in a system with flowing gas, such as areas exposed to the flue gas in biomass- and waste-fired boilers, the gaseous species (in this case HCl) are transported away from the metal which shifts the equilibria towards the right side of the reaction.

The formation of K_2CrO_4 results in the depletion of Cr in the chromia scale, which will eventually break down, leaving the metal/alloy unprotected. This generally results in the formation of faster growing oxide scales and, consequently, increased material degradation, see Figure 13.

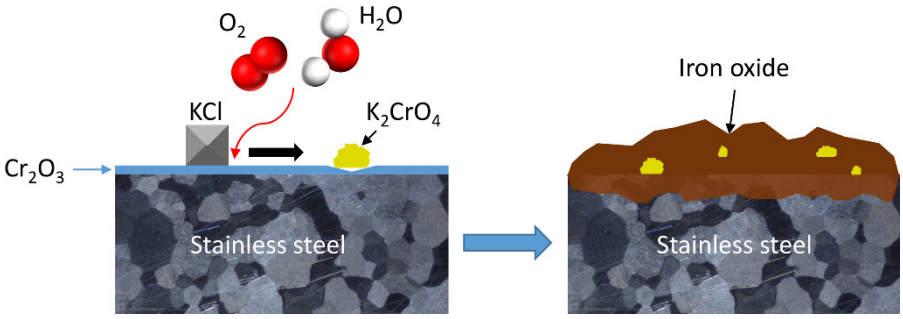

Figure 13: Schematic illustration of the breakdown of the chromia scale on iron-based stainless steels due to formation of K_2CrO_4 in the presence of KCl.

4.5.3 Chlorine-induced corrosion

In addition to high levels of water vapor and alkali-containing compounds, large amounts of chlorine-containing species, such as KCl, NaCl and HCl, are present in biomass- and waste-fired boilers. It is generally known that these species negatively affect the high temperature corrosion resistance of metals, resulting in drastically accelerated corrosion rates. The mechanism involved has been investigated extensively over the years but is still not fully understood. However, a hypothesis called "active oxidation" (or chlorine cycle) has been suggested by McNallan et al [67] and further developed by Grabke et al [68]. According to their hypothesis, the mechanism is initiated by the transport of molecular chlorine, Cl_2, through micro cracks and pores in the oxide scale to the oxide/metal interface. There, Cl_2 reacts with the metal according to Reaction 4.6:

$$\frac{x}{2}Cl_2(g) + Me(s) \rightleftharpoons MeCl_x(s) \quad \text{(Reaction 4.6)}$$

where x is the valency of the metal ion. Metal chlorides, such as $FeCl_2$ and $CrCl_2$, are only stable at low oxygen partial pressures, which is why they generally form at the oxide/metal interface. However, at elevated temperatures, the vapor pressure of metal chlorides is high, and they are therefore believed to diffuse upward through the oxide scale. Along the oxide scale there is a gradient of oxygen partial pressure with the maximum value at the scale surface, and a minimum value at the oxide/metal

interface. As the metal chlorides diffuse up through the oxide, they eventually reach an oxygen partial pressure at which they are not stable. Thus, the metal chlorides will with oxygen to form their respective metal oxides according to Reaction 4.7:

$$yMeCl_x(g) + \frac{z}{2}O_2(g) \rightleftharpoons Me_yO_z(s) + \frac{xy}{2}Cl_2(g) \quad \text{(Reaction 4.7)}$$

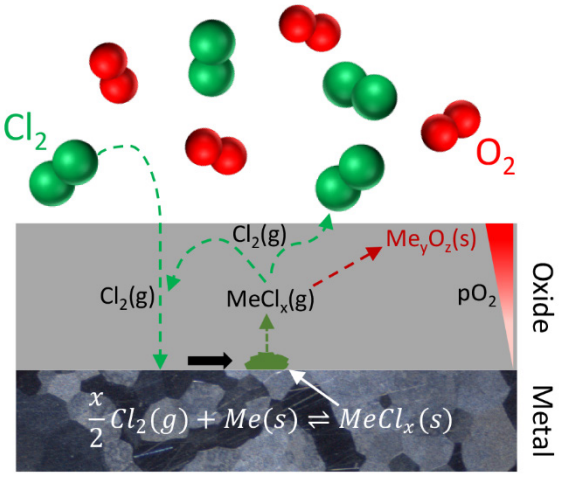

Figure 14: Schematic illustration of the active oxidation mechanism.

The Cl_2 formed in Reaction 4.7 can either be released to the surrounding atmosphere or diffuse back to the oxide/metal interface to begin a new cycle (from reaction 4.6) [68]. However, there are some problems with the active oxidation mechanism. The hypothesis is based on the ability of Cl_2 to diffuse through the oxide scale and a low oxygen partial pressure at the oxide/metal interface. If the cracks and pores in the oxide scale are large enough for Cl_2 to diffuse through, then O_2 molecules should be able to diffuse through the same cracks and pores since the molecular length of Cl_2 (396 pm) is larger than that of O_2 (264 pm). Thus, the oxygen partial pressure at the oxide/metal interface would become too high to favor the formation of metal chlorides.

Another approach has been suggested by Folkesson et al [69]. In contrast to the hypothesis on the transport of molecular chlorine through the oxide scale, this approach involves the flux of anions and cations and an electronic current. It is suggested that, since Cl_2 is a strong oxidant and easily dissociates, it is reduced at the oxide scale surface which results in the formation of Cl^- ions, see Reaction 4.8. The electronic current needed for the reaction is provided by the oxidation of metal at the oxide/metal interface (Reaction 4.9).

$$Cl_2(g) + 2e^- \rightleftharpoons 2Cl^-(ads) \quad \text{(Reaction 4.8)}$$

$$Me(s) \rightleftharpoons Me^{n+} + ne^- \quad \text{(Reaction 4.9)}$$

Chloride ions can also be formed by the reduction of adsorbed oxygen and the simultaneous deprotonation of adsorbed HCl according to Reaction 4.10:

$$2HCl(ads) + \frac{1}{2}O_2(ads) + 2e^- \rightleftharpoons H_2O(g) + 2Cl^-(ads) \quad \text{(Reaction 4.10)}$$

In the presence of oxygen and water vapor, alkali chlorides, such as KCl, can form chloride ions through a reaction with water vapor and oxygen according to the following reaction [70]:

$$2KCl(s) + \frac{1}{2}O_2(g) + H_2O(g) + 2e^- \rightleftharpoons KOH(g) + 2Cl^-(ads) \quad \text{(Reaction 4.11)}$$

Grain boundaries can be regarded as inner surfaces in a polycrystalline material [71] due to the higher energy state of the atoms bonded along grain boundaries as mentioned in section 4.2.3.2. Thus, the activation energy for diffusion is low along grain boundaries. When the chloride ions have formed and adsorbed on the oxide scale surface, they are expected to have high mobility compared to the oxygen ions due to their smaller charge/radius ratio. Therefore, the diffusivity of chloride ions along the grain boundaries can be higher than for the oxygen ions. The transport of chloride ions from the oxide surface to the oxide/metal interface via grain boundary diffusion agrees well with the formation of metal chlorides at the oxide/metal interface, as this would remain an area with a low oxygen partial pressure.

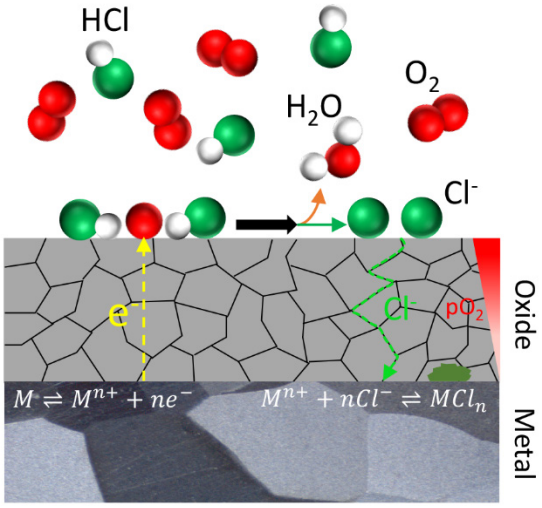

Figure 15: Schematic illustration of the chlorine-induced corrosion mechanism according to the electrochemical approach.

5 Beyond breakaway oxidation – a new approach

Breakaway oxidation is a widely used term in the field of high temperature corrosion. The term denotes the transition from a slow-growing oxide scale (commonly termed protective oxide scale) to a faster growing oxide scale. In many high temperature applications, this transition signifies the end of the lifetime of the metallic component. Therefore, research focusing on improving the properties of the protective oxide, and thereby preventing breakaway oxidation from occurring, is being conducted to a large extent. However, preventing breakaway oxidation might not be possible in certain applications. This is usually the case in harsh environments containing certain corrosive species that tend to break down protective oxide scales [8, 9, 53, 65, 66]. As previously mentioned, biomass- and/or waste-fired boilers generally has highly corrosive environments due to the presence of alkali chlorides, HCl(g) and elevated levels of water vapor. Therefore, metallic components generally exhibit breakaway oxidation at a very early stage after being put into operation [35, 72-76]. Improving the corrosion resistance of the protective oxide scales will not significantly influence the component lifetime for these types of applications. Because of this, recent studies have shifted towards investigating the behavior of the oxide scales formed after breakaway oxidation and the possibility of improving their corrosion resistance [77-79].

It has been shown that it is possible to significantly influence the growth rate of the iron-rich oxide, formed after breakaway oxidation, by altering the alloy composition. This means that it is possible to reduce the material degradation of metallic components to a large extent even in harsh environments in which breakaway oxidation occurs at an early stage. Because of these findings, describing the oxidation process as the formation of a protective oxide (alumina/chromia) followed by breakaway oxidation and the formation of non-protective oxides seems inaccurate and therefore needs to be elaborated. Thus, these two stages of the oxidation process (protective and non-protective oxide) have been defined as the primary protection and the secondary protection of an alloy (alternatively the primary and secondary corrosion regimes) [78]. The influence of the different alloying elements on both the primary and secondary protection, but mainly the latter, will be further discussed in chapter 8.

5.1 Lifetime prediction models

In addition to simplifying the distinction between different corrosion regimes and elucidating that breakaway oxidation does not necessarily equates the end of the lifetime of a metallic component, this new approach can be highly advantageous in the process of developing a lifetime prediction model.

There are many complications associated with developing a reasonably accurate lifetime prediction model, and the difficulty increases with the complexity of the system. DICTRA is a diffusion-based modelling tool that can be used to predict simple oxidation processes [80-82]. The first criterium for modelling an oxidation process is that the growth rate of the oxide is diffusion controlled, which is true for many dense and adherent oxides. The accurate prediction of the oxidation process within the primary regime (chromia/alumina) has already been achieved [83]. However, a range of complications arise in more complex and corrosive environments. Consider the oxidation of a FeCr alloy in an oxygen-containing environment in the presence of alkali salts at high temperature. According to thermodynamic calculations, chromia would form, and the predicted kinetics of the oxidation process would be based on the growth properties of the chromia scale. However, in such a corrosive environment, an FeCr alloy would be in the secondary corrosion regime the majority of the oxidation process, and the prediction would therefore be highly inaccurate. Knowing that the transition from the primary to the secondary regime takes place at an early stage, the oxidation kinetics of an iron oxide scale can be simulated instead to get a more accurate estimation of the material degradation. This

transition can, in addition, occur at a later stage (commonly known as incubation time) in which case the model can be divided into growth kinetics based on chromia (primary protection) for X number of hours followed by growth kinetics based on iron oxide (secondary protection) for Y number of hours. However, as mentioned in the previous section, altering the chemical composition of an alloy can significantly influence the oxidation kinetics of the iron-rich oxide scale. Thus, simulating the growth of pure iron oxide will in some cases also result in highly inaccurate predictions. In order to develop and improve the lifetime prediction models, it is of utmost importance to increase the understanding of the influence of different alloying elements on the oxidation kinetics within the secondary corrosion regime as well as the underlying mechanisms.

Additional challenges, in relation to lifetime prediction models, are phenomena, such as spallation and/or crack formation, which often occur in highly corrosive environments and in applications in which the metallic components are subjected to thermal cycling. Spallation of the oxide scale and crack formation in the oxide scale result in exposure of the metal substrate to the surrounding environment and a new oxide scale will begin to form and, consequently, the oxidation rate will rapidly increase [84]. Thus, these phenomena also must be taken into consideration and incorporated in future models to accurately predict the lifetime of metallic components in highly corrosive environments.

6 Experimental Procedure

This chapter describes the experimental procedures used in this study, including investigated materials, sample preparation, exposure conditions and utilized analytical equipment.

6.1 Laboratory investigations

Several types of laboratory investigations were conducted to examine the influence of different alloying elements, the mechanisms behind these effects and the potential to utilize different kinds of coatings for corrosion protection. The experimental conditions and procedures differed slightly for the different types of materials and will be described separately in the upcoming sections.

6.1.1 Exposure systems

High-temperature corrosion tests were carried out in two different systems: a horizontal tube furnace and a thermobalance (TGA). These systems have different advantages and disadvantages. Several samples can be exposed simultaneously in the horizontal tube furnace, resulting in a large sample size for accurate analysis. However, no information about the kinetics of the corrosion process can be attained since only the final weight gain can be recorded from these types of exposures. To achieve this, several exposures with different time intervals must be performed. Only one sample can be exposed at a time when utilizing a thermobalance, and several exposures must be performed to ensure reproducibility. However, the advantage of utilizing a thermobalance is that the weight change of the sample is continuously measured during the exposure. Therefore, the kinetics of the corrosion process can be recorded for each sample. In the following sections, the general procedure for the two different systems will be described.

6.1.1.1 Tube furnace exposure

The horizontal tube furnaces used in this study were equipped with silica tubes with an inner diameter of 45 mm. The silica tube was connected to several gas pipes through which various types of gases could be added. The flow rate of these gases was controlled and calibrated using a Bios Definer 220M to achieve the desired flow rate. When the presence of water vapor is desired during exposure, the gas pipes can be connected to a thermostat-controlled water bath, coupled with a membrane, to mix the incoming gas with water vapor. The desired humidity was controlled by changing the temperature of the water bath. When humidity was desired, the temperature of the water bath was set to 60.4 °C, resulting in a water vapor content of 20 vol%. A schematic illustration of the tube furnace set-up is shown in Figure 16.

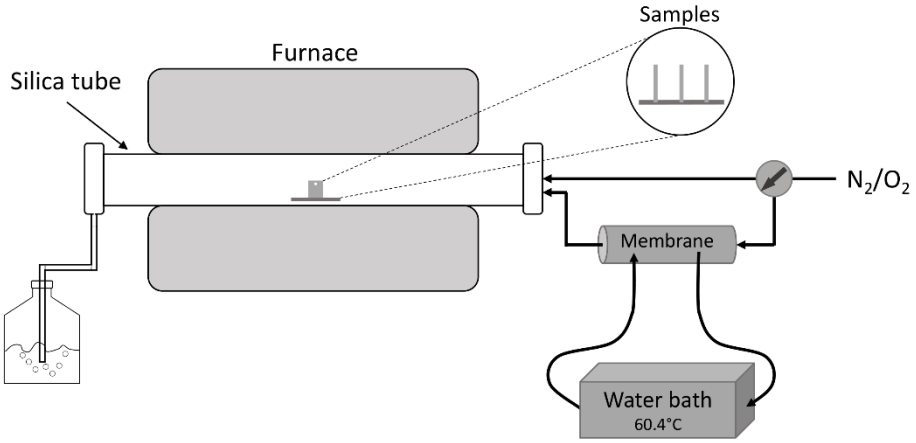

Figure 16: Schematic illustration of the tube furnace set-up used in this study.

Before inserting the samples, the gas flow parameters were adjusted, and the furnace temperature was calibrated so that the center of the silica tube exhibited the desired temperature. The samples were mounted vertically on an alumina sample holder, which can differ depending on the geometry of the samples. The sample holder with the samples was then inserted to the center of the silica tube before closing the system (with a silica end cap). For exposures with water vapor present, the valve had to be turned so that the gas passed through the membrane. After the exposure was finished, and the samples had been taken out of the furnace, they were placed in a desiccator to prevent humidity from reacting with the corrosion products during cooling. The weighing procedure will be described in sections 6.1.2, 6.1.3.1 and 6.1.3.2.

6.1.1.2 Thermobalance exposures (TGA)

The thermobalance used in this study was a Setaram Setsys system connected to a Setaram Wetsys humidifier. A schematic illustration of the TGA system is shown in Figure 17.

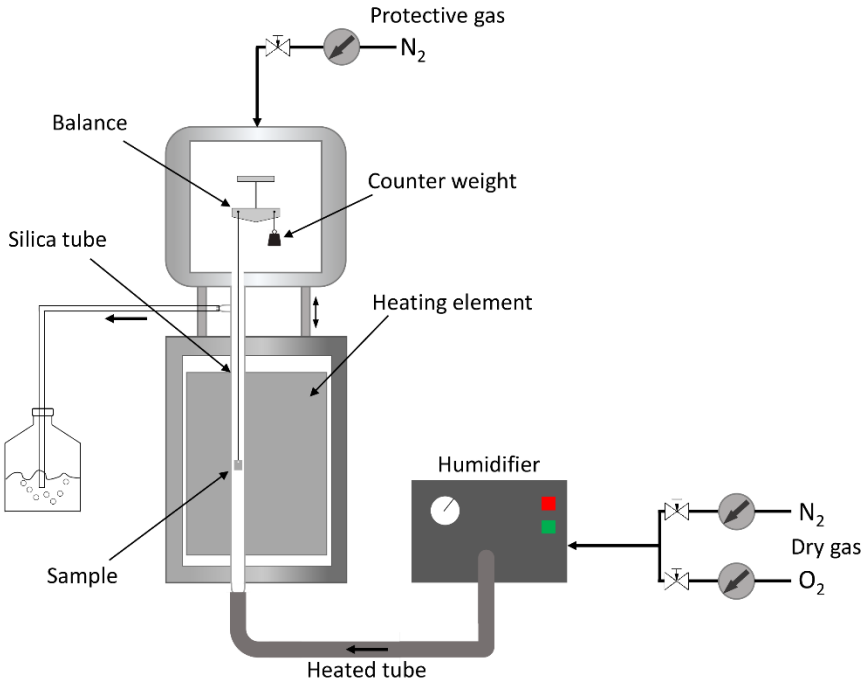

Figure 17: Schematic illustration of the TGA system used in this study.

The balance of the thermobalance was connected to a suspension system (a series of hooks) and a counterweight. The sample coupon to be exposed was hung on the bottom hook before the system was closed. The balance was calibrated by adjusting the counterweight so that the net weight was as close to zero as possible. The balance chamber was flushed with nitrogen for a minimum of 10 minutes to ensure removal of oxygen and other impurities from the air before starting the exposure. The exposure program was started when all cold spots in the TGA system had been insulated. A water vapor content of 20 vol% was used when humidity was desired. To achieve this, the relative humidity on the humidifier (Wetsys system) was set to 65%. The gas flow rate utilized was 15 ml/min, which corresponds to about 1.5 cm/s (at 600 °C with the inner diameter of the silica tube being 17 mm). The reason for the low flow rate in the thermobalance compared to the tube furnace is that a higher flow rate may cause turbulence, which would influence the quality and accuracy of the TGA measurement.

6.1.2 Model alloys

Model alloys, in which the amounts of certain elements were varied separately, were produced to investigate the effects of different alloying elements on the high temperature corrosion behavior of

FeCr(Al) alloys. The production procedure consisted of initially melting the raw materials in a vacuum induction furnace into a 1 kg ingot. This ingot was later hot-rolled into a strip and further machined to a thickness of about 2 mm. The strip was also heat treated at 950 °C to achieve a more even grain size distribution. The heat-treated alloy strips were cut into coupons with the dimensions of 10x12 mm (for tube furnace exposure) and 5x8 mm (for thermobalance exposure). A small hole with a diameter of 1.5 mm was drilled into the sample coupons, which simplified the weighing procedure and the deposition of salt. The hole was also necessary for attaching the sample coupon to the suspension system in the thermobalance. The sample coupons were ground with SiC paper (P500 to P4000) and then polished with a diamond suspension (3 µm followed by 1 µm) until a mirror-like surface had been achieved. To remove grease and dirt from the polishing, the samples were degreased with acetone and cleaned in an ultrasonic bath in separate tubes containing acetone. The samples were then cleaned with ethanol to remove any remaining acetone spots.

Two sets of model alloys have been distinguished by their Si content, i.e. model alloys with and without Si. The set of alloys without Si consists of the three matrices of FeCr (Table 1) and FeCrAl (Table 2 and Table 3) model alloys.

Table 1: Nominal chemical composition (wt-%) of the FeCr model alloys.

Alloy	Fe	**Cr**
Fe**2.25Cr**	Bal.	2.25
Fe**10Cr**	Bal.	10
Fe**18Cr**	Bal.	18
Fe**25Cr**	Bal.	25

Table 2: Nominal chemical composition (wt-%) of the FeCrAl model alloys (with varying Cr content).

Alloy	Fe	**Cr**	Al
Fe**5Cr**3Al	Bal.	5	3
Fe**10Cr**3Al	Bal.	10	3
Fe**18Cr**3Al	Bal.	18	3
Fe**25Cr**3Al	Bal.	25	3

Table 3: Nominal chemical composition (wt-%) of the FeCr(Al) model alloys (with varying Al content).

Alloy	Fe	Cr	**Al**
Fe18Cr	Bal.	18	0
Fe18Cr**1Al**	Bal.	18	1
Fe18Cr**3Al**	Bal.	18	3
Fe18Cr**6Al**	Bal.	18	6

The FeCr(Al) alloys were exposed to dry O_2 (5% O_2 + 95% N_2) in the presence of K_2CO_3 at 600 °C for 48 hours in a thermobalance. The alloys were also exposed to dry O_2 (5% O_2 + 95% N_2) in the absence of K_2CO_3 at 600 °C for 24 hours in a tube furnace. Prior to the thermobalance exposures, K_2CO_3 was deposited on the sample surfaces by spraying a water solution containing dissolved K_2CO_3 while warm air was continuously blown on the sample surface to accelerate evaporation of the solution. The samples were weighed both before and after spraying using a Sartorius™ balance with microgram resolution to measure the amount of salt deposited. This procedure was repeated until an amount of 1 mg/cm^2 had been deposited on the sample surfaces. To prevent moisture from being absorbed by

the salt, the sprayed samples were stored in a desiccator until they were inserted into the thermobalance. For the tube furnace exposures, the samples were weighed before and after exposure to record the mass gain.

The FeCrAlSi model alloys were divided into two matrices in which Si and Cr content were varied separately (Table 4 and Table 5, respectively).

Table 4: Nominal chemical composition (wt-%) of the FeCrAl(Si) model alloys (with varying Si content).

Alloy	Cr	Al	**Si**	Zr
FeCrAl**0Si**	10	4	0	0.29
FeCrAl**1Si**	10	4	1	0.29
FeCrAl**2Si**	10	4	2	0.29

Table 5: Nominal chemical composition (wt-%) of the FeCrAlSi model alloys (with varying Cr content).

Alloy	**Cr**	Al	Si	Zr
Fe**5Cr**AlSi	5	3	2	0.29
Fe**10Cr**AlSi	10	3	2	0.29
Fe**15Cr**AlSi	15	3	2	0.29
Fe**20Cr**AlSi	20	3	2	0.29

The FeCrAl(Si) model alloys were exposed in both a tube furnace and a thermobalance. The tube furnace exposures were performed in wet O_2 (5% O_2 + 20% H_2O + N_2(bal.)) both in the absence and presence of KCl at 600 °C for 168 hours. In addition, the alloys in Table 4 were exposed at the same temperature and for the same amount of time in dry O_2 (5% O_2 + 95% N_2). The thermobalance exposures were performed in wet O_2 (5% O_2 + 20% H_2O + N_2(bal.)) in the presence of KCl at 600 °C for 48 hours. Prior to the salt exposures, KCl was deposited on the sample surfaces by spraying a 20:80 water-ethanol solution containing dissolved KCl while warm air was continuously blown on the sample surface to accelerate evaporation of the solution. The amount of deposited salt was measured, and the procedure was repeated until an amount of 1 mg/cm^2 KCl had been achieved. KCl-sprayed samples were stored in a desiccator until they were inserted into the thermobalance or tube furnace. The samples exposed in the absence of KCl (wet and dry O_2) were weighed before and after exposure to record the mass gain. Due to high evaporation rates of KCl at 600 °C, the salt was deposited on gold foils and exposed under the same conditions to record the mass loss due to the evaporation of KCl.

6.1.3 Coatings

Two different types of coating techniques were utilized, namely, overlay welding and thermal spraying with HVAF.

6.1.3.1 HVAF-sprayed coatings

The thermally sprayed coatings were produced by HVAF-spraying (described in section 3.2) them onto a 16Mo3 substrate using an HVAF gun (Uniquecoat M3^{TM}, Oilville, VA, USA). Prior to spraying, the 16Mo3 substrates were grit blasted with alumina particles (63±10 µm) to cleaning and roughen the surfaces to ensure good adherence to the coating. A 16Mo3 rod with a length of half a meter was fixed in a horizontal rotating mandrel to apply the coating on the mantel area of the rod. After the coating had been applied, the rod was cut into pieces with a thickness of 5 mm. The coatings were then applied onto the flat faces of the cut pieces to ensure that the samples were coated on all sides, leaving no part of the substrate exposed. All coatings were sprayed to a thickness of roughly 250 µm. The surfaces

were coarse after the coatings had been deposited onto the substrate. For this reason, the coating surfaces were ground with SiC paper (500 grit to 4000 grit) to simplify both gravimetrical and microstructural analysis.

The compositions of the coatings and the substrate are shown in Table 6 and Table 7, respectively. Three different coating chemistries were selected, NiCr, NiAl and NiCrAlY, to investigate the performance of a chromia forming coating, an alumina forming coating and one that was both.

Table 6: Composition of the investigated coatings.

Powders	Chemical composition (wt%)				
	Ni	Cr	Al	Y	O
NiCr	78.6	21.3	-	-	0.1
NiAl	94.1	-	5.7	-	0.2
NiCrAlY	Bal.	21.2	7.3	0.9	0.2

Table 7: Composition of the substrate on which the coatings were deposited.

Substrate	Chemical composition (wt%)					
	Fe	Cr	Mo	Mn	Si	C
16Mo3	Bal.	0.1	0.3	0.5	0.3	0.15

The HVAF-coated samples were exposed to wet O_2 (5% O_2 + 20% H_2O + N_2 (bal.)) both in the absence and in the presence of KCl at 600 °C for 168 hours in a tube furnace (with a gas flow of 2.5 cm/s). Prior to the salt exposures, KCl was deposited onto the coating surfaces by spraying a 20:80 water-ethanol solution containing dissolved KCl while warm air was continuously blown on the sample surface to accelerate evaporation of the solution. The samples were weighed before and after spraying, using a Sartorius™ balance with 5 decimal accuracy (samples too heavy for the higher accuracy balance used for the model alloys and overlay-welded coatings), and the procedure was repeated until an amount of 1 mg/cm^2 KCl had been deposited. For the reference exposures, the samples were weighed (with the same balance) before and after exposure to record their mass gain.

6.1.3.2 Overlay-welded coatings

The overlay welded coatings used in this study were produced by Kanthal. Three different alloys (see Table 8) in the form of wires were welded onto a 4 mm thick Super VM12 (SVM12) steel plate using the Pulse Multi Control (PMC) technique. Because of its relatively low thickness, the substrate was welded onto a 50 mm thick steel block before overlay welding to reduce stress formation and prevent potential deformation during the overlay welding process. The overlay welded steel plates were cut into coupons with dimensions of 20x10x4 mm. Since only one face of the coupons was covered by overlay welding, a slurry coating was applied to the non-covered sides to prevent rapid corrosion of the substrate during the exposure. Thus, only the overlay welded face of the coupons was considered when gaging the corrosion resistance.

Table 8: Nominal composition of alloys used for overlay welding.

Alloys	Fe	Cr	Al	Ni	Si	Mo	Nb/Ta
FeCrAl197	bal.	12.4	3.7	-	1.3	-	-
Kanthal APMT	bal.	21	5	-	max. 0.7	3	-
IN625	5	20-23	-	bal.	max. 0.5	8-10	3.15-4.15

The overlay welded coatings and the uncoated Super VM12 (as a reference) were exposed to wet O_2 (5% O_2 + 20% H_2O + N_2 (bal.)) in the presence of KCl at 600 °C for 500 hours in a tube furnace. Prior to the exposures, the samples were placed on a hot plate while a 20:80 water-ethanol solution containing dissolved KCl was sprayed onto the coating surfaces, to deposit the KCl. The samples were weighed before and after spraying, using a Sartorius™ balance with 6-decimal accuracy to measure the amount of deposited KCl. The procedure was repeated until an amount of 0.5 mg/cm^2 KCl had been deposited. The samples were placed on an alumina sample holder with the uncoated surface face down. The uncoated Super VM12 samples were placed standing in the slits of the sample holder. To ensure that KCl remained on the surface of the samples for the entire exposure, an alumina boat filled with KCl was placed in front of the samples. This was done to saturate the gas flow with KCl(g) to reduce the evaporation rate from the samples. The gas flow was also set to 0.1 cm/s, which was based on previous KCl evaporation tests.

6.2 Field studies

Research was conducted in both a waste-fired boiler and a biomass-fired boiler. In the former, model alloys similar to the low-purity set investigated in the laboratory set-up were exposed to investigate if trends observed in the laboratory environment could also be observed in the much more complex environment. In the latter, commercial alloys and newly developed alloys and coatings (HVAF-sprayed) were investigated in a milder boiler environment (in comparison to waste-fired boilers). The upcoming sections describe the experimental procedure for these studies.

6.2.1 Waste-fired boiler

Air-cooled sample probes were inserted into the boiler through specially designed holes to expose the samples. The samples were attached onto the sample probes in the form of rings (with a narrow slit to enable bending, simplifying attachment and removal). The FeCrAl model alloys were produced by Kanthal by induction heating and casting in a copper mold in a protective argon atmosphere, resulting in cylindrical ingots. The ingots were machined to remove surface defects and then forged at 900 °C during which they were pressed into the form of pucks. The pucks were then made into rings, with an inner diameter of 3.3 cm and a thickness of roughly 2 mm, by lathe machining, see Figure 18.

Figure 18: Picture of a finished sample ring, used for probe exposures in the field-studies.

The compositions of the FeCrAl model alloys, in which the Cr and Si contents were varied, are shown in Table 9.

Table 9: Nominal chemical composition (wt-%) of the FeCrAl model alloys exposed in the waste-fired boiler.

Alloys	Fe	Cr	Al	Si	Zr
Fe5CrAl2Si	bal.	5	3	2	0.29
Fe10CrAl2Si	bal.	10	3	2	0.29
Fe15CrAl2Si	bal.	15	3	2	0.29
Fe20CrAl2Si	bal.	20	3	2	0.29
Fe10CrAl0Si	bal.	10	3	0	0.29

In addition to the model alloys, a 16Mo3 (Fe bal., 0.01 wt% Cr, 0.3 wt% Mo, 0.5 wt% Mn, 0.3wt% Si) sample ring (produced in the same way as the FeCrAl model alloys) overlay-welded with Inconel 625 (Ni bal., 20-23 wt% Cr, 8-10 wt% Mo, 3.15-4.15 wt% Nb+Ta) was exposed as a reference material.

The exposures were performed at the AffaldPlus plant in the Babcock & Wilcox Vølund boiler which is a grate-waste-fired boiler with a thermal capacity of 27 MW. The exposures were performed over the grate at the new steamboost position during a test of boiler settings, which gave a highly corrosive environment with high flue gas temperature (about 1000 °C) and relatively high levels of Cl, resulting in a highly corrosive environment. More information about the environment at the steamboost position can be found in [85, 86].

Prior to exposure, the thickness of each sample ring was measured at eight points around the ring using an Olympus 38DL PLUS Ultrasonic thickness gage. Because of the uneven nature of overlay welding, thickness measurements were not performed on the Inconel 625 overlay-welded sample ring. The air-cooled probes, used for exposure of all investigated materials, had two temperature zones with separate thermocouples for regulating the temperature in each zone. The material temperature of each zone was controlled with a PID (Proportional-Integral-Derivate) controller, and pressurized air was used as the cooling agent to achieve a material temperature of 600 ±3°C. The probe was designed to hold a total of 8 samples, 4 samples in each temperature zone, see illustration in Figure 19.

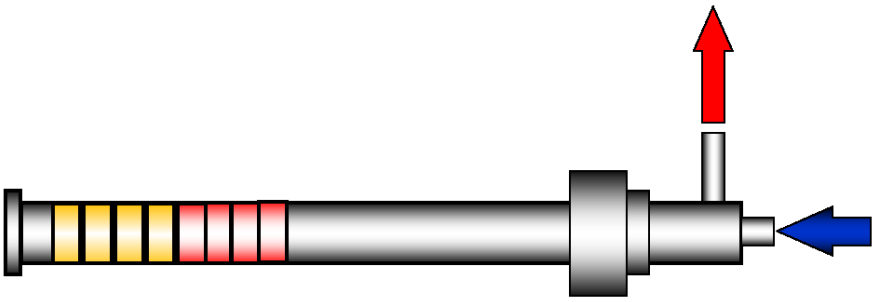

Figure 19: Schematic illustration of the air-cooled probes used in the field-studies. The yellow and red areas illustrate the two different temperature zones (with four sample locations in each). The blue and red arrows represent the cold inlet and the warm outlet for air, respectively.

A deposit test was performed prior to the exposure to gage the corrosivity of the boiler environment, and to determine the S/Cl ratio. Rings made of Sanicro 28 were exposed for 2 h for the deposit test. After removing the probe, the sample rings were detached along with the deposit and stored in a desiccator until ion chromatography (IC) could be performed. The corrosion test was initiated immediately after the deposit test and lasted for 672 h. After exposure the sample rings were removed from the probe and stored in a desiccator.

6.2.2 Biomass-fired boiler

This field-study was performed at the commercial grate-fired Combined Heat and Power (CHP) boiler (154 MW) at the Skaerbaek Power Plant (designed and manufactured by Babcock and Wilcox Vølund and operated by Örsted A/S) in which mainly wood chips are combusted. The procedure for producing and preparing the sample rings and the utilization of air-cooled sample probes, were the same as described in the previous section. Three commercial stainless steels (347H, 310, Sanicro 25), three different FeCrAl model alloys (see Table 10), and a 347H sample ring, thermally sprayed (HVAF) with an enhanced version of FeCrAl 197 (4.9 wt-% Al and 1.9 wt-% Si), was exposed.

Table 10: Nominal chemical composition of FeCrAl model alloys exposed in the biomass-fired boiler

Model Alloys	Fe	Cr	Al	Si
FeCrAl197	bal.	12.4	3.7	1.3
FeCrAl0Si	bal.	10	4	0
FeCrAl2Si	bal.	10	3	2

The exposures were performed for a total of 168 hours at two superheater locations with different flue gas temperatures. At each location, the rings were exposed to two different material temperatures, 600 °C and 700 °C, regulated by the air-cooled probes as described in the previous section. Prior to exposure, deposit tests were performed at each location and material temperature, resulting in four different deposits. The S/Cl ratio in the deposits were analyzed using IC to gage the corrosivity of the current boiler environment. The exposed sample and the deposit samples were stored in a desiccator until analysis.

6.3 Calculation of oxide thickness

Theoretical oxide thicknesses were calculated based on the mass gain of the exposed samples. The calculation was based on the assumption that the total mass gain originates from the density change due to the ingress of oxygen. The theoretical density change is given by Equation 6.1

$$\Delta\rho_{theoretical} = \rho_{M_xO_y} * \frac{M(O_2)}{M(M_xO_y)}$$ (Equation 6.1)

where $\rho_{M_xO_y}$ is the density of the oxide, and $M(O_2)$ and $M(M_xO_y)$ is the molar mass of oxygen gas and the oxide, respectively. Utilizing the definition of density:

$$\rho = \frac{m}{V}$$ (Equation 6.2)

where m is the mass gain (g/cm^2), and V is an arbitrary volume of the oxide, Equations 5.1 and 5.2 can be combined, resulting in Equation 5.3:

$$V\ cm^3 = d\ cm * 1\ cm^2 = \frac{m}{\rho_{M_xO_y} * \frac{M(O_2)}{M(M_xO_y)}}$$ (Equation 6.3)

where d is the oxide thickness on an area of 1 cm^2. Thus, the oxide thickness in µm is given by Equation 5.4:

$$d = \frac{m}{\rho_{M_xO_y} * \frac{m(O_2)}{m(M_xO_y)}} * 10000$$ (Equation 6.4)

7 Analytical techniques

Apart from calculating the mass gain of the exposed materials, several analytical techniques were used to investigate the degree of corrosion attack, the presence of corrosion products and their microstructure in order to determine the underlying mechanisms. This chapter describes the analytical techniques and procedures used in this study.

7.1 Microscopy

Visualizing the surface or cross section of a sample is of the utmost importance for understanding the corrosion process and the underlying mechanisms. The oxide scale thickness and microstructure, and the presence of other corrosion products, give essential information about what occurs during the exposure a sample. The initial conditions of the material are of equal importance, for which parameters, such as grain size, surface morphology and impurities, can be studied.

7.1.1 Optical Microscopy

In optical microscopy, the image is produced by utilizing photons aimed at the sample surface. The photons are reflected and refracted using lenses, which results in a magnified image of the sample. A Zeiss AXIO Vert. A1 equipped with an AxioCam ICc 1 (with ZEN blue edition software) was used to examine the material prior to exposure to obtain information such as grain size and the general microstructure. It is possible to acquire a general overview of the corrosion products formed on a sample surface by using optical microscopy, but it has certain limitations. The main limitation of optical microscopy is the comparatively large wavelength of the photons (390-700 nm) which results in images with a relatively low resolution (200 nm at best). Thus, it is not possible to examine the corrosion products in detail. To acquire images with higher resolution, it is necessary to utilize other techniques that are not limited by large wavelengths. One such type of instrument is electron microscopes, which utilizes electrons to visualize a sample surface.

7.1.2 Scanning Electron Microscopy (SEM)

An SEM is a type of microscope that utilizes electrons to visualize the surface of a sample. The wavelength of an electron is inversely proportional to the momentum of the electron, which in turn is directly proportional to the velocity of the electron. Because of the very low mass of an electron, the wavelength is much shorter than for photons when accelerated to high velocities, and therefore, SEM has a significantly higher resolution than optical microscopes. In practice, the resolution of an SEM is also determined by the width of the electron beam and the interaction volume of the electrons in a solid material (discussed below). The SEM system consists of an electron source from which electrons are emitted and later accelerated in an electron gun. Before reaching the sample surface, the electrons pass through a system of magnetic lenses and apertures. The main functions of these are to focus the electron beam and make the probe size, i.e. the size of the surface area hit by the electron beam, as small as possible while keeping the current of electrons as high as possible [87]. The electron beam scans across the material surface to obtain information about a larger area. It is important to maintain a high vacuum in the column and the sample chamber. If the vacuum is not high enough, the electron beam will interact with the gas molecules present, which can result in reduced resolution.

Various signals are generated and emitted when an electron beam interacts with a material. Among these are secondary electrons (SE), backscattered electrons (BSE) and X-ray photons. The depth from which the signals are emitted differs depending on the current of the incoming electron beam and the type of signal [88], see Figure 20. By using different types of detectors, different kinds of information can be obtained from the signals.

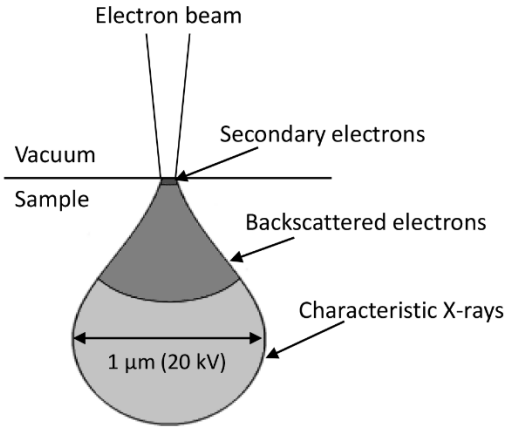

Figure 20: Illustration of the interaction volume from which different signals are emitted when using SEM (Based on [87]).

The secondary electrons have a low energy (< 50 eV) and can only escape from a small volume close to the surface. Thus, secondary electrons give the best resolution of the three different signals. The edges of surface features on a sample emit more secondary electrons than flat surfaces, which results in different contrast. Thus, the detection of secondary electrons is commonly used to visualize the topography of a sample surface [87].

Backscattered electrons have a higher energy than secondary electrons and can escape from a larger depth, which results in a lower spatial resolution. In addition to the accelerating voltage (beam current), the amount of backscattered electrons emitted depends on the composition, density, the presence of voids and the sample geometry [88]. A heavier material (higher atomic number) emits higher amounts of backscattered electrons. Thus, the detection of backscattered electrons is commonly used to visualize the distribution of different elements on a sample surface. A more porous area of the sample will appear in brighter contrast because less backscattered electrons are emitted. For crystalline samples, the contrast can be influenced by the orientation of the lattice. If the lattice is oriented in a way so that the incoming electrons encounter a low density of atoms, a fraction of these electrons will penetrate deeper into the crystal structure before being scattered [88]. The number of backscattered electrons is reduced in this way, and a darker contrast will be displayed for this area. This type of contrast is called electron channeling contrast and can be observed on very smooth metal surfaces on which different grains are distinguished by different contrasts because the lattice orientation of the metal grains differ, see Figure 21.

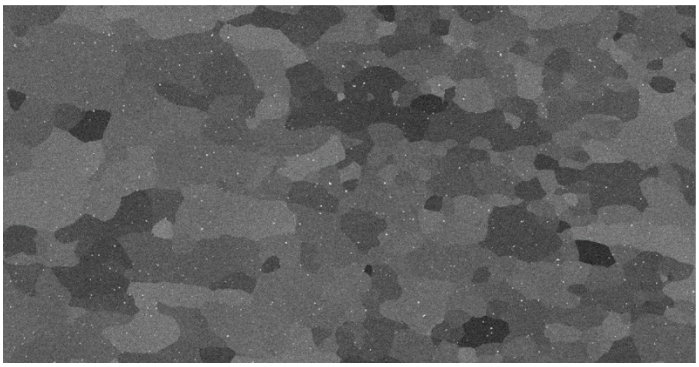

Figure 21: SEM-BSE image of a smooth metal surface. The grains are distinguished by the difference in contrast resulting from the different lattice orientations.

The third signal, X-ray photons, is different from the two other signals as it is not used to visualize a sample surface but instead to determine the elemental composition of a sample surface (and below

depending on the interaction volume). X-rays are produced when a high energy electron transfers a sufficient amount of energy to an atom to release an electron from an inner shell [87]. The atom can then relax by emitting energy in the form of an x-ray photon. The energy of the X-ray photon, emitted during the relaxation, is characteristic for the specific atom. Using an EDX (energy dispersive X-ray) detector, it is possible to distinguish which elements are present on the sample surface. However, since X-rays escape from an even greater depth than the backscattered electrons, the resolution is further reduced, which makes it difficult to analyze the elemental composition of very small features [88]. Some elements release X-ray photons with similar amounts of energy, that can impede the determination of the elemental composition. It is also important to always analyze an area with known composition to verify the accuracy of the EDX analysis.

An FEI Quanta 200 FEG ESEM equipped with an Oxford Instruments X-Max^N 80 T EDX detector was utilized and operated at accelerating voltages between 10-20 kV. In addition, a Leo ULTRA 55 FEG SEM was used (using ESB detector) with an accelerating voltage of 2 kV to achieve higher magnification images when analyzing small features.

7.1.3 Broad Ion Beam (BIB)

Prior to SEM analysis of sample cross sections, these were prepared using Broad Ion Beam (BIB) milling (not field samples). This results in a much smoother surface that further reveals microstructural features and makes it possible to more accurately analyze the cross section. The BIB instrument used was a Leica TIC 3X equipped with three argon guns. Before milling, one side of the sample was first sputtered with a thin gold layer followed by the attachment of a silicon wafer onto the sputtered surface with glue. After the glue had cured, the sample was cut using a low speed saw. Before inserting the sample into the BIB instrument, the cross section was carefully ground (with P1000 Si-C paper) to achieve an even cross section. The sample was then attached to a sample holder (either by using carbon tape or with silver paint) and inserted into the BIB instrument, see Figure 22. The stage was adjusted so that roughly 0.1 mm of the sample was not covered by the mask, see Figure 23. The instrument was mainly operated at 8 kV for 4-6 hours (sometimes longer due to worn out ion guns). When higher quality cross sections were required (for example for EBSD analysis, described in the next section), the instrument was operated at 4 kV and 2 kV for roughly four 4 hours at each setting in addition to 8 kV milling.

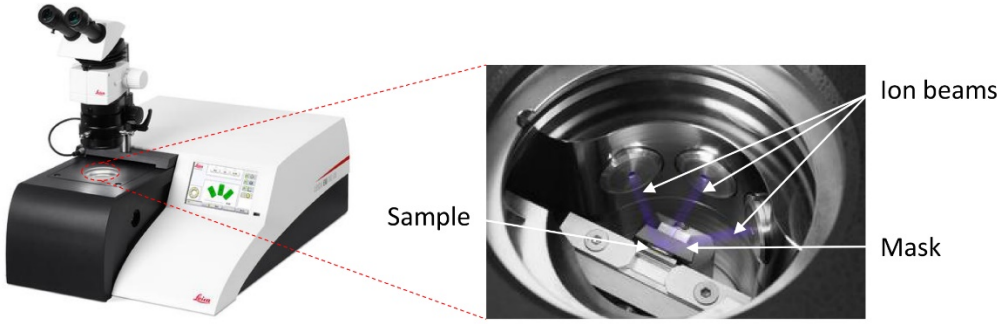

Figure 22: Picture of the BIB instrument used in this study (left). The picture to the right shows a sample attached to a sample holder hat has been placed on the instrument stage. Three ion guns are directed toward the sample, which is covered by a mask.

During the process, the ion beams mill the exposed part of the sample while the part of the sample covered by the mask remains unexposed as shown in Figure 23. This results in a smooth and clean surface that makes small microstructural features more distinguishable.

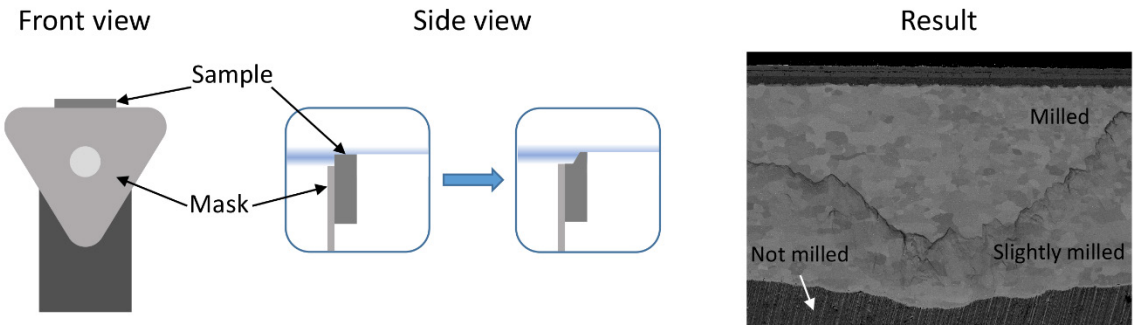

Figure 23: Schematic illustration of the BIB milling process (left) and SEM-BSE image of an exposed metal sample prepared with BIB milling (right). The degree of milling can be distinguished in the SEM image.

7.1.4 Electron Backscatter Diffraction (EBSD)

EBSD is an SEM-based technique used to obtain crystallographic information about a crystalline sample. For conventional EBSD, the sample surface normal is tilted 70° from the electron beam axis to maximize signal intensity, which improves the signal-to-background ratio in the diffraction pattern thereby improving the sensitivity for detection [89]. Upon interaction between the electron beam and the sample, backscattered electrons, satisfying Bragg's law (see Equation 7.1 in section 7.2), fluoresce a phosphor screen, producing characteristic Kikuchi bands. Microstructural information such as grain size, shape and orientation, localized strain and phase identification can be extracted from the Kikuchi bands. A representative diffraction pattern of a FeCrAl alloy is shown in Figure 24, displaying the Kikuchi bands of the Body-Centered Cubic (BCC) phase.

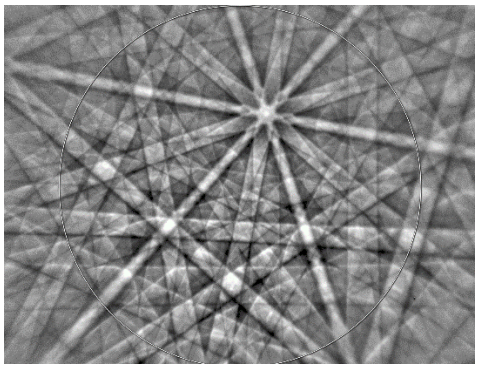

Figure 24: EBSD-pattern of a BCC phase in a FeCrAl alloy.

Kikuchi bands are characteristic of both the crystal structure and crystal orientation in the region where they were generated and can be used to distinguish between different grains and determine phases. When the electron beam is scanned over a polycrystalline sample, spatial images/maps obtained using this technique provide information about different crystal orientation and phases in the sample region. The miller indices may be acquired from the diffraction patterns with a computer software linked to the microscope, generating a map that displays differences in crystal orientation. A typical example of such a map is shown in Figure 25.

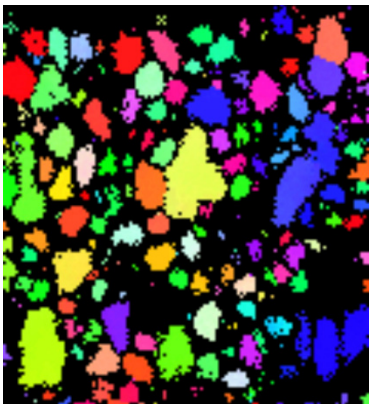

Figure 25: EBSD map displaying differences in grain orientation (different colors), used for distinguishing between different grains.

A Tescan GAIA3 Dual Beam FIB-SEM equipped with an Oxford Instruments NordlysNano Camera, was used for EBSD analysis, which was performed by Dr Imran Hanif to determine crystallographic phases and grain size. All EBSD analysis were carried out with an operating voltage of 20 keV, while other parameters were suitably adjusted based on the sample surface. BIB milling was performed as described in section 7.1.3 prior to EBSD analysis.

7.1.5 Focused Ion Beam (FIB)

Focused Ion Beam (FIB) milling is a powerful tool for site specific milling and deposition, particularly in materials science. Most corrosion products are routinely investigated using SEM-based techniques, but in certain cases, site specific milling is required. Reasons for doing this can be to examine the cross section underneath a specific corrosion product on a sample surface or to investigate the cause behind local differences in oxide scale thickness. Thin lamellae for TEM analysis can be prepared with a FIB system. In a FIB system, ions are produced from a liquid metal ion source (typically Ga) and accelerated towards the sample surface using voltages up to 30 keV. Electrostatic lenses and deflectors are used to focus and deflect the ion beam within the ion column. The ion current must be reduced for high-accuracy-milling since a too high ion current results in a wider distribution of the ions.

The principle for imaging using a FIB instrument is identical to that for SEM [87]. When ions hit the surface, it results in the emission of X-rays and secondary electrons. As with SEM, the latter can be detected to generate an image. The number of secondary electrons emitted depends on the ion current, accelerating voltage, composition of the examined area on the surface as well as surface topography. The resolution of ion induced secondary electron images are comparable to the resolution of SEM images but with better channeling and atomic number contrast due to higher secondary electron yield. When the ions interact with the crystals of the grains the number of secondary electrons emitted is affected by the orientation of the crystals which makes the different grains distinguishable (more so than with an SEM). However, FIB is a destructive technique which damage the visualized sample surface even when using lower currents [87].

An FEI Versa3D LoVac DualBeam FIB-SEM (with both an electron column and an ion column) system equipped with an Omniprobe and a Pt-deposition system for preparing thin lamellae for TEM analysis was used. Channeling contrast imaging was done by Amanda Persdotter to distinguish the oxide grains for the purpose of examining differences in oxide grain size, see Figure 26. Thin lamellae of ≤ 100 nm for TEM analysis were prepared by Dr Vijayshankar Asokan and Dr Imran Hanif.

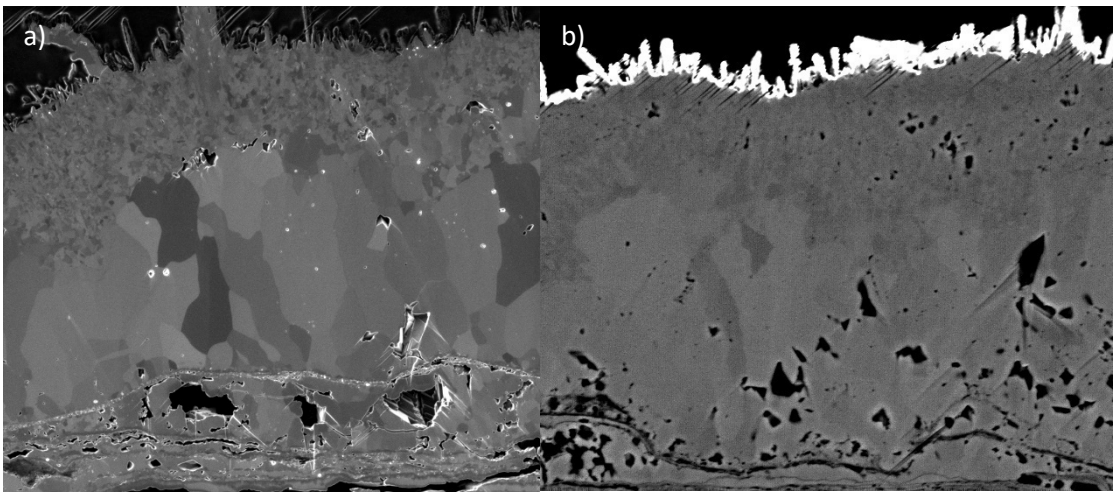

Figure 26: Two images of the same sample (not the same area), visualized using a) FIB (by Amanda Persdotter) and b) SEM (after BIB milling). The oxide grains were more distinguishable when FIB milling was used.

7.1.6 Transmission Electron Microscopy (TEM)

The principle of TEM differs from SEM in several important aspects. Similar to SEM, electrons are generated from an electron source, accelerated and directed towards the TEM-sample surface. However, in contrast to SEM in which the image is generated through the detection of backscattered or secondary electrons, it is the electrons that are transmitted through the sample that are of importance. The transmitted electrons are focused by an objective lens followed by utilization of a charge-coupled device (CCD) to generate an image. A sample must be electron transparent for electrons to be able to transmit through it, and consequently, the TEM lamella is usually ≤ 100 nm in thickness. SEM analysis gives information about specimen morphology, surface structure and chemical composition. Information about the internal structure of the samples and crystal structure can be obtained as well with TEM analysis. One of the main advantages of TEM analysis is that small sample features can be analyzed in more detail because of the higher resolution than obtained through SEM analysis. This is mainly due to the much smaller interaction volume for the former than in the latter. Similar to SEM, when performing EDX analysis it is of great importance to analyze a part of the sample that is of known composition to determine the accuracy of the elemental analysis. This is especially crucial when the thickness of the sample lamella is unknown since this can significantly influence the measured composition for certain elements.

An FEI Titan 80–300 equipped with an Oxford Instruments INCA X-sight EDX detector was used for all TEM investigations. TEM was operated in scanning TEM (STEM) and TEM mode under different conditions. STEM-EDX analysis was performed to determine the elemental distribution of certain corrosion products. High angle annular dark field (HAADF) imaging was also performed in STEM mode. In addition, electron diffraction patterns were obtained in TEM mode for phase determination.

TEM analysis was performed by Dr Vijayshankar Asokan to investigate thin oxide scales (in the nanometer range), while Dr Imran Hanif was responsible for the TEM analysis of samples that had formed thicker oxide scales (iron-rich oxide).

7.2 X-ray diffraction (XRD)

A complementary method for performing chemical analysis is X-ray diffraction (XRD). Compared to many other types of chemical analysis, which only detects the presence of the different elements, XRD is able to disclose the presence of specific compounds and/or phases on or in the examined sample with no or minor sample preparation.

The principle of XRD is based on interference between X-rays scattered by atoms in a crystal structure. When an incoming beam of X-rays (commonly referred to as incident beam) reaches a crystalline material, the X-rays will interact with and be scattered by atoms. Because the X-rays consist of wave motions with certain wavelengths, these can interfere with each other either constructively or destructively [90]. Constructive interference occurs when two X-rays are in phase with each other, which results in them reinforcing each other. Destructive interference occurs when the X-rays are instead out of phase, which results in them cancelling out each other, see Figure 27.

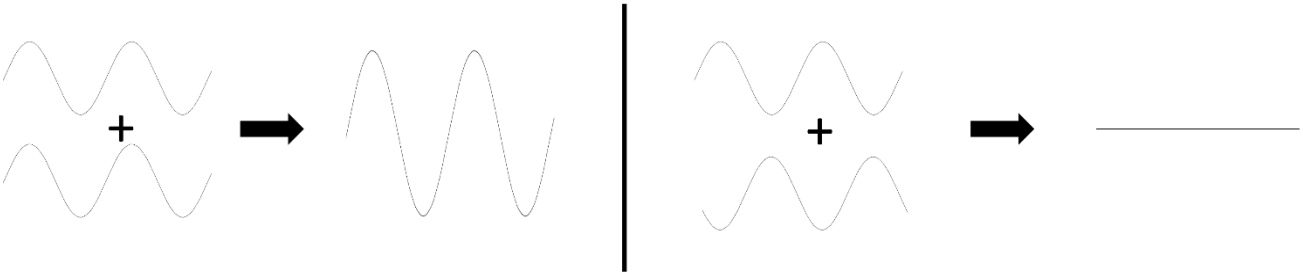

Figure 27: Schematic illustration of constructive (left) and destructive (right) interference between waves.

A schematic illustration of the scattering of X-rays by atoms in a crystalline material is shown in Figure 28. The incident X-ray beam is scattered by atoms in three crystal planes (A, B and C). Since the atoms in the crystalline material are arranged periodically in a lattice, there is a definite phase relation between the scattered waves [90]. Thus, for constructive interference to occur, the path difference, αβγ, of two X-rays must be equal to a whole number n of the wavelength of the X-ray.

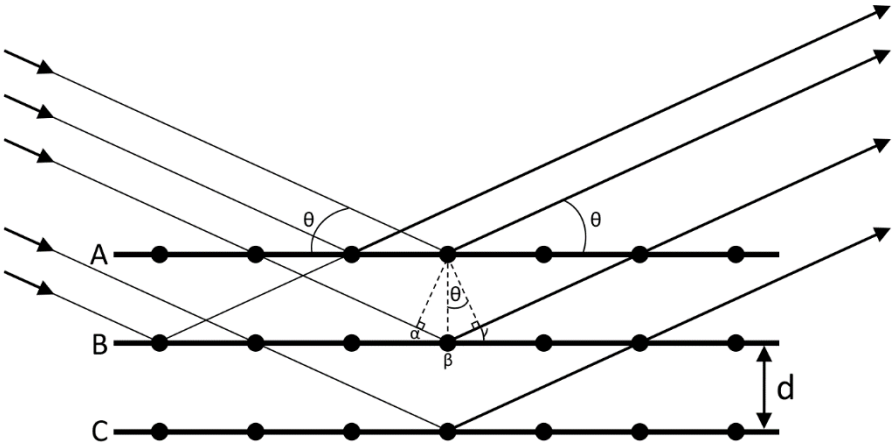

Figure 28: Schematic illustration of diffraction of an X-ray beam by atoms in several crystal planes (based on [90]).

The necessary conditions were mathematically expressed by W.L. Bragg in 1913, which resulted in Bragg's law:

$$n\lambda = 2d \cdot sin\theta \qquad \text{(Equation 7.1)}$$

where n is a whole number, λ is the wavelength of the incoming X-rays, d is the interplanar spacing in the lattice and θ is the incident angle of the incoming X-rays. Most incident angles result in destructive interference.

When analyzing a crystalline material with a diffractometer, the incident angle slowly increases from one value to another. The diffracted X-rays are detected and registered while varying the incident angle, resulting in a spectrum of peaks at incidence angles where constructive interference occurs. This spectrum is characteristic of a specific compound or phase. Spectra of a vast number of compounds

have been recorded and stored in a database, which is used when analyzing the composition of unknown or partially unknown samples.

A Siemens D5000 diffractometer was used as a complement to the EDX analysis and electron diffraction (with TEM and EBSD) used in the present study to analyze the corrosion products of the FeCrAl alloys. When analyzing thick oxide scales (micrometer range), the XRD program consisted of a locked couple scan ranging from 2θ=0° to 80°. For thin oxide scales (in the nanometer range), the XRD program consisted of a detector scan from 2θ=10° to 90° with an incidence angle of 0.2°.

7.3 Thermodynamic modelling

Thermodynamic calculations are a complementary tool for understanding mechanisms involved in the corrosion process. Thermodynamic calculations of material properties has been used for decades to predict stable phases in different systems [91]. The concept of this method is to define the conditions, e.g. temperature, pressure, composition of phases, in such a way that the degree of freedom equals zero. The energy of a system can be calculated once the state of that system is defined, i.e. the degree of freedom is zero. Different types of energies can be calculated based on the defined conditions, i.e. Helmholtz, Gibbs, etc. Gibbs energy is very convenient as it is defined in constant volume, which is the case for most chemical processes.

The equilibrium in a system is reached when the variation of the Gibbs free energy relative to an internal parameter is at its minimum; this is the basis of the Calphad (CALculation of PHase Diagrams) approach. Calphad-based software use this criterium to predict material properties, such as equilibrium phases, the composition of phases and the activities of elements under the defined conditions. Different software, e.g. Thermo-Calc, Factsage, Pandat, use this method to evaluate thermodynamic properties with models developed based on experimental data. Equation 7.2 is used in Thermo-Calc to express the molar Gibbs energy of a multi-component system:

$$G_m = {}^{srf}G_m + {}^{phys}G_m - T * {}^{cnf}S_m + {}^{E}G_m \qquad \text{(Equation 7.2)}$$

where ${}^{srf}G_m$ is the surface of reference (see Figure 29) and represents the Gibbs energy of an unreacted mixture of the components, ${}^{phys}G_m$ is the contribution to the Gibbs energy from physical phenomena (such as magnetic transitions), $T * {}^{cnf}S_m$ is the contribution from the configurational entropy based on ideal mixing of the components and ${}^{E}G_m$ is the excess Gibbs energy, i.e. the deviation from the ideal solution.

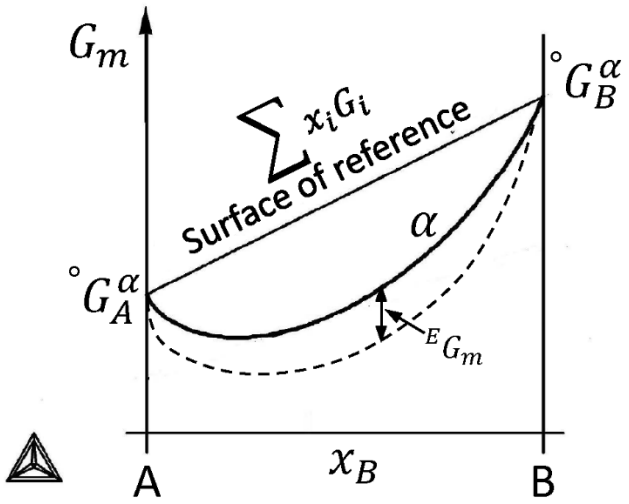

Figure 29: A molar Gibbs energy diagram for a mixture of two components, A and B, in phase α. The solid curve represents the real Gibbs energy while the dashed curve represents the Gibbs energy from the three first terms in Equation 7.2.

For two phases in equilibrium at constant pressure and temperature, the compositions of the phases, $x_B^{\alpha/\beta}$ and $x_B^{\beta/\alpha}$, are given by the minimum of Gibbs energy for each phase, see Figure 30. The chemical potentials, $\mu_A^{\alpha+\beta}$ and $\mu_B^{\alpha+\beta}$, for each component in the two-phase system are given by the intersections of the common tangent for these minima with the component axes. The Thermo-Calc software utilizes the description of the phases in the databases (optimized based on experimental data) to produce phase diagrams, as illustrated in Figure 31.

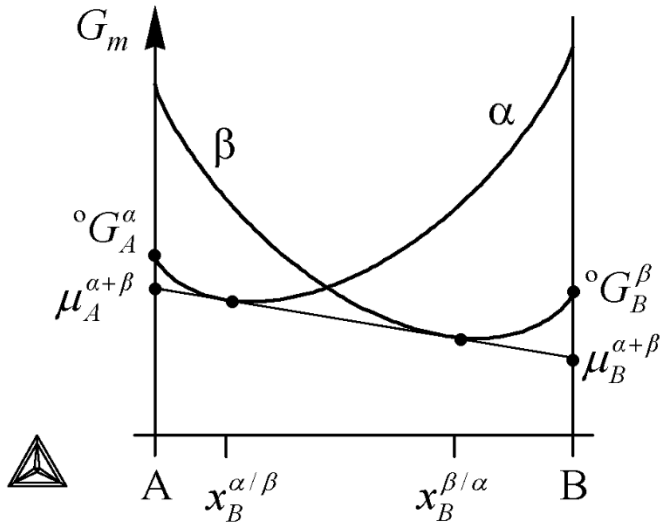

Figure 30: Common tangent construction for finding the equilibrium between two phases, α and β, at constant pressure and temperature.

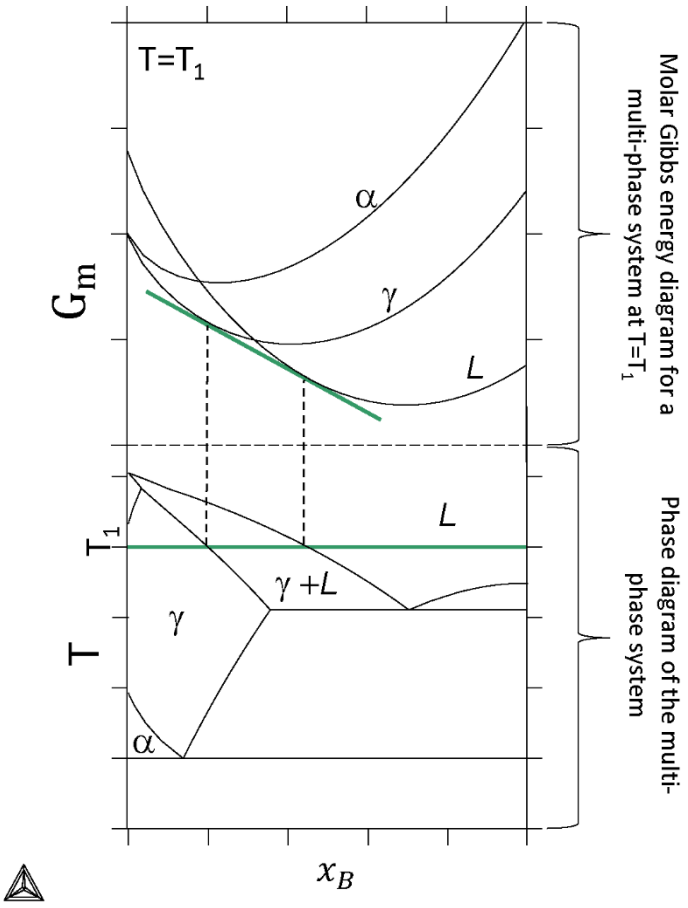

Figure 31: Schematic illustration of how a phase diagram of a multi-phase system can be computed from the molar Gibbs energy of each phase at different temperatures and constant pressure.

Recent developments of models for Calphad software have enabled thermodynamic and kinetic modelling of some oxidation processes at high temperatures in simple environments (O_2) [92-94]. The Dictra module in the Thermo-Calc software is used to simulate the oxidation process by using two different models: the moving phase boundary model [95] and the homogenization model [96]. In the latter, the calculation domain is divided into cells in which local equilibrium is assumed. The local chemical potential in each cell, attained through equilibrium calculations, results in a chemical potential gradient over the domain, providing the driving forces for diffusion.

Thermodynamic calculations were performed by Dr Sedigheh Bigdeli using Thermo-Calc and Dictra to understand the influence of certain elements on alloy/oxide properties, such as stable oxide phases and equilibrium composition and the activities and mobilities of different elements.

8 Results and discussion

The corrosion resistance of FeCr(Al) model alloys in corrosive environments of varying harshness, and the influence of different alloying elements on the corrosion behavior were investigated. Since the mechanical properties of FeCrAl alloys are known to be relatively poor, the performance of different types of coatings was studied to gage the potential of using these for mitigating the corrosion attack and possible complications associated with utilizing coatings. This study includes field investigations in biomass- and waste-fired boilers in order to connect the observations and trends from the laboratory studies to the intended applications. The results from the studies will be presented and discussed in the following sections. Note that the presented concentrations of elements in the various kinds of corrosion products are presented as cationic concentrations (cat%) in the upcoming sections, i.e. oxygen is always excluded. The reason for this is the technical difficulties in quantifying lighter elements such as oxygen.

8.1 A new perspective on corrosion resistance

A new approach was presented in chapter 5, in which the corrosion behavior of iron-based alloys is divided into two regimes, the primary and secondary corrosion regimes. The corrosion resistance in the primary corrosion regime, i.e. the primary protection of an alloy, is dependent on the formation of a slow-growing oxide scale, such as chromia or alumina. The corrosion resistance of an alloy in the secondary corrosion regime, i.e. the secondary protection of an alloy, is instead dependent on the oxidation behavior of the faster-growing iron-rich oxide scale that forms after breakaway oxidation. The criteria for achieving a high corrosion resistance largely depend on the corrosion regime in which a material will belong to during the majority of the operating lifetime. The potential of improving the primary and secondary protection by optimizing the alloying composition will be discussed in the following sections.

8.1.1 The primary protection

The primary protection of an alloy, mostly known as “the protective oxide scale”, is desired in a range of applications to reduce material degradation and retain specific properties. To form a primary protection, the alloy must to contain certain amounts of Cr and Al to form Cr- and/or Al-rich scales, respectively. Generally, an alloy containing large amounts of Cr and Al can more easily form these types of scales and is also better at retaining the formed scale. Meanwhile, an elevated concentration of Cr and Al in the alloy can result in poor mechanical properties, which are crucial for many applications. Altering the Cr and Al contents to achieve a balance between corrosion properties and mechanical properties is therefore of the utmost importance.

A broad range of FeCr(Al, Si) model alloys were exposed in dry O_2 and wet O_2 (5% O_2 + N_2 (bal) and 5% O_2 + 20% H_2O + N_2 (bal)) at 600 °C for up to 168 hours as described in section 6.1.2. The results from these exposures are described in more detail in Papers I, III, IV and V. The most important outcomes are presented and discussed below.

The majority of the FeCr(Al) model alloys, except Fe2.25Cr and Fe5Cr3Al, displayed a very low mass gain when exposed in dry O_2 at 600 °C for 24 hours, which indicates the formation of a primary protection, see Figure 32. The inability of Fe2.25Cr and Fe5Cr3Al to rapidly form a primary protection was expected since chromia-forming steels are generally known to require a minimum Cr content of around 12 wt% to form a Cr-rich oxide scale. Additionally, the Fe5Cr3Al alloy is below the optimal range of FeCrAl alloys to form a Cr and/or Al-rich oxide scale [97]. However, the significantly lower mass gain of Fe5Cr3Al than of Fe2.25Cr indicates that a protective oxide scale formed on Fe5Cr3Al after the initial rapid oxidation. Keeping a FeCr(Al) alloy lean, i.e. maintaining relatively low amounts of Cr and Al, is beneficial for reducing the negative influence of these alloying elements on mechanical properties,

fabricability and price. However, lean FeCrAl alloys tend to lose their primary protection in humid environments because of their inability to form an Al-rich oxide scale or to sustain a Cr-rich oxide scale because of the volatilization of Cr (see section 4.5.1) [97, 98]. To improve the primary protection of lean FeCr(Al) alloys at medium-high temperatures (about 600 °C), the microstructure of the oxide scale(s) formed on the surface of these must be further understood.

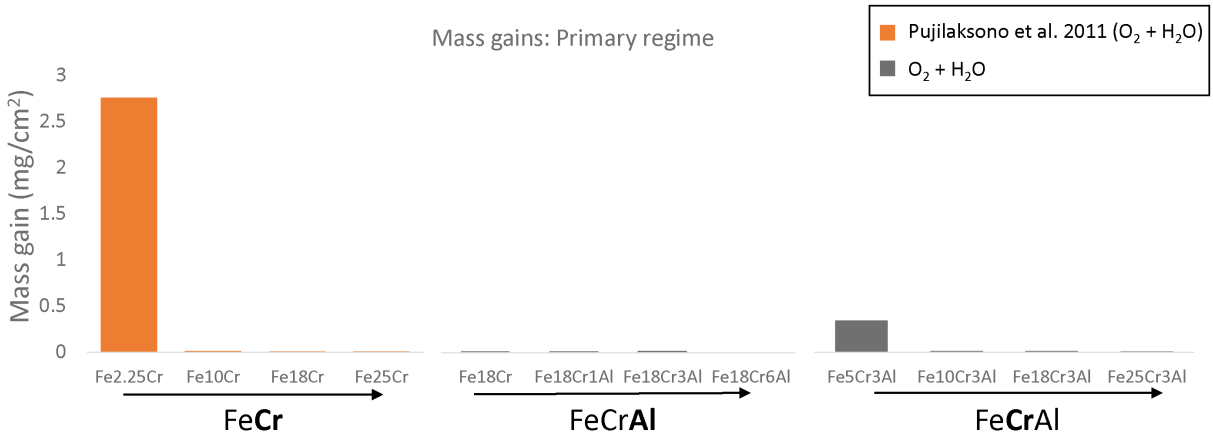

Figure 32: Average mass gains of FeCr(Al) model alloys after exposure to 5% O_2 + N_2 (bal.) at 600 °C for 24 hours.

The lean FeCrAl alloy, Fe10Cr4AlRE (denoted FeCrAl0Si in Table 4), was exposed to the same environment as the alloys mentioned above for 24 and 168 hours after which it displayed mass gains in the same range, i.e. it has formed a primary protection, see Figure 33. However, it was found that the surface morphology of FeCrAl0Si was not homogeneous. Some grains behaved less protectively and had formed an iron-rich oxide while the rest behaved protectively and had retained the primary protection. Nevertheless, the number of iron-oxide-covered grains did not increase significantly between the 24-hour and 168-hour exposures, but a change in surface morphology was observed.

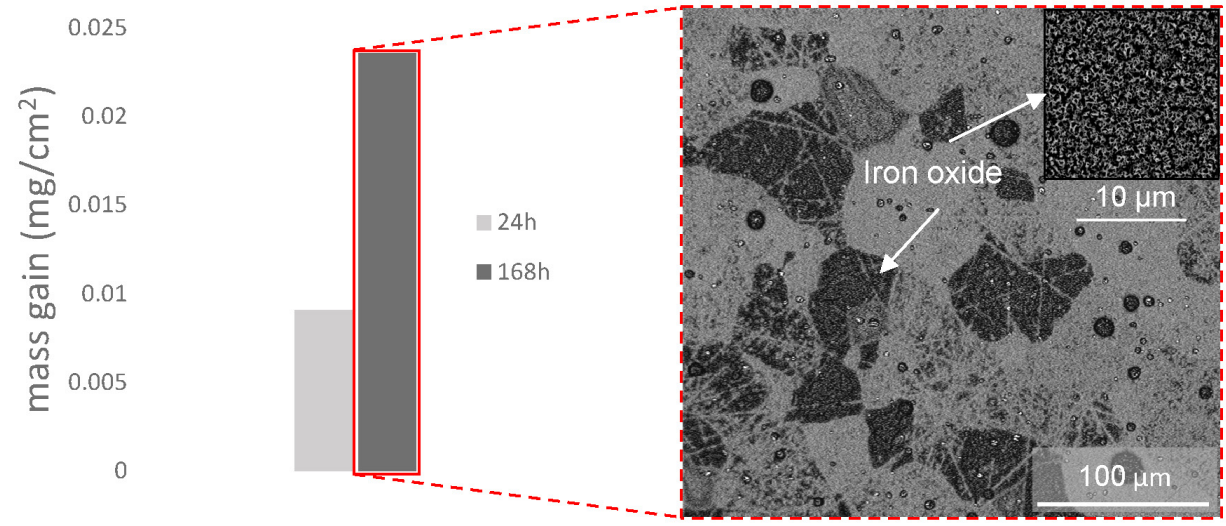

Figure 33: Average mass gain (left) of FeCrAl0Si after exposure to 5% O_2 + N_2 (bal.) at 600 °C for 24 and 168 hours (SEM-BSE plan view image after 168 hours on the right).

Lifting out a section of an iron-oxide-covered grain and performing STEM analysis revealed that an Al-rich oxide scale (50-75 nm) had formed underneath the iron-rich oxide scale (80-130 nm), see Figure 34. This indicates that the propagation of the iron-rich oxide scale was inhibited by the formation of a healing layer. One of the protective grains was also analyzed with STEM. The analysis showed that the grain had formed a 40-75 nm thick protective oxide consisting of somewhat overlapping Cr- and Al-

rich layers (up to 40 cat% Cr and up to 60 cat% Al), see Figure 35. Iron oxide nodules had formed evenly distributed on the surface of both the protective and less protective grains and seemed to originate at the RE particles protruding from the surface. The less protective grains and the protruding RE-particles may act as nucleation sites for breakaway oxidation (transition into the secondary corrosion regime).

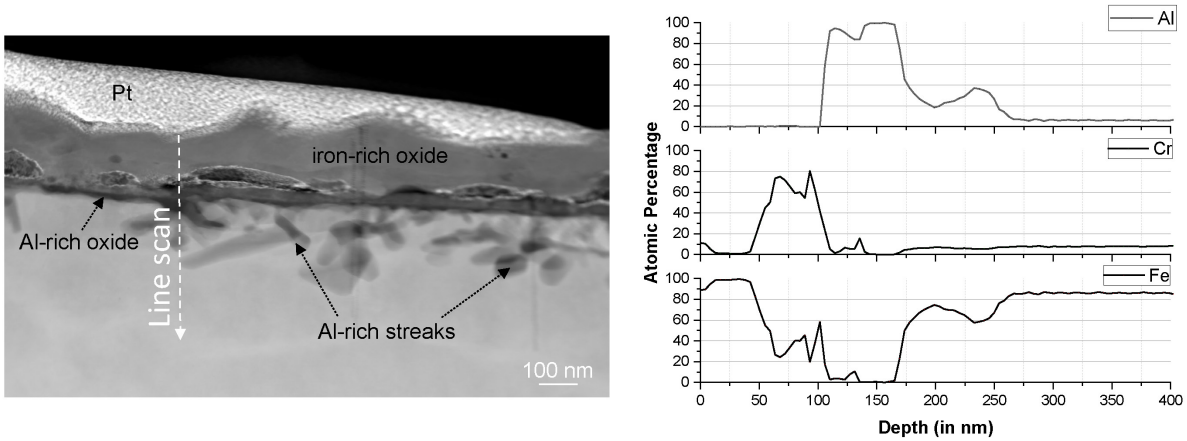

Figure 34: STEM-HAADF image (left) and EDX-data from line scan (right) of an iron-oxide-covered grain on FeCrAl0Si after exposure to 5% O_2 + N_2 (bal.) at 600 °C for 168 hours

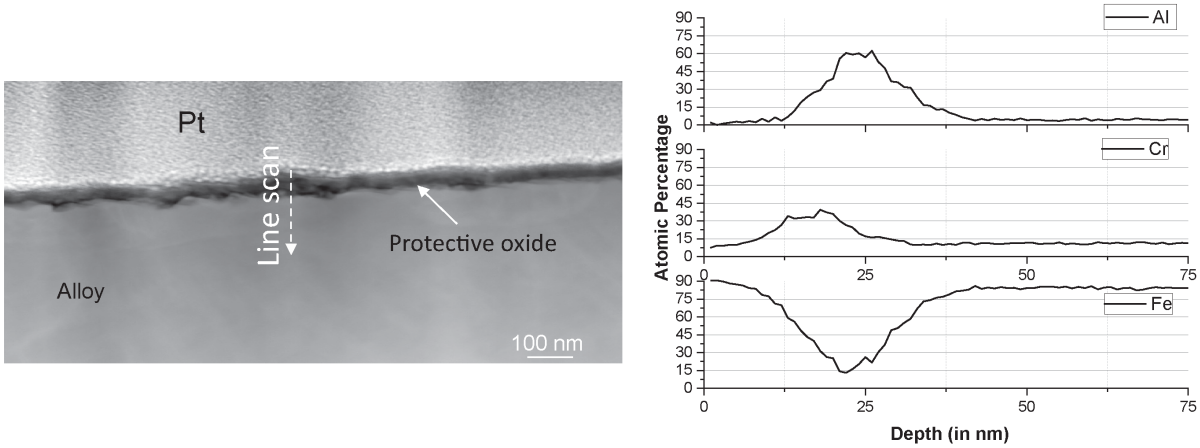

Figure 35: STEM-HAADF image (left) and EDX-data from line scan (right) of a protective grain on FeCrAl0Si after exposure to 5% O_2 + N_2 (bal.) at 600 °C for 168 hours.

The positive effect of minor additions of Si in stainless steel and other corrosion-resistant alloys on the high temperature corrosion resistance has been reported by several authors [19-22, 59, 61, 99, 100]. The majority of the studies have investigated this effect in the temperature range 700-1000 °C at which a thin SiO_2 scale has been found to form. This scale is suggested to act as a diffusion barrier, preventing further corrosion attack. However, the operating temperature of many applications is below this temperature range, which is why it is of interest to investigate whether the effect of Si addition is valid at lower temperatures. For this reason, the effect of minor additions of Si on the primary protection of lean FeCrAl alloys at 600 °C in dry O_2 was investigated (see Paper III and IV).

The mass gains attained from exposing the FeCrAl model alloys in Table 4 (0-2 wt% Si) to dry O_2 (5% O_2 + N_2 (bal.) at 600 °C, showed that increasing Si content had a somewhat mixed effect on the primary protection, see Figure 36. The recorded mass gain upon the addition of 1 wt% Si was slightly higher than for the alloy without Si. However, the mass gain was drastically decreased upon the addition of 2 wt% Si.

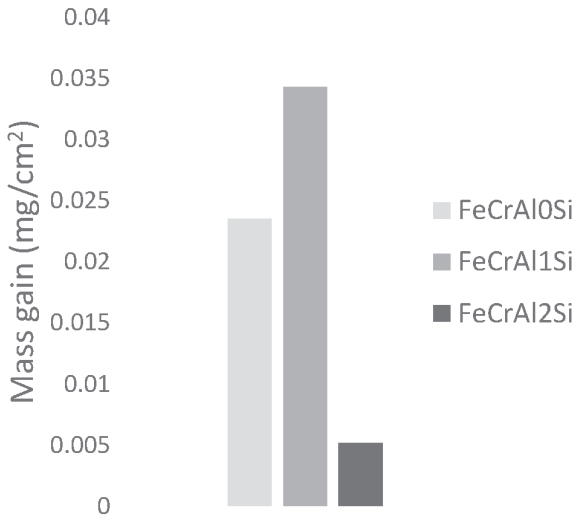

Figure 36: Average mass gain of FeCrAl model alloys with varying Si content (listed in Table 4) after exposure to 5% O_2 + N_2 (bal.) at 600 °C for 168 hours.

These thermogravimetrical changes can be correlated to the surface morphology, see Figure 37. The higher mass gain of FeCrAl0Si and FeCrAl1Si can be attributed to the formation of iron-oxide-covered (the former) grains and iron oxide nodules (both alloys). None of these features were found on the surface of FeCrAl2Si, but a thin protective oxide scale has formed on the entire surface.

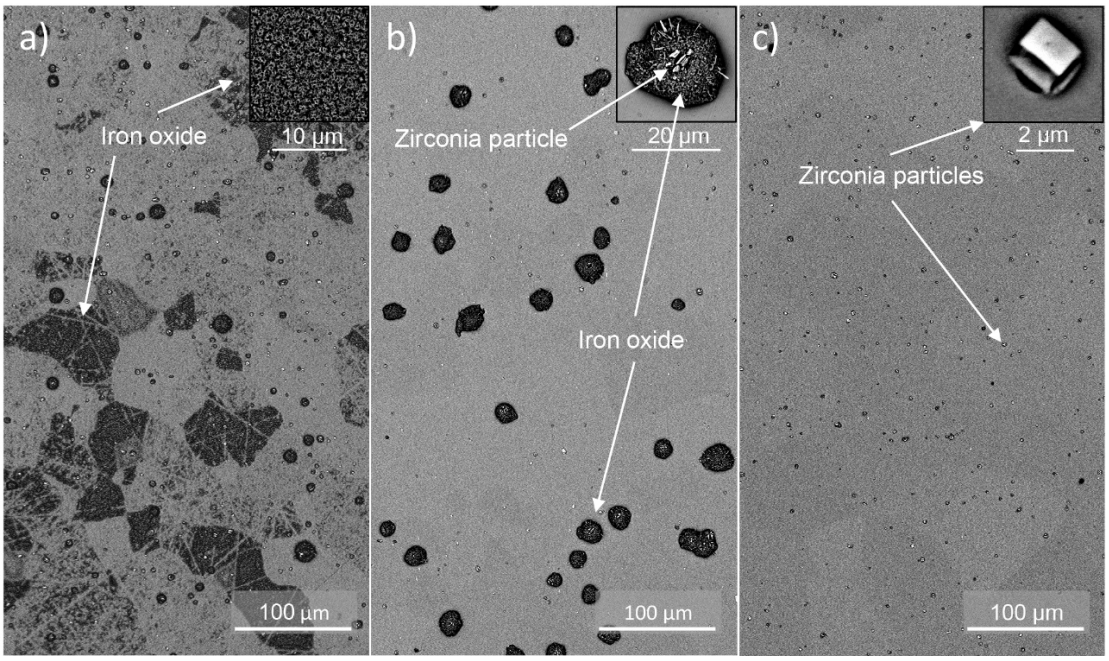

Figure 37: SEM-BSE plan view images of a) FeCrAl0Si, b) FeCrAl1Si and c) FeCrAl2Si after exposure in 5% O_2 + N_2 (bal.) for 168 hours at 600 °C.

To investigate if these surface features could act as nucleation sites for breakaway oxidation in more corrosive environments, the same alloys were exposed to wet O_2 (5% O_2 + 20% H_2O + N_2(bal.)) at 600 °C for 168 hours. This drastically changed the corrosion behavior of FeCrAl0Si, as can be seen in Figure 38. Comparing the mass gain of FeCrAl0Si after exposure to dry and wet O_2, it is apparent that breakaway oxidation occurred when exposed to wet O_2. However, both FeCrAl1Si and FeCrAl2Si displayed significantly lower mass gains after exposure to wet O_2 than under dry conditions.

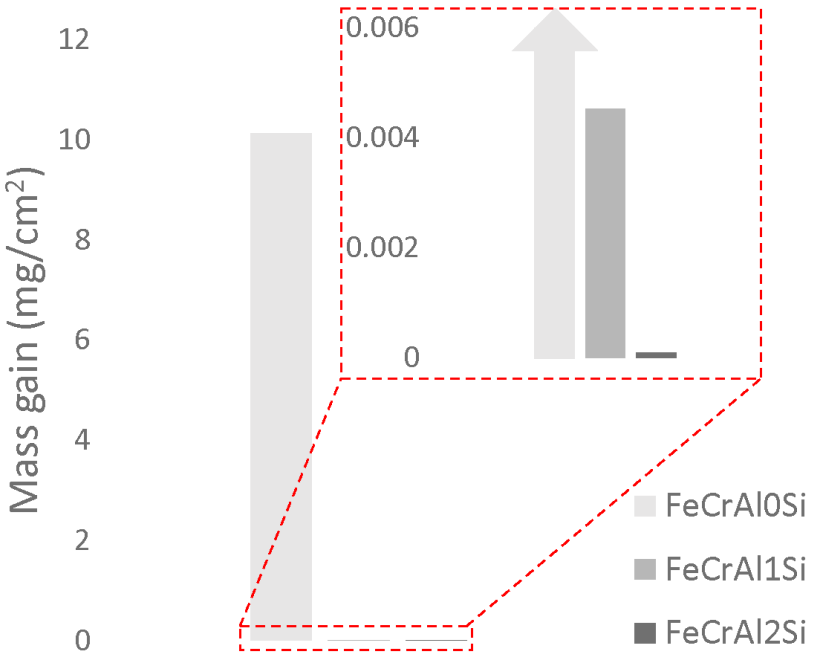

Figure 38: Average mass gain of FeCrAl model alloys with varying Si content (listed in Table 4) after exposure to 5% O_2 + 20% H_2O + N_2 (bal.) at 600 °C for 168 hours.

These changes can partially be explained by the surface morphology of the alloys after exposure to wet O_2, see Figure 39. Firstly, the rough surface morphology of FeCrAl0Si is indicative of a thick oxide (in the micrometer range), which was confirmed in the cross-section image in Figure 39d, which shows that a roughly 80 µm thick iron-rich multi-layered oxide. FeCrAl1Si displayed a significantly reduced number of iron oxide nodules after exposure to wet O_2, which explains the roughly ten orders of magnitude lower mass gain. FeCrAl2Si also displayed a significantly lower mass gain corresponding to an oxide thickness of 1 nm (based on the formation of Al_2O_3 and the assumptions described in section 6.3).

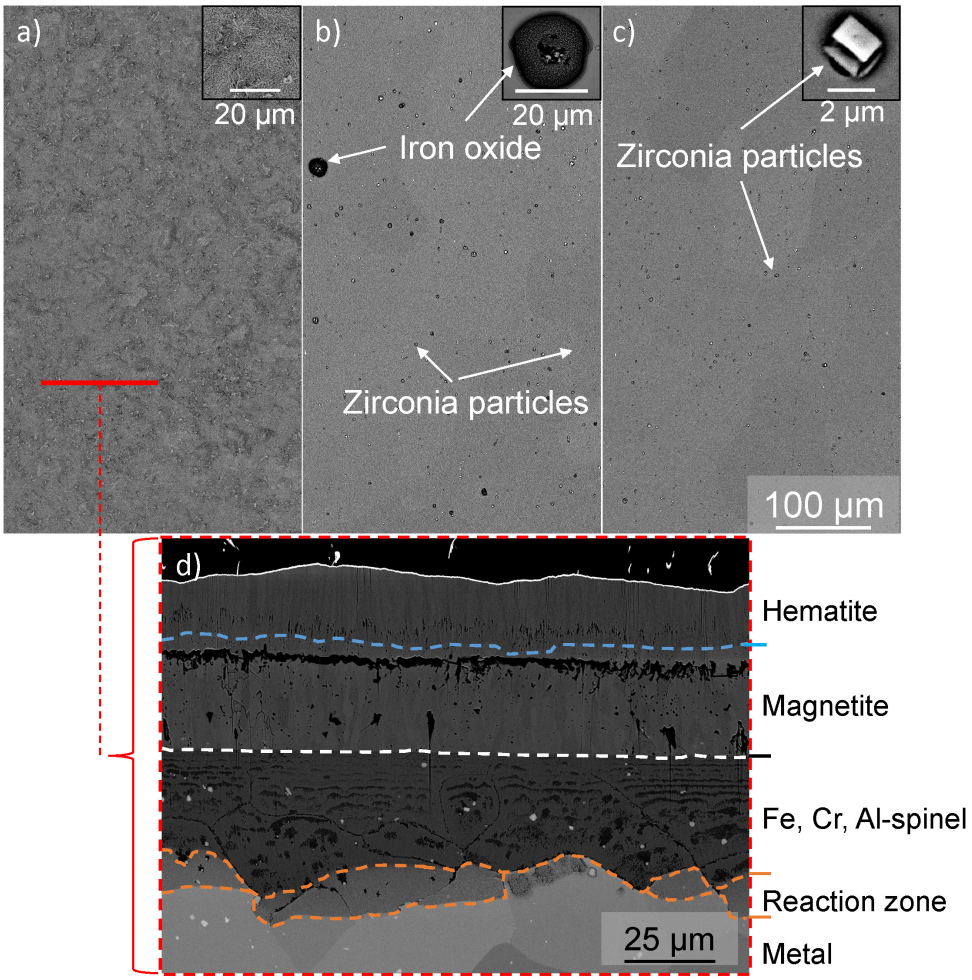

Figure 39: SEM-BSE plan view images of a) FeCrAl0Si, b) FeCrAl1Si and c) FeCrAl2Si and d) a cross-section image of FeCrAl0Si after exposure to 5% O_2 + N_2 (bal.) for 168 hours at 600 °C.

To investigate the reason behind a FeCrAl alloy's reduced sensitivity to water vapor upon the addition of Si, the microstructure of the oxide scale formed on FeCrAl2Si after exposure to dry O_2 was examined with STEM analysis, see Figure 40. The figure shows that FeCrAl2Si formed a 50 nm thick oxide scale that consists of a highly Cr-enriched outer layer on top of an inner Al-rich layer (significant iron content but a very low Cr content). Two important differences between FeCrAl0Si and FeCrAl2Si could be isolated. Firstly, the segregation of Cr to the outer part of the oxide scale formed on FeCrAl2Si could be connected to the reduced sensitivity to water vapor since the rest of the oxide scale remained relatively free of Cr in comparison to the oxide scale formed on FeCrAl0Si. Secondly, the overall Al content was found to be higher in the oxide scale formed on FeCrAl2Si (45-71 cat% Al) than in the oxide scale formed on FeCrAl0Si (23-34 cat% Al) when integrating the Al content from the STEM-EDX analysis. That the Al content in the oxide scales differs to such a high extent is surprising since both alloys had the same Al content.

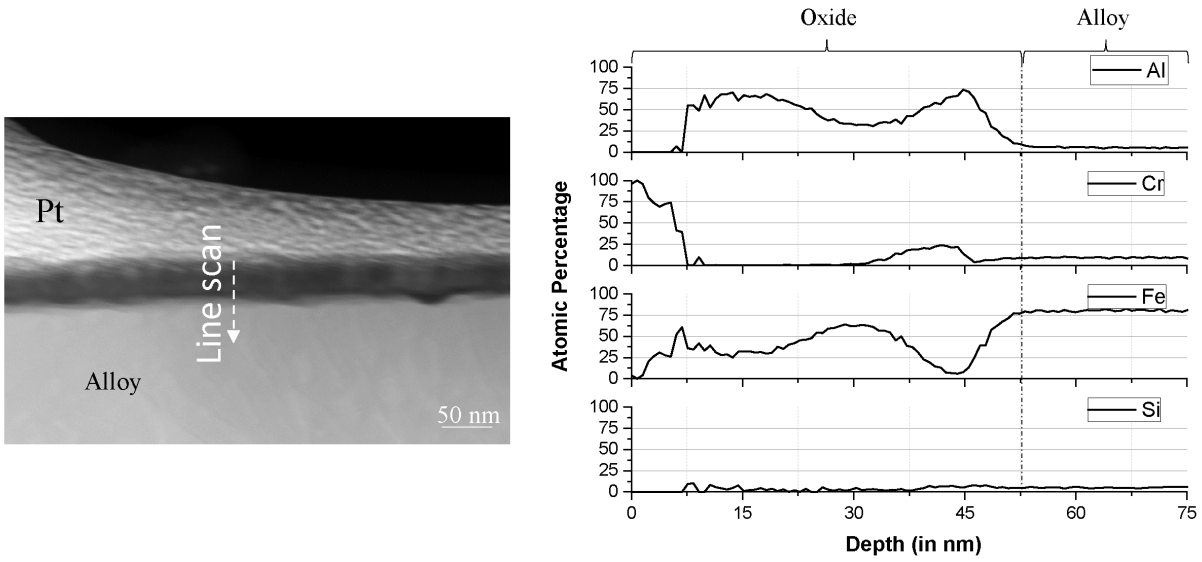

Figure 40: STEM-HAADF image (left) and EDX-data from line scan (right) of the oxide formed on FeCrAl2Si after exposure to 5% O_2 + N_2 (bal.) at 600 °C for 168 hours.

Thermodynamic calculations supported the observed segregation of Cr-rich an Al-rich oxide layers within the oxide scale formed on FeCrAl2Si, see Figure 41. The figure shows that segregation occurs upon the addition of Si, while an intermixed Cr/Al-rich oxide scale forms in the absence of Si. In addition, the range of pO_2 at which a pure alumina is stable is significantly extended, i.e. pure alumina could form at an earlier stage of the oxidation process. Pure alumina was not found anywhere in the oxide scales of either of the alloys. However, deviations from the calculated equilibrium compositions was expected because of the relatively low temperature and short exposures. The interaction between Si and Al/Cr in the alloy and the influence of Si on each activity is displayed in Figure 42. Each line in the figure corresponds to an activity of Al (left) or Cr (right). The figure illustrates that the activity of Al increases with the Si content in the alloy while the activity of Cr in the alloy decreases (the red arrows show the transition from one iso-activity line to the next when increasing the Si content). Thus, FeCrAl2Si is expected to behave like an alloy with a higher Al content, which generally results in the formation of more Al-rich oxide scales [101].

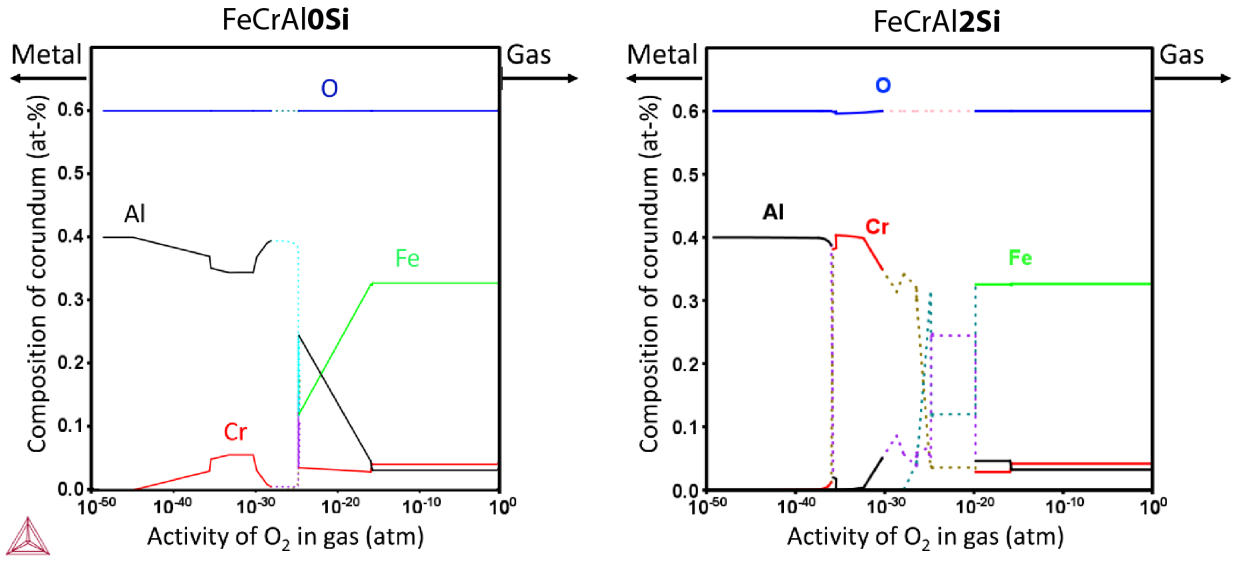

Figure 41: Predicted equilibrium compositions of the corundum-type oxide at different pO_2 for FeCrAl0Si (left) and FeCrAl2Si (right), attained with thermodynamic calculations using Thermo-Calc. The dotted lines show the compositions at values of pO_2 at which the corundum is metastable.

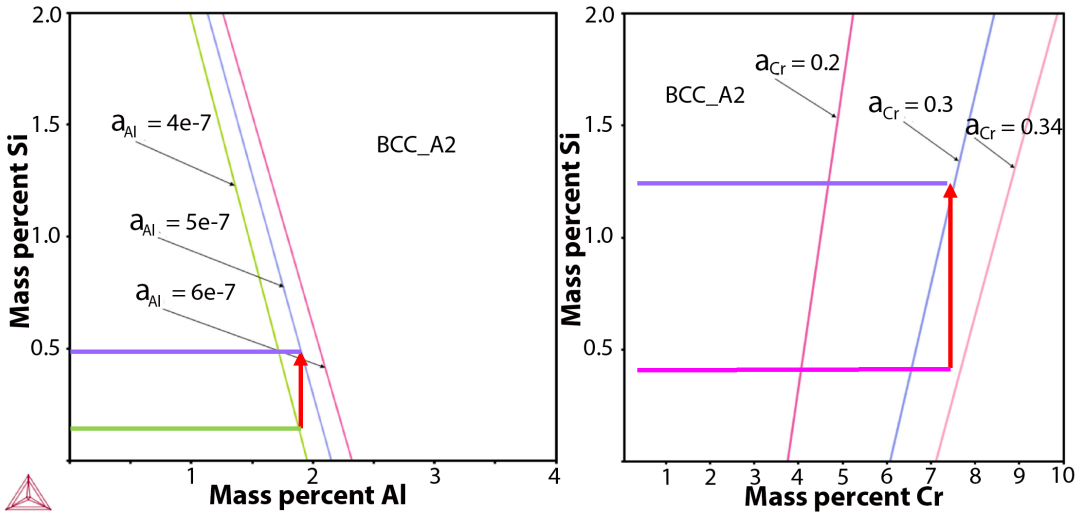

Figure 42: The influence of Si content on the activity of Al (left) and Cr (right) in the alloy, attained with thermodynamic calculations using Thermo-Calc.

The increased Al content in the oxide scale upon the addition of Si is a reasonable explanation to the increased corrosion resistance in the humid environment. However, after exposure to wet O_2, FeCrAl2Si was found to have formed a less Al-rich oxide scale than after exposure to dry O_2, see Figure 43. The EDX analysis showed that the overall Al content in the oxide scale was 24-30 cat%, i.e. similar to that of FeCrAl0Si after exposure to dry O_2. Instead, high enrichment of Si was found in the outer part of the scale. This is in contrast to the oxide scale formed after exposure to dry O_2, which showed an almost complete absence of Si. The interaction between Si and water vapor has previously been observed by Sand et al. when exposing a Si-containing FeCrAl alloy to both dry and wet air at 800 °C [102, 103]. Elevated Si content was found in the outer part of the oxide scale after exposure to wet air, while no Si was present in the oxide scale after exposure to dry air. Additionally, XRD analysis showed indications of the aluminum silicate, mullite. Because of the higher exposure temperatures, this may not be directly compared to the present study. In the present study, no mullite was detected with XRD analysis.

The outer part of the oxide scale formed on FeCrAl2Si after exposure to wet O_2 was also completely free of Cr. This is in contrast to the outer part of the oxide scale formed on FeCrAl2Si after exposure to dry O_2, which was found to be highly enriched in Cr (Figure 40). As described in section 4.5.1, chromia-forming alloys generally display initial mass loss during exposure to water vapor in oxidizing conditions because of the phenomenon known as Cr evaporation. This may explain the very low mass gain of FeCrAl2Si after exposure to wet O_2. To investigate potential Cr evaporation, FeCrAl2Si was exposed to 20% H_2O + air at 600 °C for 168 hours using the set-up described by Sand et al. [104] in which the amount of evaporated Cr can be measured. It was found that 0.001 mg/cm^2 Cr had evaporated after 168 hours. The measured Cr evaporation (0.001 mg/cm^2) corresponds to a 6 nm thick chromia scale which is in the same range as the with Cr-rich outer layer found on FeCrAl2Si after exposure to dry O_2. This suggests that the low mass gain in wet O_2 is a result of evaporation of the outer Cr-rich layer.

The detailed microstructural analysis suggests that the mechanism behind the very low Cr content found in the oxide scale of FeCrAl2Si after exposure to wet O_2, could be connected to enrichment of Si in the outer part of the scale or the segregation of Cr- and Al-rich layers. However, regardless of the underlying mechanism(s), the very low Cr content could explain the high corrosion resistance to the humid environment upon the addition of Si.

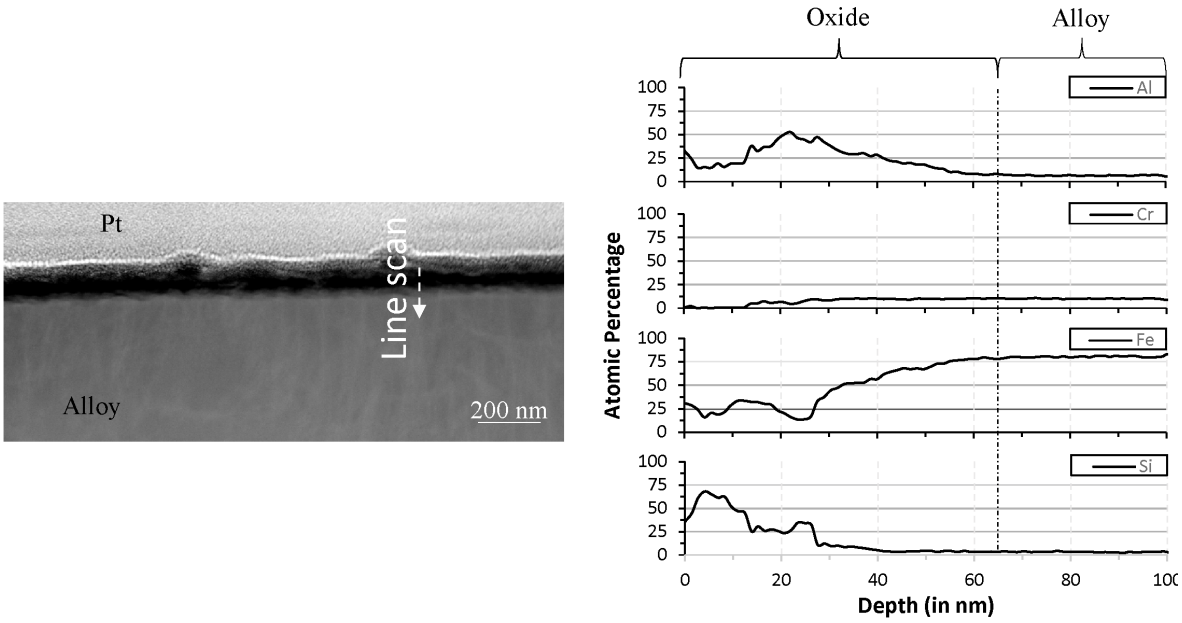

Figure 43: STEM-HAADF image (left) and EDX-data from line scan (right) of the oxide formed on FeCrAl2Si after exposure to 5% O_2 + 20% H_2O + N_2 (bal.) at 600 °C for 168 hours.

The addition of Si was also found to extend the range of Cr content at which a FeCrAl alloy can form a primary protection. As was shown in the beginning of this section, Fe5Cr3Al had difficulties with forming a fully protective oxide scale when exposed in dry O_2, exhibiting a higher mass gain the more highly alloyed steels, see Figure 32. However, all Si-containing FeCrAl model alloys (listed in Table 5), with Cr contents from 5 to 20 wt% remained protective when exposed to wet O_2, see Figure 44. In other words, the addition of Si enabled an alloy that is generally not considered chromia/alumina-forming, to form a protective oxide scale (primary protection) that was also able to withstand breakaway oxidation in the presence of water vapor. The slightly higher mass gain that Fe5CrAlSi showed in relation to the other alloys can be explained by minor presence of iron oxide nodules on the alloy surface, see Figure 45. Nevertheless, the visibility of the underlying alloy grains showed that the base oxide was in the nanometer range.

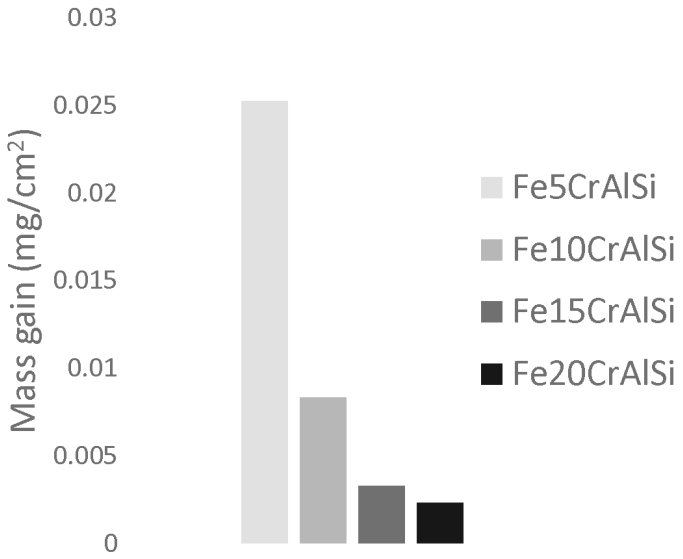

Figure 44: Average mass gain of Si-containing FeCrAl model alloys with varying Cr content (listed in Table 5) after exposure to 5% O_2 + 20% H_2O + N_2 (bal.) at 600 °C for 168 hours

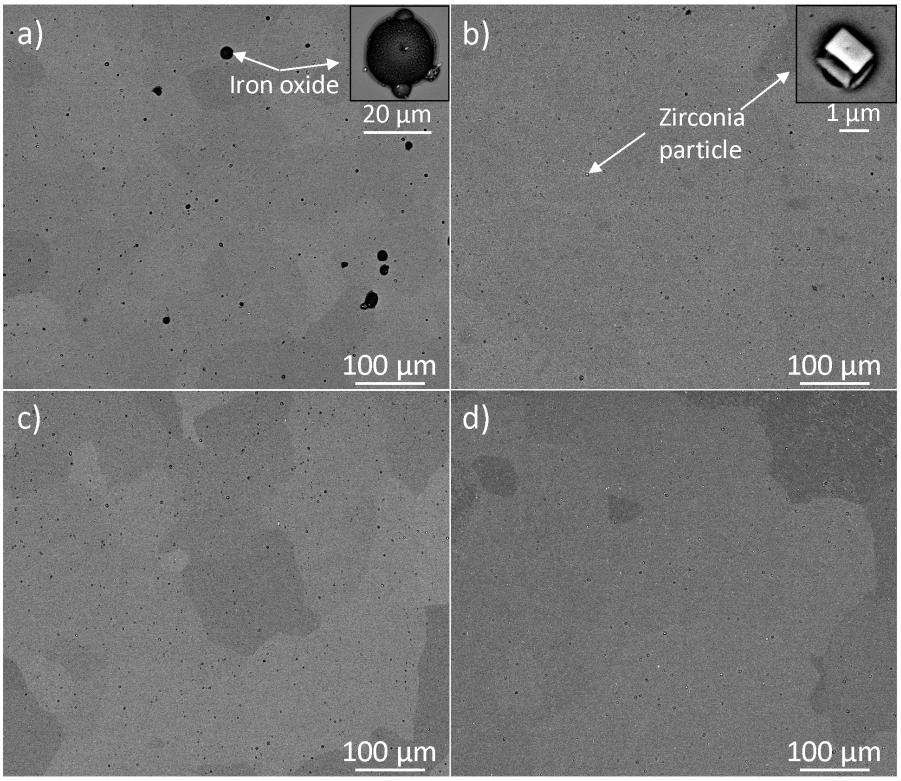

Figure 45: SEM-BSE plan view images of a) Fe5CrAlSi, b) Fe10CrAlSi, c) Fe15CrAlSi and d) Fe20CrAlSi after exposure to 5% O_2 + 20% H_2O + N_2 (bal.) at 600 °C for 168 hours.

This section has demonstrated the potential to improve the primary protection of FeCr(Al) alloys by optimizing the concentration of different alloying elements. Enabling lean FeCrAl alloys to retain their primary protection in the presence of water vapor with minor additions of Si shows great promise for reducing the detrimental effects of Cr and Al on mechanical properties as well as costs without sacrificing the corrosion resistance of the alloys. The proposed mechanisms should be further investigated as these could be beneficial for the future development of alloys for humid environments.

8.1.2 The secondary protection

The secondary corrosion regime is generally referred to as the oxidation propagation after breakaway oxidation. As mentioned in Chapter 5, breakaway oxidation is often considered the end of the lifetime of a component, which can be true for applications in which the formation of thick oxides is detrimental to certain key parameters. However, breakaway oxidation is generally inevitable in extremely harsh environments. A vital question associated with this is whether it is possible to influence the propagation behavior within the secondary regime and thereby reduce the material degradation of alloys. Iron-based alloys generally form multi-layered iron-rich oxide scales after transitioning into the secondary regime [53, 54, 98, 105-109]. Thus, the same concept of improving the primary protection, i.e. by the addition of Cr, Al and Si, may not necessarily be valid for the secondary protection.

A broad range of model alloys (FeCr(Al, Si)) were exposed in environments that were chosen according to their ability to rapidly break down the primary protection (e.g. water vapor, KCl and K_2CO_3). The observations are further discussed in Papers I, II, III and V and the most important outcomes will be presented and discussed in this section.

K_2CO_3 has been shown to break down the primary protection by depleting the initially formed oxide scale in Cr [9]. After transitioning into the secondary corrosion regime, K_2CO_3 is assumed to have no or very limited influence on the oxidation kinetics. The FeCr(Al) model alloys in Table 1, Table 2 and Table 3, were exposed to dry O_2 (5% O_2 + N_2 (bal.)) in the presence of K_2CO_3 in a thermobalance to investigate how Cr and Al influence the initiation kinetics (first 48 hours) within the secondary regime.

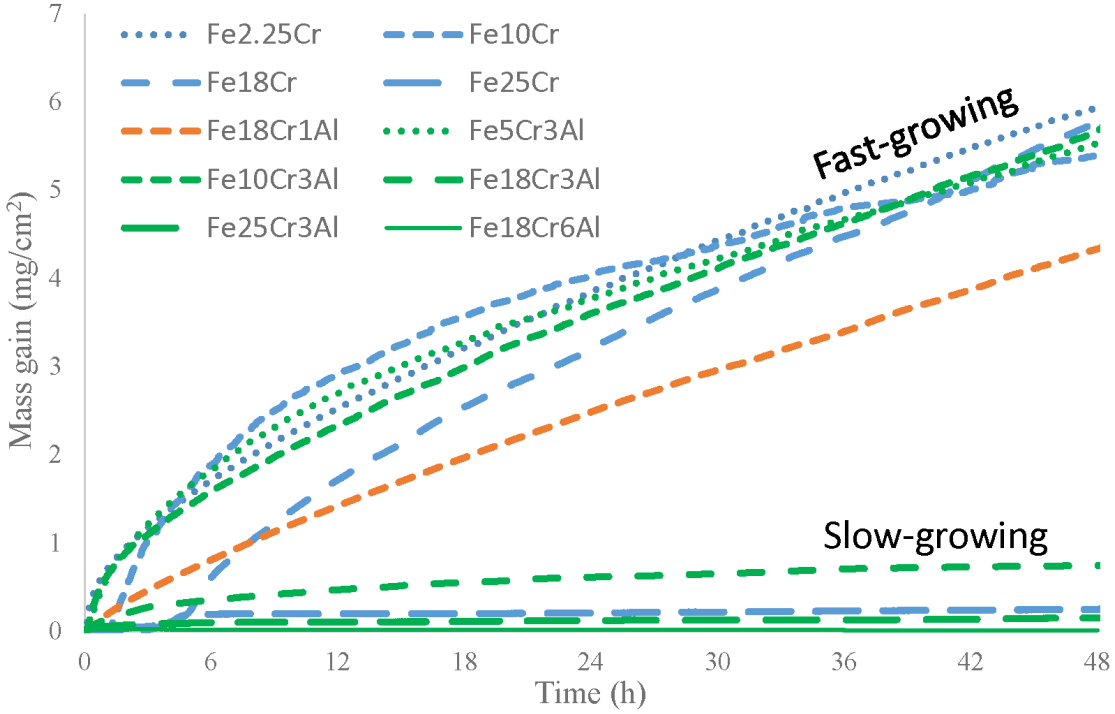

Figure 46: TGA data for the FeCr(Al) model alloys after exposure to 5% O_2 + N_2 (bal.) in the presence of K_2CO_3 at 600 °C for 48 hours.

The K_2CO_3 deposit on the sample surfaces was able to successfully break the primary protection of all the FeCr(Al) model alloys, except Fe18Cr6Al, Figure 46. Fe18Cr6Al seemingly was able to rapidly form an oxide scale with a sufficient Al content to resist the breakdown in the presence of K_2CO_3. Most of the other alloys immediately transitioned into the secondary corrosion regime (indicated by higher mass gain than Fe18Cr6Al). It is apparent that the range of model alloys displayed two different behaviors within the secondary regime: fast-growing and slow-growing oxide scale growth. The FeCr model alloys (Cr < 25wt%) and the FeCrAl model alloys (Cr < 18wt%) displayed close to identical behavior, i.e. the formation of fast-growing oxide scales exhibiting initial exponential growth followed by parabolic growth. Even though the alloying composition varied significantly between these alloys, the composition did not seem to influence the corrosion behavior within the secondary regime, but all alloys displayed similar corrosion rate as iron and low-alloyed steels [98, 110]. The corrosion rate was drastically reduced when a critical Cr content was exceeded (Cr ≥ 25wt% for FeCr alloys and Cr ≥ 18wt% for FeCrAl alloys). All alloys that fulfilled these criteria (Fe18Cr3Al, Fe25Cr3Al and Fe25Cr) transitioned into a sub-parabolic behavior at an early stage of the oxidation process. The transition from fast to slow oxide scale growth (in the secondary regime) occurred at a lower Cr content for the FeCrAl alloys than the FeCr alloys, indicating a synergistic relationship between Cr and Al.

The measured oxide scale thickness of the alloys was in agreement with the calculated values (40-50 µm for alloys forming fast-growing oxides and 1-5 µm for alloys forming slow-growing oxides), see Figure 47. Regardless of material class and corrosion rate in the secondary regime, the alloys had formed iron-rich oxide scales with similar microstructure, i.e. outward-growing iron oxide and inward

growing (Fe, Cr, (Al))-oxide with similar thickness ratios (60-70% outward and 30-40% inward). The most apparent differences between the alloys that displayed a poor secondary protection and the alloys that displayed a good secondary protection is the total oxide scale thickness and the formation of a reaction zone, i.e. internal oxidation of the equilibrium composition in the spinel phase and iron (found underneath the oxide scale of alloys that displayed a poor secondary protection). A nitridation zone was found underneath the slow-growing oxide scales of FeCrAl alloys (Fe18Cr3Al and Fe25Cr3Al). The alloys that had formed a reaction zone displayed a peculiar microstructure in the inward-growing scale, consisting of porous and dense layers that alternated in a periodic manner. The FeCrAl alloys that formed slow-growing oxide scales displayed nitridation zones underneath the oxide scales. This has previously been found on FeCrAl alloys after breakaway oxidation at 600 °C, shown to consist of Al-nitrides [111]. SEM-EDX analysis indicated that the inward-growing (Fe, Cr, Al)-oxide scale on the FeCrAl alloys that displayed a good secondary protection was highly enriched in Cr and depleted in Fe.

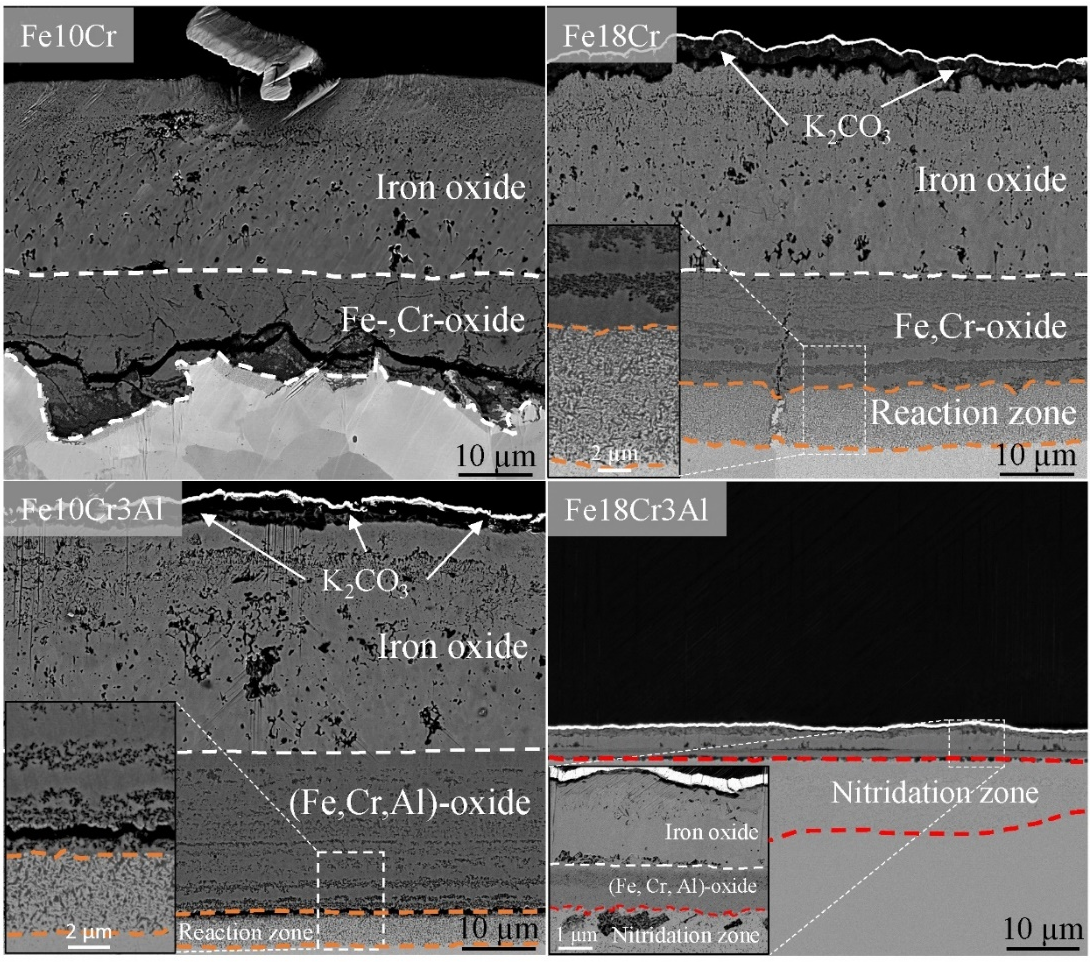

Figure 47: SEM-BSE cross section images of Fe10Cr, Fe18Cr, Fe10Cr3Al and Fe18Cr3Al after exposure to 5% O_2 + N_2 (bal.) in the presence of K_2CO_3 at 600 °C for 48 hours.

Minor additions of Si were shown to significantly improve the primary protection of FeCrAl alloys (section 8.1.1), but could these additions also improve the secondary protection? To answer this question, the FeCrAl model alloys in Table 4 were exposed to wet O_2 in the presence of KCl (to break down the primary protection) in both a thermobalance and a tube furnace as described in section 6.1.2. Because of the relatively high evaporation rate of KCl at 600 °C, the mass change of KCl-sprayed gold foils was recorded both in the thermobalance and the tube furnace. The evaporation rate was found to be 0.008 mg/cm^2 h in the thermobalance and 0.03 mg/cm^2 h in the tube furnace. The higher

evaporation rate for KCl in the tube furnace was attributed the higher flow rate. The evaporation rate in each system was used to estimate the actual mass gain as a result of oxide scale formation.

Previous research on the influence of Si on corrosion resistance in harsh environments are scarce. However, the few studies investigating this found that the addition of Si significantly reduced the corrosion rate of FeCr(Al) alloys [112-114]. Accordingly, the initial oxidation rate (first 48 hours) was significantly reduced upon the addition of Si, see Figure 48. FeCrAl0Si displayed oxidation kinetics similar to that of the FeCr(Al) model alloys with poor secondary protection, i.e. the formation of a fast-growing oxide scale (compare with Figure 46). FeCrAl1Si and FeCrAl2Si exhibit similar final mass gains but behaves slightly different during the first 24 hours. FeCrAl1Si initially displayed a more rapid initial oxidation rate but transitioned into a sub-parabolic behavior after about 6 hours, while FeCrAl2Si initially displayed a lower rate but did not transition into a sub-parabolic behavior until after about 24 hours. All Si-containing alloys displayed a slightly higher mass gain (1-2 mg/cm) than the FeCr(Al) model alloys with a good secondary protection (compare with Figure 46), which could be connected to the presence of Cl (Cl-induced corrosion described in section 4.5.3.).

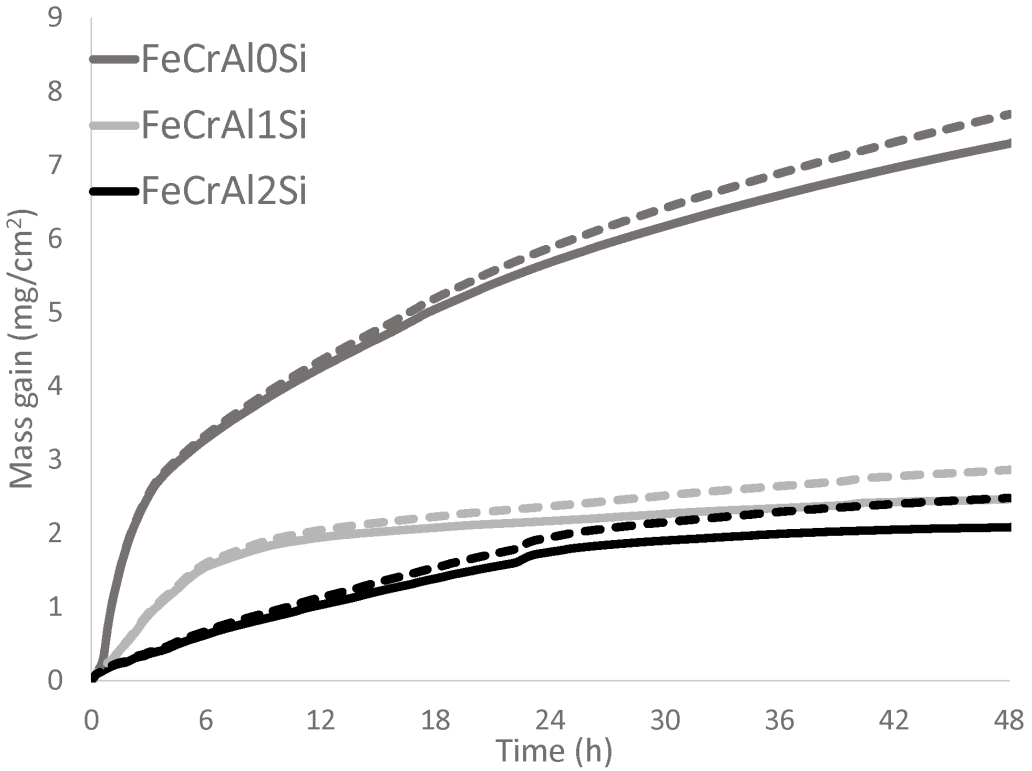

Figure 48: TGA data for the FeCrAl(Si) model alloys (Table 4) after exposure to 5% O_2 + 20% H_2O + N_2 (bal.) in the presence of KCl at 600 °C for 48 hours in a thermobalance. The dashed lines correspond to the adjusted mass gain considering the evaporation of KCl under the studied conditions.

The recorded mass gain of FeCrAl0Si and FeCrAl1Si after 168 hours of exposure agreed relatively well with the oxidation kinetics displayed by the TGA data, see Figure 49. However, FeCrAl2Si displayed about twice as high mass gain after 48 hours than after 168 hours. In addition, the mass gain of FeCrAl2Si was twice as high as FeCrAl1Si even though exhibited similar oxidation kinetics after 48 hours of exposure. This indicates that FeCrAl2Si may transition into sub-parabolic behavior at an earlier stage than FeCrAl1Si when exposed in the tube furnace. The shorter exposure to high presence of KCl in the tube furnace set-up, in which the evaporation rate of KCl is significantly higher than in the thermobalance, may be the explanation. The higher presence of KCl might inhibit the mechanism behind the transition into sub-parabolic behavior for FeCrAl2Si. That the transition into sub-parabolic

behavior for FeCrAl1Si does not seem to be affected by the higher presence of KCl indicates that this effect becomes less pronounced when the oxide scale thickness increases.

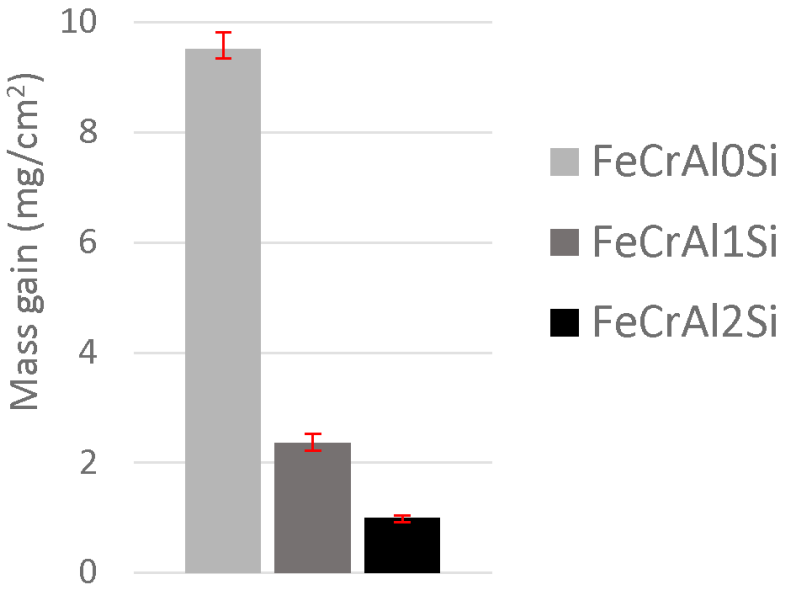

Figure 49: Recorded mass gain for the FeCrAl(Si) model alloys (Table 4) after exposure to 5% O_2 + 20% H_2O + N_2 (bal.) in the presence of KCl at 600 °C for 168 hours in a tube furnace.

The oxide scales formed on FeCrAl0Si (65-80 µm), FeCrAl1Si (25-35 µm) and FeCrAl2Si (10-20 µm) after exposure for 168 hours displayed a microstructure similar to those observed for all the ferritic steels (in this work) within the secondary regime, i.e. outward-growing iron oxide and inward-growing (Fe, Cr, Al, (Si))-oxide, see Figure 50 and Figure 51. However, a reaction zone formed underneath the oxide scale of FeCrAl0Si, while nitridation zones were found underneath the oxide scales of the other alloys. The hematite and magnetite layers were easily distinguished in the outward-growing oxide scale of FeCrAl0Si and FeCrAl1Si and displayed similar grain size (40-400 nm in hematite and 1-2 µm in magnetite). The hematite and magnetite layers were not as distinct for FeCrAl2Si, which displayed a grain size of 70-700 nm in the outward-growing oxide scale. Hematite is the most slow-growing of the iron oxides due to the lower lattice defect density [12, 40, 115]. Initially forming a thicker hematite layer may therefore reduce the overall corrosion rate during propagation. However, the thickness of the hematite layer was in the same range for all alloys and can therefore not explain the drastically reduced oxidation rate. It is generally known that fine-grained oxides grow faster than course-grained oxides due to the increased number of grain boundaries, i.e. higher density of fast diffusion paths for ion transport. However, the reduced oxidation rate cannot be explained by a more course-grained outward-growing oxide scale since FeCrAl0Si and FeCrAl1Si displayed similar grain sizes in the outward-growing scale.

An interesting feature, which is only observed for the Si-containing alloys, is the part of the inward-growing oxide layer closest to the metal/oxide interface, shown in Figure 51a[3]. This 0.5-1.5 µm thick layer is seemingly denser than the rest of the inward-growing oxide and SEM-EDX analysis indicated that it is highly enriched in Cr (up to 60 cat%) and depleted in Fe. This is in contrast to the rest of the inward-growing oxide scale, which consists of about 25 cat% Cr and 60 cat% Fe. The amount of Al (15 cat%) and Si (10 cat%) remained relatively constant throughout the inward-growing oxide scale.

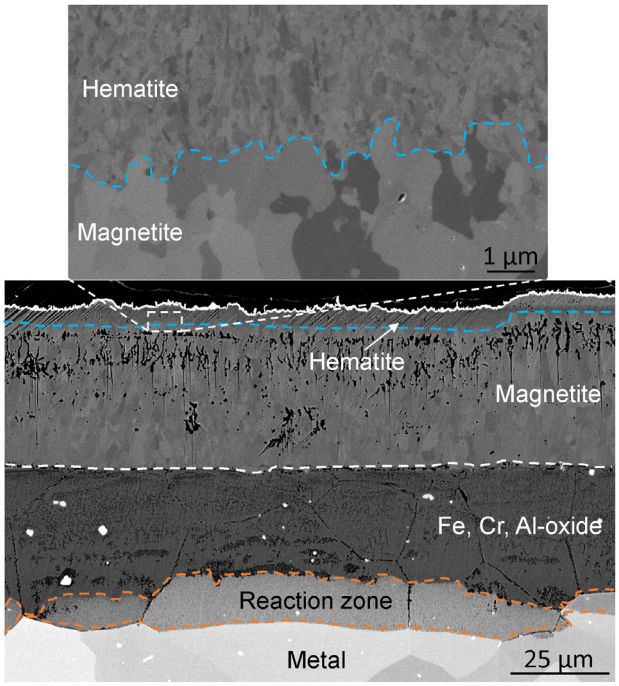

Figure 50: SEM-BSE cross section image of FeCrAl0Si after exposure to 5% O_2 + 20% H_2O + N_2 (bal.) in the presence of KCl at 600 °C for 168 hours in a tube furnace.

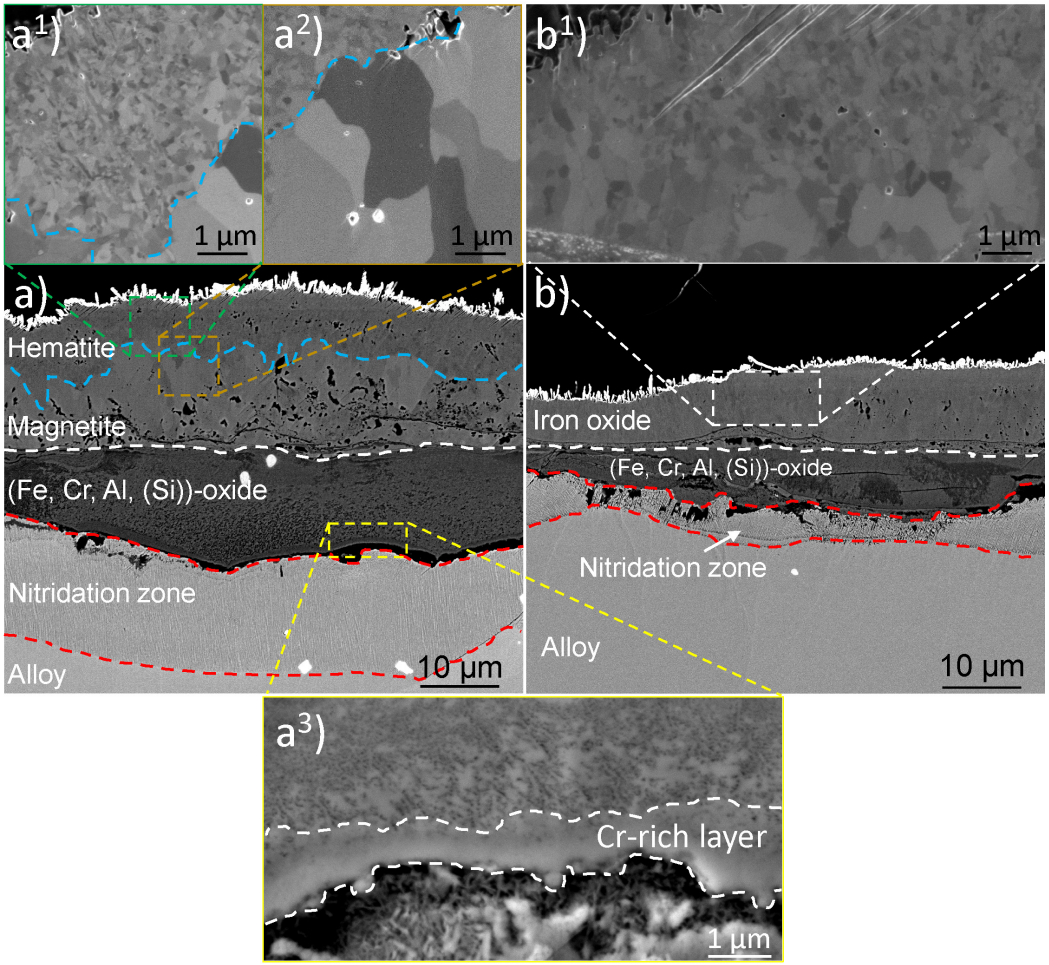

Figure 51: SEM cross section images of a) FeCrAl1Si and b) FeCrAl2Si after exposure to 5% O_2 + 20% H_2O + N_2 (bal.) in the presence of KCl at 600 °C for 168 hours in a tube furnace.

Investigating the corrosion behavior of the FeCr(Al) model alloys showed that both Cr and Al significantly improved the corrosion resistance within the secondary corrosion regime (Figure 46). Additionally, minor addition of Si resulted similar improvement for FeCrAl model alloys with lower Cr content (Figure 48) in an even more corrosive environment (water vapor and KCl). It was therefore of interest to investigate the combined effect, i.e. the effect of Cr content on the corrosion behavior of Si-containing FeCrAl alloys within the secondary regime. The FeCrAlSi model alloys in Table 5 were exposed both in a thermobalance (48 hours) and a tube furnace (168 hours) in dry O_2 in the presence of KCl. The results are further discussed in Paper V.

All alloys immediately transitioned into the secondary corrosion regime, Figure 52. Two very different oxidation kinetics can be distinguished. Fe5CrAlSi and Fe10CrAlSi formed much faster-growing oxide scales than Fe15CrAlSi and Fe20CrAlSi but displayed significantly lower oxidation rates than the FeCr(Al) model alloys with poor secondary protection (compare Figure 46 and Figure 52). Similar to FeCrAl1Si and FeCrAl2Si, Fe5CrAlSi and Fe10CrAlSi displayed different initial oxidation rates but the same final mass gain after 48 hours of exposure. All alloys transitioned into sub-parabolic behavior, but this occurred at a significantly earlier stage for Fe15CrAlSi and Fe20CrAlSi.

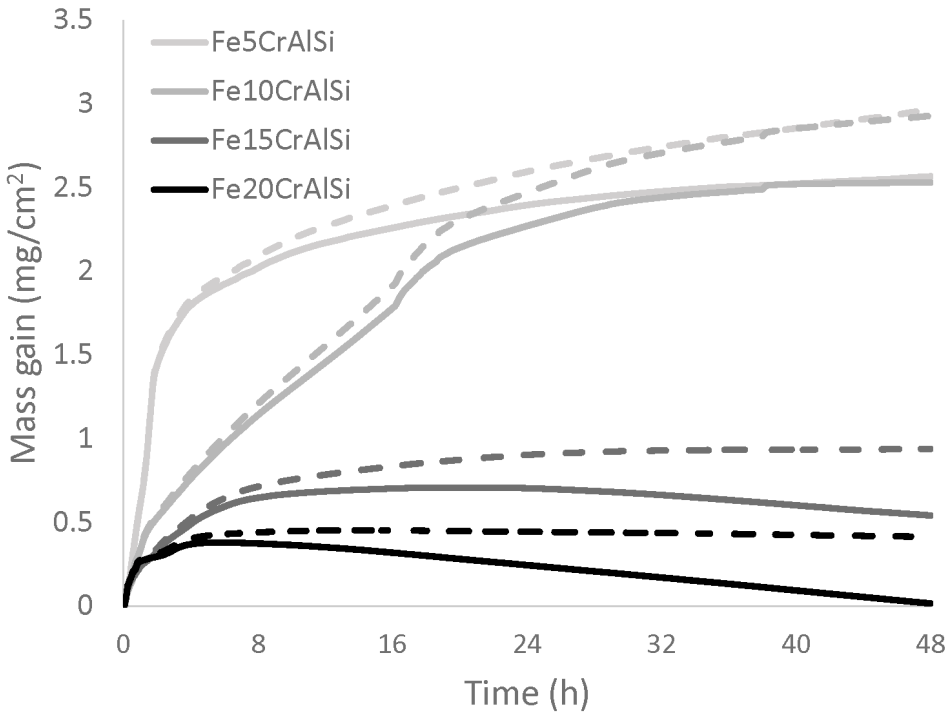

Figure 52: TGA data for the FeCrAlSi model alloys (Table 5) after exposure to 5% O_2 + 20% H_2O + N_2 (bal.) in the presence of KCl at 600 °C for 48 hours in a thermobalance. The dashed lines correspond to the adjusted mass gain considering the evaporation of KCl under the present conditions.

All alloys, except Fe5CrAlSi, displayed a lower mass gain after 168 hours than after 48 hours of exposure. As mentioned above, the initial oxidation kinetics of Fe5CrAlSi and Fe10CrAlSi differs similarly to those of FeCrAl1Si and FeCrAl2Si and so does the deviations between oxidation rates observed in the thermobalance and the tube furnace. Thus, as previously discussed, the higher presence of KCl may inhibit the transition into sub-parabolic behavior for a longer time in the thermobalance. Considering the evaporation of KCl, Fe15CrAlSi and Fe20CrAlSi displayed mass gains in the same range after 48 hours and 168 hours of exposure, which is in agreement with the early transition into sub-parabolic growth displayed by the TGA data (Figure 52) Thus, possibly due to the

elevated Cr content, the higher presence of KCl in the thermobalance does not seem to significantly inhibit the transition into sub-parabolic behavior for these alloys.

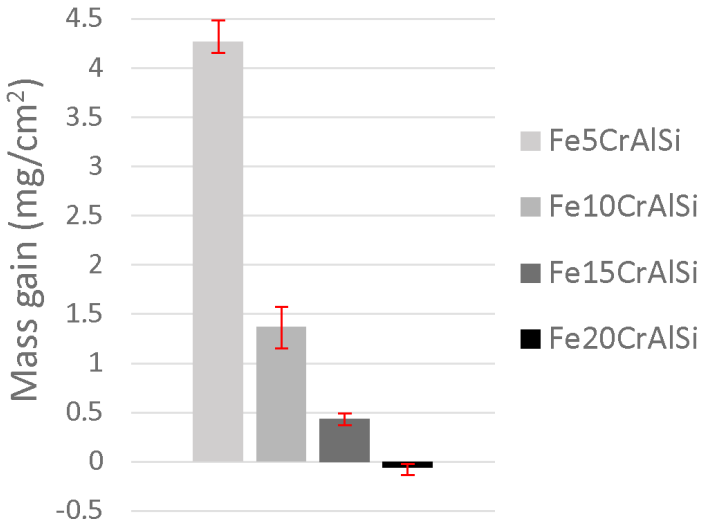

Figure 53: Recorded mass gain for the FeCrAlSi model alloys (Table 5) after exposure to 5% O_2 + 20% H_2O + N_2 (bal.) in the presence of KCl at 600 °C for 168 hours in a tube furnace.

All alloys formed iron-rich oxide scales with microstructures similar to those observed for alloys after breakaway oxidation but displayed greatly reduced scale thickness with increased Cr content, see Figure 54, Figure 55, Figure 56 and Figure 57. Fe5CrAlSi was the only alloy to form a reaction zone underneath the oxide scale (the other alloys formed a nitridation zone (NZ)). The oxide scale thickness varied largely over the surface of Fe10CrAlSi after exposure for 48 hours and explains the relatively high oxidation rate in the thermobalance, see Figure 55a-b. The inward-growing scales of Fe5CrAlSi, Fe10CrAlSi and Fe15CrAlSi (the outer part) was identified as spinel with EBSD analysis. Cr-enrichment was detected with SEM-EDX close to the metal/oxide interface of Fe10CrAlSi after both 48 and 168 hours of exposure but was more pronounced after the longer exposure. Similar Cr-enrichment, but more pronounced, was detected for Fe15CrAlSi and Fe20CrAlSi after 48 and 168 hours of exposure. However, the entire inward-growing scale of Fe20CrAlSi was enriched in Cr. In contrast to the generally increased corrosion resistance, Fe15CrAlSi and Fe20CrAlSi displayed grain boundary attack in areas under which large amounts of K_2CrO_4 had formed.

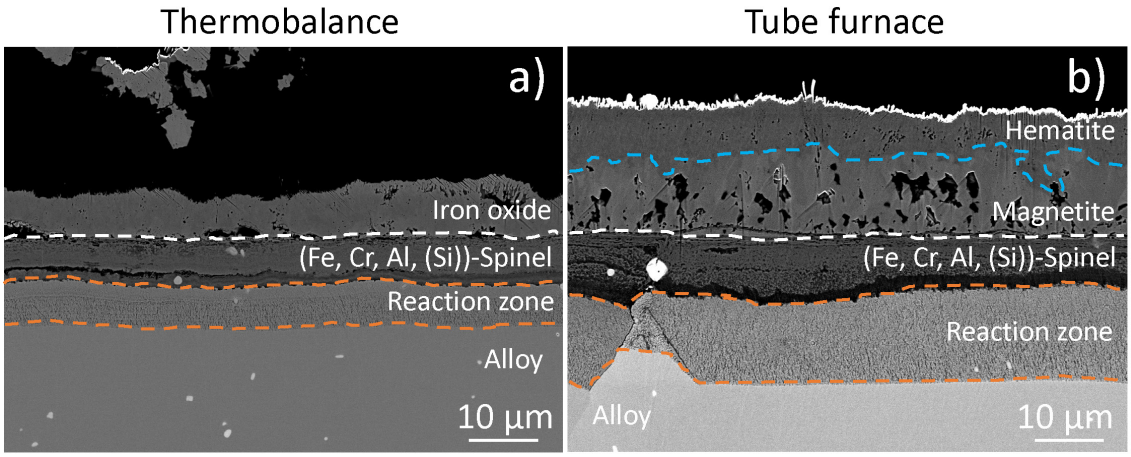

Figure 54: SEM cross section images of Fe5CrAlSi after exposure to 5% O_2 + 20% H_2O + N_2 (bal.) in the presence of KCl at 600 °C in a) a thermobalance for 48 hours and b) a tube furnace for 168 hours.

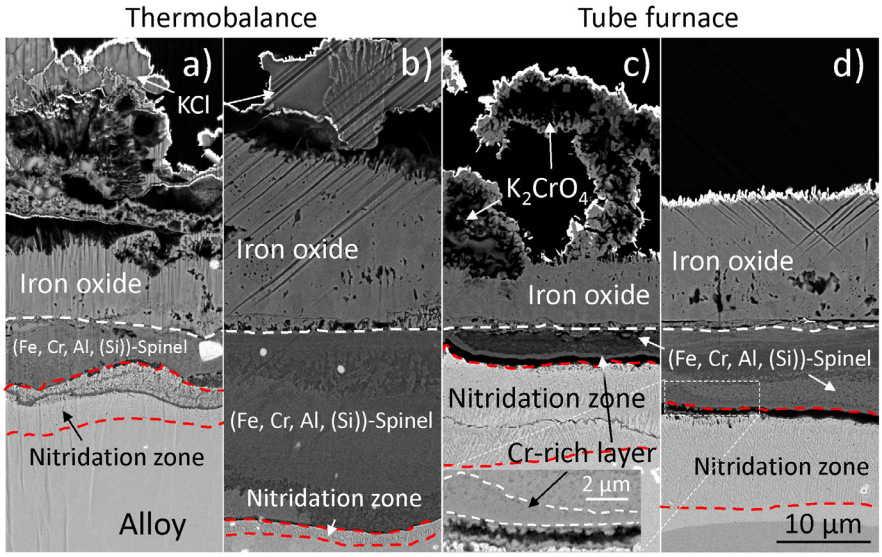

Figure 55: SEM cross section images of Fe10CrAlSi after exposure to 5% O_2 + 20% H_2O + N_2 (bal.) in the presence of KCl at 600 °C in a) a thermobalance for 48 hours and b) a tube furnace for 168 hours.

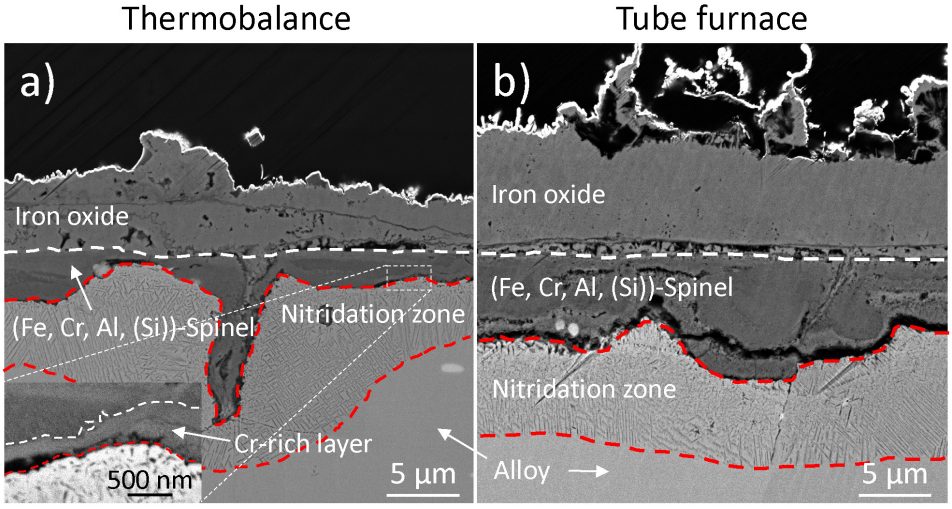

Figure 56: SEM cross section images of Fe15CrAlSi after exposure to 5% O_2 + 20% H_2O + N_2 (bal.) in the presence of KCl at 600 °C in a) a thermobalance for 48 hours and b) a tube furnace for 168 hours.

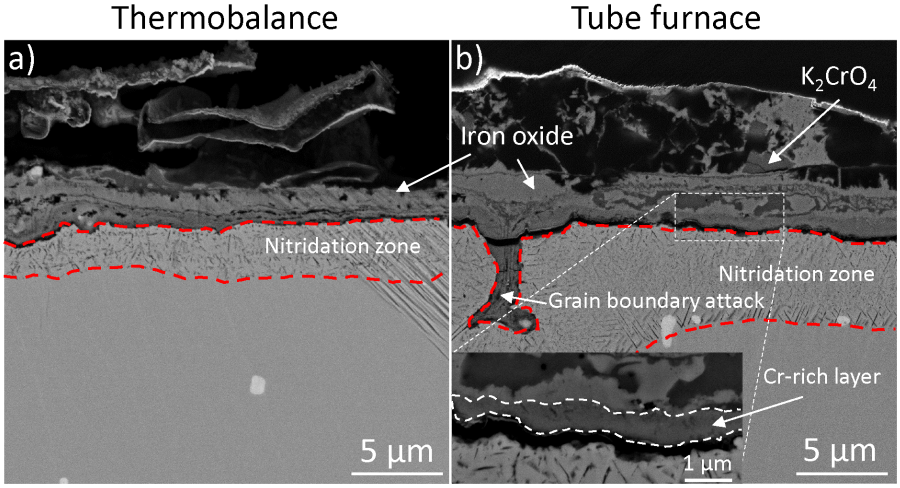

Figure 57: SEM cross section images of Fe20CrAlSi after exposure to 5% O_2 + 20% H_2O + N_2 (bal.) in the presence of KCl at 600 °C in a) a thermobalance for 48 hours and b) a tube furnace for 168 hours.

The cross-section overviews of Fe15CrAlSi and Fe20CrAlSi in Figure 58 shows that grain boundary attack occurred to a higher extent for the latter. Grain boundary attack was not observed for the FeCr(Al) model alloys when exposed in the presence of K_2CO_3 (see Figure 47) which strongly indicates that Cl is involved in the underlying mechanism. This is in agreement with previous research, showing higher extent of grain boundary attack during exposure in the presence of higher amounts of KCl [116, 117]. In addition, traces of Cl were observed along the attacked grain boundaries. Malede et al. showed correlations between grain boundary attack and the presence of Cr-rich σ-phase in the grain boundaries [118, 119]. The formation of the σ-phase has been shown to form in the temperature range 600-1000 °C [120-123] but is very slow at 600 °C. Accordingly, σ-phase was not found in the studied alloys.

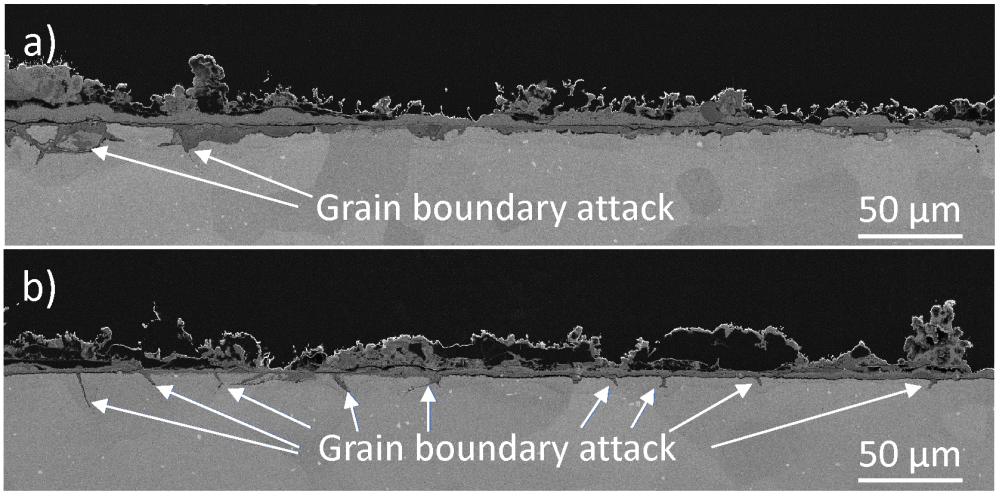

Figure 58: SEM-BSE cross section images of a) Fe15CrAlSi and b) Fe20CrAlSi after exposure to 5% O_2 + 20% H_2O + N_2 (bal.) in the presence of KCl at 600 °C for 168 hours in a tube furnace.

Pronounced Cr-depletion and possible void formation was observed along the attacked grain boundaries, especially at higher depth, see Figure 59a. Similar Cr-depletion was also observed along grain boundaries that does not yet display grain boundary attack, see Figure 59b. Depletion of Cr in the region adjacent to the grain boundaries are sometimes attributed to the formation of Cr-carbides [124]. However, similar to σ-phase no Cr-carbides were found in the grain boundaries. Jonsson et al. suggested that the preferential attack of the grain boundaries in the presence of HCl(g) was connected to the formation of voids along the grain boundaries because of the rapid outward flux of Cr and Fe and that metal chlorides preferentially form along these voids [125]. Because of the high ionic conduction of metal chlorides, this could lead to further increase in outward flux of Cr an Fe and as a result, the propagation of void formation along the grain boundaries can be accelerated. The correlation between this phenomenon and the elevated Cr content in the alloys is not fully understood but could be connected to the increased ability of these alloys to form chromium chloride, $CrCl_2$. Similar void formation was observed by Phother with TEM and FIB/3D reconstruction after exposure of 304L with continuous deposition of KCl [117].

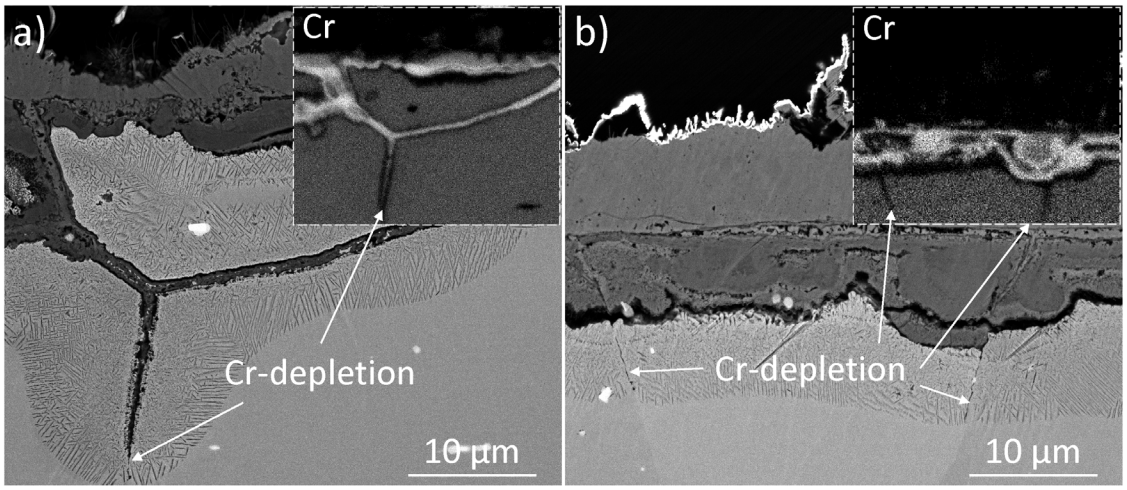

Figure 59: SEM-BSE cross-section images of Fe15CrAlSi after exposure to 5% O_2 + 20% H_2O + N_2 (bal.) in the presence of KCl at 600 °C for a) 48 hours and b) 168 hours. The inserts in the top right corners of each image is the corresponding SEM-EDX map of Cr.

Investigating the corrosion behavior of the FeCrAlSi model alloys showed that the presence of Si enhanced the previously observed influence of Cr and Al on the secondary protection. Even with a Cr content of 5 wt% (Fe5CrAlSi) the corrosion rate within the secondary regime was shown to be significantly reduced in comparison to the FeCr(Al) alloys with <18 wt%/<25 wt% Cr (FeCrAl/FeCr). The FeCrAlSi alloys with elevated Cr content (≥15 wt%) displayed similar corrosion rate to FeCr(Al) alloys with ≥18 wt%/≥25 wt% Cr (FeCrAl/FeCr). However, in the presence of KCl, elevated Cr content was also shown to make the alloys more susceptible to grain boundary attack which demonstrates the importance of finding a balance between the positive and negative aspects of elevated Cr and Si content in different types of environments. The inward-growing scales of Fe5CrAlSi, Fe10CrAlSi and Fe15CrAlSi (outer part) were identified as spinel with EBSD analysis. The inward-growing scales (of all studied alloys in this section) that did not display elevated Cr-enrichment were therefore interpreted as spinel type oxide.

Two important microstructural differences between the alloys forming fast-growing oxide scales and the alloys that formed slow-growing oxide scales within the secondary corrosion regime could be isolated: The alloys forming slow-growing oxide scales (except Fe2.25Cr) display reaction zones underneath the oxide scale and the alloys that formed slow-growing oxide scales displayed significant Cr-enrichment throughout or in the lower part of the inward-growing oxide scale. The alloys displaying intermediate corrosion rates (Fe18Cr1Al and Fe5CrAlSi) also exhibited reaction zones and no pronounced Cr-enrichment.

Jonsson et al. discussed the formation of reaction zones, as a type of internal oxidation, associated with the rapid oxidation rate after breakaway oxidation [54, 105]. These were shown to consist of nanosized Cr-rich spinel precipitates surrounded by Cr-depleted metal. A phase diagram for the FeCr system at 600 °C was calculated with Thermo-Calc, see Figure 60. The phase regions show what phases are thermodynamically stable at different pO_2 and cationic concentrations of Cr (Cr/(Fe+Cr+Al)). S and C denotes spinel and corundum type oxide, respectively and the subscripts Fe and Cr signify if the phase is Fe- or Cr-rich. In two-phase regions, the composition of each phase is given by the extremes of the tie lines across the phase region. However, the phase diagram in Figure 60 shows a part of a ternary phase diagram (triangle). In ternary diagrams the tie lines in a two-phase region might not be completely horizontal and the extremes of these are therefore not possible to determine from the binary diagrams. Such data can be extracted from the software if needed. Note that phases with the same subscripts can have different compositions depending on which phase regions they belong to.

Phases without a subscript, such as C, can belong to the entire range of Cr concentration. The two-phase region BCC_{Fe} + S_{Cr}, i.e. iron-rich metal and Cr-rich spinel, corresponds to the reaction zone. The absence of a reaction zone for Fe2.25Cr can be explained by the low Cr content, resulting in the inability to form Cr-rich spinel precipitates (or very few). The alloys that displayed formation of reaction zones (except Fe5CrAlSi) exhibited a peculiar microstructure in the inward-growing oxide scale, displaying dense and porous regions which alternated in a periodic manner and with a reducing frequency closer to the metal/oxide interface. The porous structure is believed to be remnants of the reaction zone. Jonsson et al. suggested that the iron-rich metal in the reaction zone rapidly oxidize, leaving pores behind and in turn results in a poorly protective oxide scale, which allows for rapid transport of oxidizing species through the oxide scale [105]. The periodicity of the dense and porous bands is not fully understood. However, considering that the porous bands in the inward-growing oxide scale should enable faster transport of oxygen through the oxide scale, the underlying metal may be exposed to different conditions than the previously oxidized metal, i.e. a higher oxygen partial pressure. According to the phase diagram in Figure 60, the new conditions may be outside the stability region for the reaction zone (pO_2 above 10^{-25} atm). In the absence of a reaction zone a dense spinel can form. This would result in a reduced oxygen partial pressure and an eventual transition into the two-phase region (reaction zone). With time, these alternation in phase stability could result in a continuous loop of rapid oxidation. The transitions between the phase regions might take longer as the total oxide thickness increases, which would explain the reduced periodic frequency of the alternations closer to the metal/oxide interface. The rapid oxidation of the iron-rich metal in the reaction zone could explain why the alloys that formed fast-growing oxide scales in the secondary corrosion regime displayed similar oxidation kinetics as low-alloyed steels and iron under the same conditions [92, 98, 110].

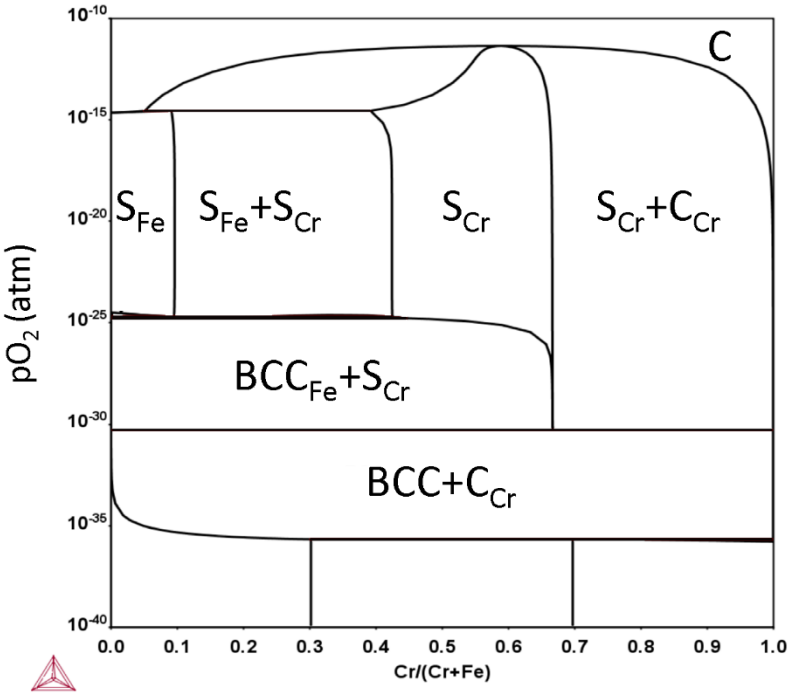

Figure 60: A phase diagram for the FeCr system at 600 °C calculated with Thermo-Calc.

The concept of the formation of a healing layer is often brought up in association to breakaway oxidation and subsequent transition into a lower oxidation rate [19, 106, 107, 126-128]. For chromia-forming steels, Cr-enrichment close to the oxide/metal interface is generally interpreted as the formation of a Cr-rich $(Fe_x, Cr_{1-x})_2O_3$ corundum-type healing layer. While this may occur rapidly at elevated temperatures (above 800 °C) it may take longer at lower temperatures (around 600 °C) [129].

Additionally, the healing layer must form faster than the iron-rich oxide scale grows. This was demonstrated by Fe10Cr, Fe18Cr, Fe10Cr3Al, which easily formed a primary protection in dry O_2 but was not able to form a healing layer after transitioning into the secondary corrosion regime in the presence of Cr-depleting species because of the high growth rate of the iron-rich oxide scale. In contrast, the more highly alloyed FeCrAl(Si) alloys instantly displayed significantly lower oxide growth rates after losing the primary protection, i.e. before a healing layer should be able to form.

To further investigate the nature of the Cr-enrichment in the inward-growing part of the slow-growing oxide scales, more detailed microstructural analysis was performed on selected alloys, displaying good secondary protection (Fe18Cr3Al, Fe25Cr3Al, Fe15CrAlSi and Fe20CrAlSi). This was done by lifting out thin lamellae from the BIB cross-sections for TEM analysis as described in sections 7.1.5 and 7.1.6. The characterization is described in more detail in Papers II and V.

The entire inward-growing oxide scale of Fe18Cr3Al was highly enriched in Cr (60-65 cat%) with a relatively low Al content of about 15 cat%, see Figure 61. Beneath the oxide scale, the alloy is depleted in Cr to a depth of about 1 µm. The total concentration of Cr and Al in the inward-growing oxide scale is 75-80 cat%. Similar to Fe18Cr3Al, the entire inward-growing oxide scale of Fe25Cr3Al displayed high Cr-enrichment (about 70 cat%) while the Al content remained at about 15 cat%, see Figure 62. The total concentration of Cr and Al is therefore about 85 cat%. Cr-depletion was found underneath the oxide scale to a depth of about 800 nm. Void formation had occurred directly beneath the oxide scale, which could be connected to the depletion of Cr.

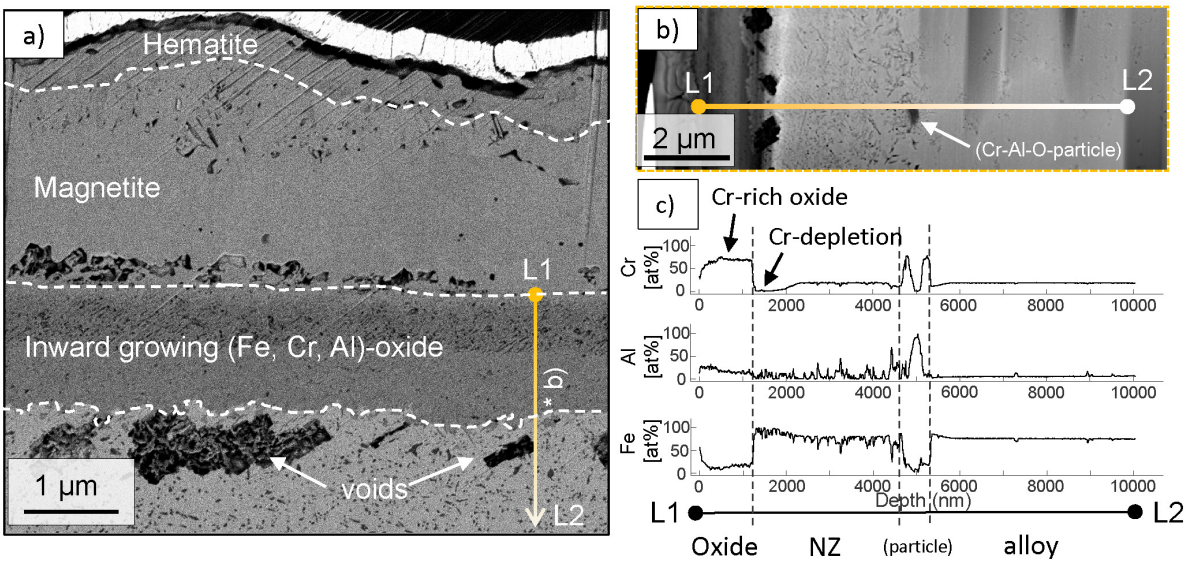

Figure 61: a) SEM-cross section image and b) STEM-HAADF image (of TEM lamella) of a representative area of Fe18Cr3Al after exposure to 5% O_2 + N_2 (bal.) in the presence of K_2CO_3 at 600 °C for 48 hours. The line L1 to L2 corresponds to the STEM-EDX line-scan presented in c).

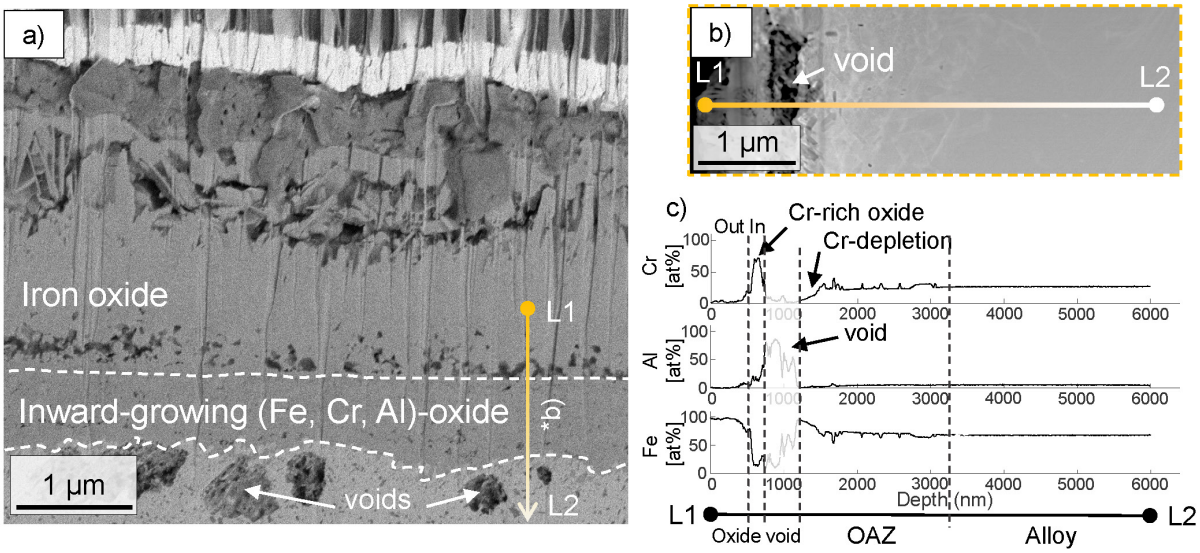

Figure 62: a) SEM-cross section image and b) STEM-HAADF image (of TEM lamella) of a representative area of Fe25Cr3Al after exposure to 5% O_2 + N_2 (bal.) in the presence of K_2CO_3 at 600 °C for 48 hours. The line L1 to L2 corresponds to the STEM-EDX line-scan presented in c).

The oxidation state of Cr and Al are generally more restricted to be trivalent in comparison to Fe that can be both di- and trivalent [130]. Even though Cr is able to be divalent, a study by Liang et al. strongly indicated that Cr was present in the trivalent state and positioned mainly in the octahedral sites when investigating the valency and site position of Cr in magnetite with varying amounts of Cr [131]. Since the structure of the spinel oxide ($(M^{2+}M_2^{3+})O_4$), in which the divalent ions mainly occupy the tetrahedral sites and the trivalent ions mainly occupy the octahedral sites, the maximum amount of di- and trivalent ions are limited to 33.3 cat% and 67.7 cat%, respectively. That the total concentration of Cr and Al in the inward-growing scale exceeded the limit of trivalent ions for both Fe18Cr3Al and Fe25Cr3Al suggests that they are not of spinel type.

Convergent-beam electron diffraction (CBED) was performed to determine the crystal structure of the inward-growing oxide scales of Fe18Cr3Al and Fe25Cr3Al. The CBED pattern in Figure 63a[1] is in agreement with the spinel crystal structure, strongly indicating the presence of spinel type oxide in the inward-growing scale of Fe18Cr3Al even though it exceeds the theoretical limit of trivalent ions. This may be explained either by a) trivalent Cr ions are reduced into divalent Cr ions or b) trivalent Cr ions occupy tetrahedral sites. An example of a spinel type oxide in which the trivalent ions occupies a larger portion of tetrahedral sites is Maghemite (γ-Fe2O3), which consists only of trivalent iron ions [132]. One third of the trivalent ions occupy tetrahedral sites while two thirds occupy octahedral sites. The charge neutrality was shown to be maintained by the presence of cation vacancies, located at octahedral sites [133]. While the configuration may not be thermodynamically stable, this shows that it is possible to exceed the limit of 67.7 cationic% trivalent ions in a spinel type oxide. However, the CBED pattern in Figure 63b[2] suggests that the inward-growing scale of Fe25Cr3Al is a corundum type oxide. This indicates that the Cr-rich spinel is meta-stable and may eventually transform into a corundum type oxide or that both spinel and corundum are present simultaneously. A transformation from a Cr-rich spinel to a corundum structure may take place more rapidly with a higher Cr content.

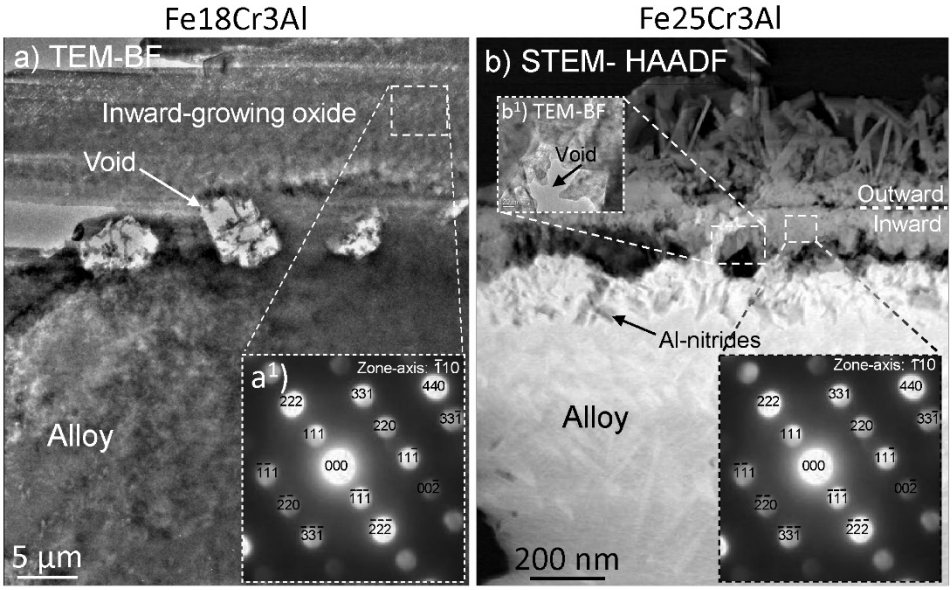

Figure 63: a) TEM-BF image of Fe18Cr3Al and b) STEM-HAADF of Fe25Cr3Al after exposure to 5% O_2 + N_2 (bal.) in the presence of K_2CO_3 at 600 °C for 48 hours. a[1]) and b[2]) shows the CBED patterns in the inward-growing oxide of the respective alloys.

Even though the FeCrAlSi model alloys were exposed in a more corrosive environment (water vapor and KCl), Fe15CrAlSi displayed similar oxidation kinetics as Fe18Cr3Al. However, the composition is not homogeneous throughout the inward-growing scale of Fe15CrAlSi, see Figure 64. The upper part of the inward-growing scale (II), consists of about 40 cat% Cr and 10-20 cat% Al while the underlying layer (III) consists of about 65 cat% Cr and 15 cat% Al. The Si content remains constant throughout the inward-growing scale at about 10 cat%. This confirms that a SiO_2 scale has not formed but that Si is incorporated in the inward-growing scale. When Si (tetravalent) is present in a spinel, such as ringwoodite, it occupies the tetragonal sites [134]. Thus, the upper layer (II) in Figure 64 does not exceed the theoretical limit of trivalent ions in a spinel type oxide while the Cr-rich layer (III) does. Beneath the oxide scale, Cr is depleted to a depth of 500 nm. Similar to Fe18Cr3Al and Fe25Cr3Al, Fe20CrAlSi displayed a high Cr content throughout the entire inward-growing scale, see Figure 65. However, while the lower part of the scale displays a Cr content of about 60 cat%, the upper part of contains 100 cat% Cr, indicating the formation of a pure chromia layer. The alloy is depleted in Cr to a depth of about 400 nm beneath the oxide scale. However, even though both Fe15CrAlSI and Fe20CrAlSi displayed high Cr-enrichments in the inward-growing oxide scale, the CBED patterns in Figure 66 corresponds to a spinel crystal structure. The porous and dense regions of the inward-growing scale formed on Fe15CrAlSi displayed identical CBED patterns.

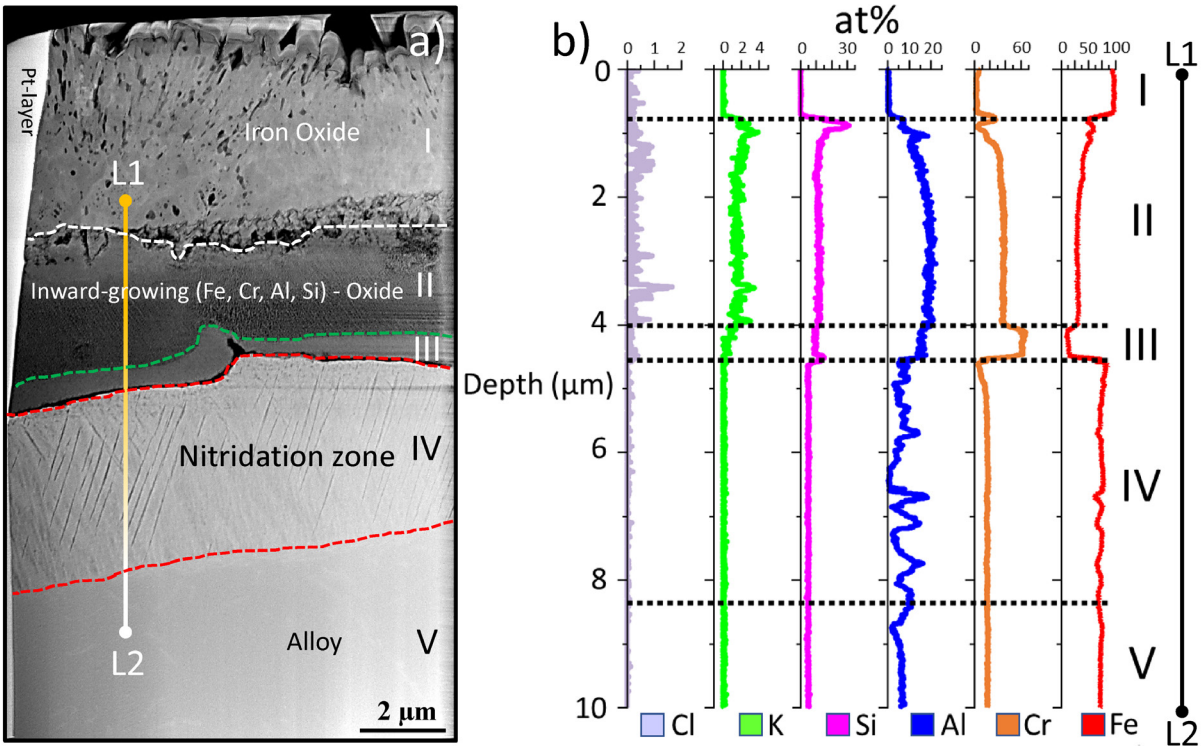

Figure 64: a) STEM-HAADF image (of TEM lamella) of Fe15CrAlSi after exposure to 5% O_2 + 20% H_2O + N_2 (bal.) in the presence of KCl at 600 °C for 48 hours. The line L1 to L2 in a) corresponds to the STEM-EDX line-scan presented in b).

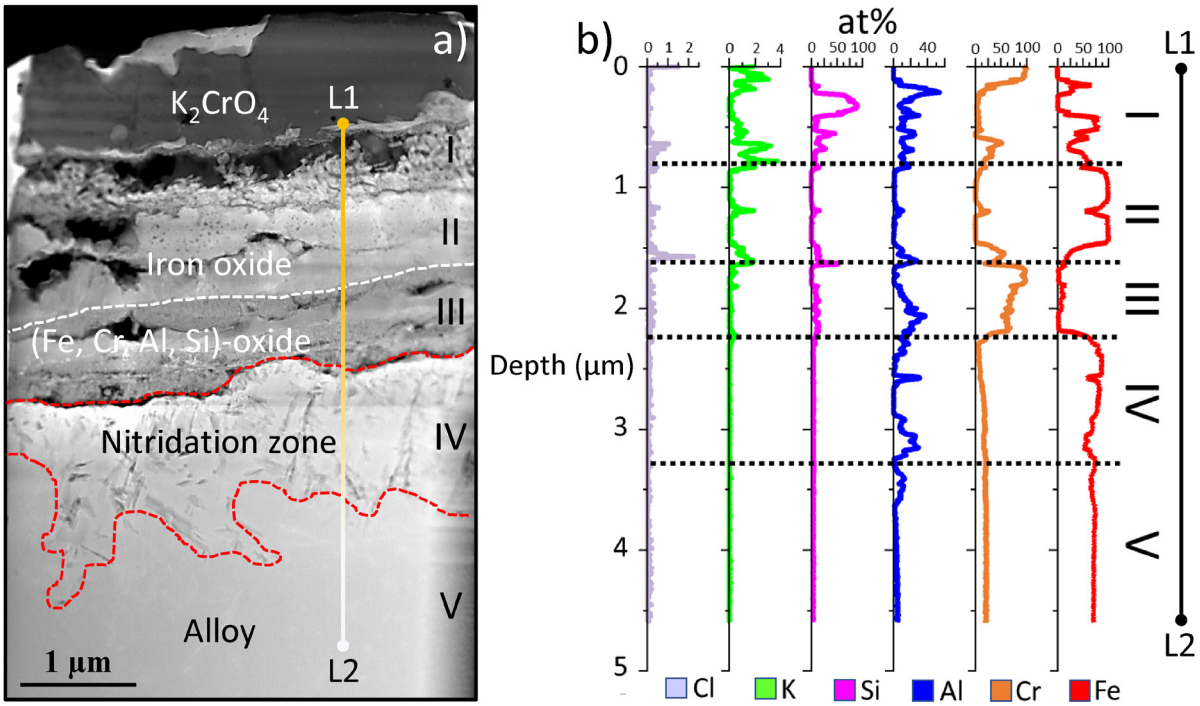

Figure 65: a) STEM-HAADF image (of TEM lamella) of Fe20CrAlSi after exposure to 5% O_2 + 20% H_2O + N_2 (bal.) in the presence of KCl at 600 °C for 48 hours. The line L1 to L2 in a) corresponds to the STEM-EDX line-scan presented in b).

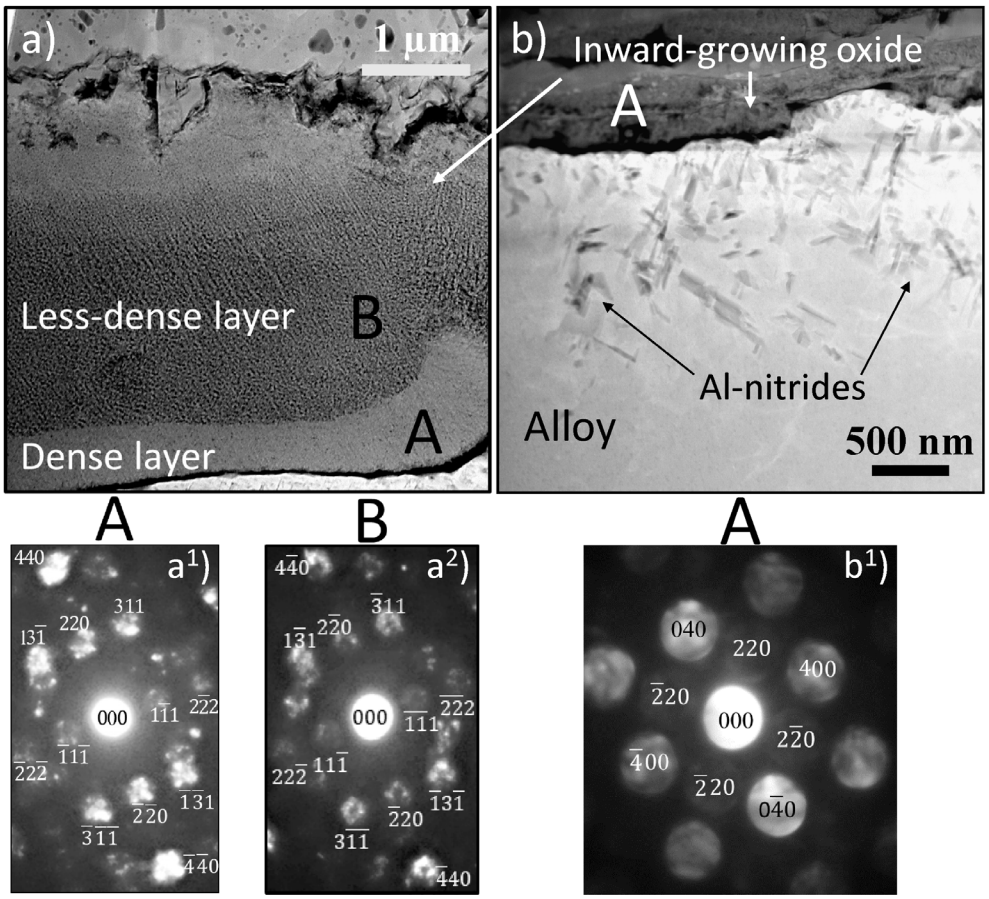

Figure 66: STEM-HAADF images of a) Fe15CrAlSi and b) Fe20CrAlSi after exposure to 5% O_2 + 20% H_2O + N_2 (bal.) in the presence of KCl at 600 °C for 48 hours. a[1]) and a[2]) shows the CBED patterns for region A and B (Cr-rich), respectively, in the inward-growing scale of Fe15CrAlSi and b[1]) shows the CBED pattern in location A of the inward-growing scale of Fe20CrAlSi.

The detailed microstructural analysis confirmed the enrichment of Cr in the inward-growing part of the slow-growing oxide scales. Even though exceeding 67.7 cat% trivalent ions, the presence of spinel was detected in the inward-growing scales of Fe18Cr3Al, Fe15CrAlSi and Fe20CrAlSi. However, this does not mean that they do not contain corundum type oxide as well. Col et al. identified Cr-rich spinel co-existing with Cr-rich corundum type oxide close to the metal/oxide interface of the inward-growing scale formed on a 304L sample after exposure in dry O_2 at 850 °C for 312 hours. This is predicted by the FeCr phase diagram at higher concentrations of Cr (S_{Cr}+C_{Cr}), see Figure 60. The presence of corundum type oxide in the inward-growing scale of Fe25Cr3Al, indicates that the Cr-rich spinel is not stable under the exposure conditions and that phase transformation into a corundum type oxide will occur, given enough time. Upon formation of a slow-growing Cr-rich scale, depletion of Cr in the underlying metal is expected. The depths of the depletion zones (Cr) underneath the oxide scales were found to be in the range 400 to 1000 nm. A depletion zone to a depth of 40 nm could be expected after 1 hour of exposure based on extrapolated diffusivity data of binary Fe–Cr alloys at 600 °C (D_{Cr} of $10^{-14.5}$ cm^2 s^{-1}) [135, 136]. Jonsson et al. found that the actual depth of the depletion zone of a Fe10Cr model alloy was about 80 nm, i.e. slightly higher than the estimated value [105]. Even though the diffusivity of Cr in FeCrAl alloys may deviate from those reported for Fe-Cr alloys, the much longer depletion zones found in the present study indicates that the depletion of Cr started at an early stage of the exposure and not during the final hours. These observations strongly suggest that the early transition into sub-parabolic behavior for the alloys forming slow-growing oxide scales is caused by the formation of the highly Cr-enriched scale which is in agreement with the concept of the formation of a healing layer after transitioning into the secondary corrosion regime. However, this does not explain

why alloys such as Fe18Cr, which clearly are able to form a primary protection in the absence of Cr-depleting species, does not form similar healing layers or show any indications of Cr-enrichment in the inward-growing oxide scale. This indicates that Al may have a vital role in the ability of an alloy to form a healing layer.

The most important criteria that need to be fulfilled in order to form a healing layer is a) the alloy contains enough Cr and/or Al to form a primary protection and b) the formation of healing layer must be faster than the growth rate of the iron-rich oxide scale. Because of the high oxidation rate of the alloys displaying a poor secondary protection, these are not expected to fulfill the second criteria. The slow-growing oxide scales displayed lower growth rate even before the transition into sub-parabolic behavior, i.e. before the potential formation of a Cr-rich healing layer, which is vital for fulfilling the second criteria. Thermodynamic calculations can offer a viable explanation to this phenomenon. Considering the reaction zone once more, which was suggested to cause high oxidation rates because of the formation of a porous inward-growing scale and rapid oxidation of the Cr-depleted metal in the reaction zone. That the oxidation kinetics for all alloys displaying a poor secondary protection is similar to pure iron and low-alloyed steels strongly suggests that iron oxidation is the rate-determining factor. In that case rapid oxidation will occur as long as the reaction zone is thermodynamically stable. The phase diagrams for the FeCr(Al) system in the pO_2 range 10^{-30} to 10^{-25} atm at fixed concentrations of Al at 600 °C are shown in Figure 67b-d. Similar to the phase diagram for the FeCr system, the composition of the phases in different regions can be extracted from the software if needed. The phases $C_{L\text{-}Cr}$ and $C_{H\text{-}Cr}$ in the phase diagrams in Figure 67c-d signifies corundum type oxide with a low or high Cr content, respectively. Note that the subscripts are used to simplify the interpretation of the phase diagram. For example, $C_{L\text{-}Cr}$ does not necessarily mean that it is very low in Cr but rather that it is less Cr-rich than $C_{H\text{-}Cr}$. The phase diagrams indicate two important differences. Firstly, the stability range (Cr concentration) of the reaction zone (BCC_{Fe}+S_{Cr}) is reduced upon addition of Al. In the absence of Al, the reaction zone is stable up to 67 cat% Cr while it is only stable up to 32 cat% Cr with 15 at% Al (including oxygen). At the same time, the phase diagrams shows that the concentration of Cr at which the transition into the two or three-phase region(s) (S_{Cr}+C_{Cr}, S_{Cr}+$C_{L\text{-}Cr}$ and S_{Cr}+$C_{L\text{-}Cr}$+$C_{H\text{-}Cr}$) where spinel is in equilibrium with corundum is reduced with increasing concentration of Al. Since the inward-growing scales of the FeCr model alloys Fe2.25Cr, Fe10Cr and Fe18Cr contained less than 67 cat% Cr (see Paper I), these are expected to form reaction zones and not be able to reach a high enough Cr content to transition into the (S_{Cr}+C_{Cr}) phase region. The transition into slow oxide scale growth, displayed by Fe25Cr, may be caused by a sufficiently rapid enrichment of Cr to move out of the stability range for the reaction zone (exceeding 67 cat% Cr), but since Fe25Cr was not further analyzed no conclusions can be drawn. The inward-growing scales of the FeCrAl alloys Fe5Cr3Al and Fe10Cr3Al were found to be contain less than 32 cat% Cr (see Paper I) while the inward-growing scale of Fe18Cr3Al is expected exceed this Cr concentration at an early stage of the oxidation process, which explains the sudden transition from the formation of fast-growing to slow-growing oxide scales between Fe10Cr3Al and Fe18Cr3Al. Note that the thermodynamic calculations should not be considered an exact prediction but rather an indication of the involved driving forces and the direction towards which the oxidation process may proceed.

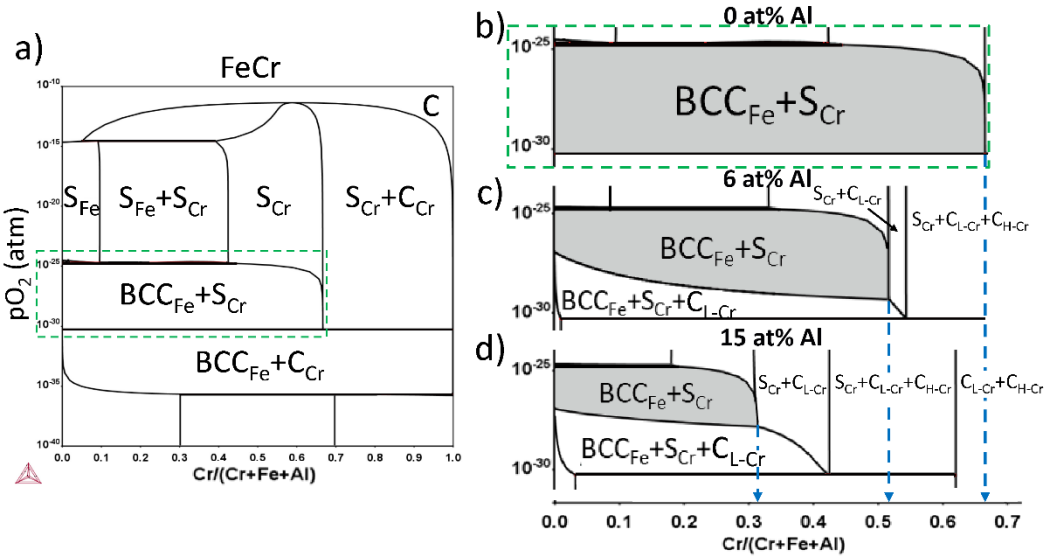

Figure 67: Phase diagrams for the FeCr(Al) system at 600 °C calculated with Thermo-Calc. b) is a magnified FeCr diagram indicated by the green square in a). c) and d) corresponds to the phase diagrams at fixed Al concentrations of 6 and 15 at%, respectively. The blue dotted lines signify the maximum Cr-content at which the two-phase region, BCC_{Fe}+S_{Cr}, is stable.

The thorough investigation of a range of different FeCr(Al, Si) model alloys in different harsh environments in combination with thermodynamic calculations strongly suggests that the criteria for the formation of slow-growing oxide scale within the secondary regime is the ability of an alloy to rapidly transition outside of the stability region for the reaction zone. As expected, this occurred faster for alloys with elevated Cr content since the Cr-concentration in the inward-growing scale more rapidly reaches the critical values during the iron-depletion caused by the formation of outward-growing iron oxide. Less expected was the beneficial influence of Al on the stability range of the reaction zone, enabling leaner alloys to form slow-growing oxide scales within the secondary corrosion regime. Similar observations were found upon the addition of Si but the influence of the incorporation of Si in the spinel crystal structure is not fully understood. Nevertheless, Si clearly enabled even leaner (in Cr) FeCrAl alloys to form slow-growing oxides within the secondary regime.

The presence of KCl seemed to suppress the enrichment of Cr in the inward-growing scale. This was indicated by the difference in corrosion rates in the tube furnace and the thermobalance, displayed by FeCrAl2Si and Fe10CrAlSi. These are expected to be on the border of being able to rapidly exceed the critical limit (Cr content) for forming slow-growing oxide scales and might therefore be more affected by the higher amount of KCl. When the presence of KCl in the vicinity of the metal/oxide interface is reduced, either by evaporation of KCl or by an increased oxidation depth, these alloys are finally able to transition into the protective behavior. In addition, KCl was found to trigger grain boundary attack for alloys with elevated Cr content. The mechanism behind this effect is not fully understood but may be of great importance of the performance of alloys in harsh environments.

8.2 Utilizing coatings for mitigation of high temperature corrosion in harsh environments

Utilizing coatings to mitigate the material degradation cause by high temperature corrosion is a highly desirable concept. It is desirable both because of its economic aspects, i.e. the utilization of expensive highly alloyed steels without exceeding economic limits, and that mechanical properties are not as crucial since the coating is not responsible for pressure-bearing capabilities. However, two factors that highly complicate the implementation of coatings, especially in very harsh environments, are the adhesion of the coating to the substrate and the density of the coating [137, 138]. Adhesion is

dependent on the interaction between the substrate and the coating, and how well the coating wets the surface of the substrate. This interaction differs between different coating techniques. For example, an overlay welded coating is partially melted together with the substrate, resulting in stronger adhesion between the coating and the substrate than with thermally sprayed coatings. The adhesion of thermally sprayed coatings is dependent on how well the coating particles deform at the substrate surface, which in turn is dependent on the acceleration and temperature of the sprayed particles. In addition to the degree wetting, the difference in thermal expansion is an important aspect when it comes to the adhesion of a coating, especially during thermal cycling. If the thermal expansion coefficient differs largely between the substrate and the coating, the thermal stresses can lead to delamination. The density of a coating is especially important in harsh environments that contains highly corrosive species. If a coating contains a large degree of open pores, these corrosive species will be able to diffuse through the coating and eventually reach the substrate, which will result in rapid material degradation. The present study mainly focuses on the corrosion resistance of two different types of coatings in terms of oxidation behavior and their ability to protect the underlying substrate. The two coating techniques are thermal spraying (HVAF) and overlay welding.

8.2.1 HVAF coatings

As mentioned in section 3.2, the thermal spraying technique HVAF is capable of producing coatings with very high density, good adhesion and low oxide content in comparison to many other thermal spraying techniques (such as HVOF and APS), because of the high particle velocity and relatively low particle temperature of the HVAF technique [29, 30]. These are crucial parameters for the performance of coatings in corrosion protection in harsh environments.

The performance of three HVAF-sprayed coatings with different compositions were investigated by exposing them to highly corrosive environments in tube furnaces followed by microstructural characterization as described in sections 6.1.3.1 and 7.1. The thermogravimetrical and microstructural analysis after exposure in the two corrosive environments (O_2 + H_2O with and without KCl present) will be presented and discussed in the sections below.

8.2.1.1 O_2 + H_2O

It has previously been shown that the HVAF coatings NiCr, NiAl and NiCrAlY succeed in protecting a substrate when exposed to ambient air at 600 °C as these coatings formed thin protective oxide scales (50-130 nm) [139]. However, due to the high levels of water vapor in the flue gas in biomass- and waste-fired boilers, the understanding of the influence of water vapor on the corrosion protective performance of the coatings is of great importance.

As described in section 4.5.1, chromia-forming steels often experience Cr evaporation in humid environments at elevated temperatures due to the formation of gaseous chromium(VI) oxy hydroxide ($CrO_2(OH)_2$). It is therefore expected that the Cr-containing coatings in this study will exhibit a higher degree of corrosion attack in the presence water vapor than in the presence of dry O_2. Accordingly, the coatings did not display mass gains indicative of the formation of a primary protection when exposed to O_2 + H_2O at 600 °C for 168 hours, see Figure 68. The calculated oxide scale thicknesses of the coatings, based on the mass gains, ranged from 0.6 – 1 µm. However, the metallic luster remained on the coating surface, indicating that the primary protection had not been lost. This was confirmed with SEM analysis, which showed no thick oxide scale on the surface of any of the coatings, see Figure 69. The relatively high mass gains of the coatings may originate from areas at which the coating is not fully covering the substrate (difficult to fully cover edges of the substrate).

SEM analysis revealed that all coatings had a significant degree of porosity, mostly originating from splat boundaries (the coating microstructure is further described in Paper VI). Open networks of pores

can act as transport paths for corrosive species through the coating. The NiCr coating had formed oxide in the pores, but not the NiAl and NiCrAlY coatings, see EDX-map inserts in Figure 69. SEM-EDX analysis of a non-exposed NiCr coated sample confirmed that the oxide formation within the coating took place during exposure (see Paper VI).

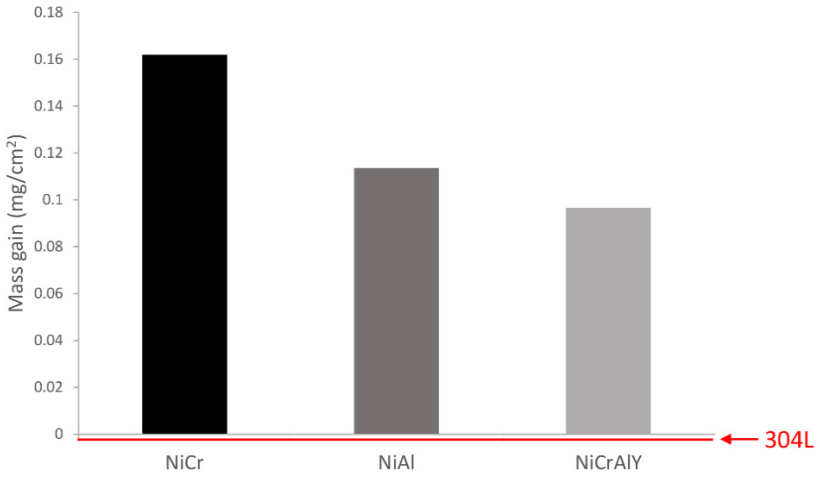

Figure 68: Mass gains of coated samples after exposure to 5% O_2 + 20% H_2O + N_2 at 600 °C for 168 hours. The red line shows the mass gain of a bulk 304L sample exposed under the same conditions.

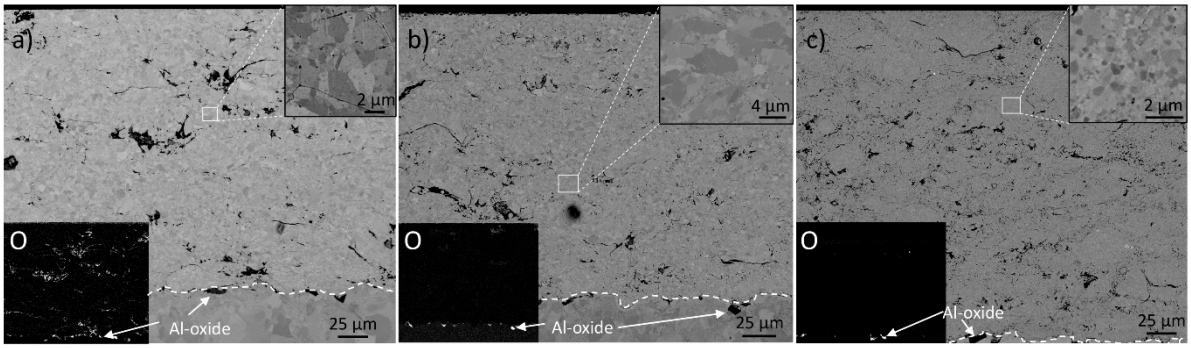

Figure 69: SEM-BSE cross-section image of the a) NiCr, b) NiAl and c) NiCrAlY coatings after exposure to 5% O_2 + 20% H_2O + N_2 at 600 °C for 168 hours. EDX map for oxygen added in bottom-left corner for each coating specimen. The dashed line shows the coating/substrate interface. The Al-oxide observed at coating/substrate interface are remains from the grit-blasting of the substrate.

The grain size can have significant effects on the protectiveness of coatings since smaller grains could increase the diffusion rate of Cr and/or Al to the surface of a coating and facilitate the formation of a Cr- and/or Al-rich oxide scale. The NiCr and NiAl coatings had grain sizes in the range of 0.5-5 µm, which is larger than the grain size of the NiCrAlY coatings (0.2 – 1 µm). Thus, the NiCrAlY may be able to form a protective oxide scale faster, which would prevent the diffusion of corrosive species through the coating. The composition of the thin protective oxide scale (primary protection) can also be a contributing factor since a Cr-rich oxide scale is more susceptible to Cr evaporation, which may explain the inability of the NiCr coating to prevent internal oxidation. However, all coatings managed to protect the substrate from exposure to the surrounding environment.

8.2.1.2 O_2 + H_2O + KCl

As described in sections 4.5.2 and 4.5.3, chromia-forming steels exhibit a drastically accelerated corrosion rate in the presence of KCl at high temperatures due to the loss of the protective Cr-rich scale because it reacts with KCl to form K_2CrO_4 according to Reaction 4.4. Jafari et al. have recently studied the corrosion behavior of HVAF-sprayed NiCr, NiAl and NiCrAlY coatings in ambient air at 600

°C with KCl present for 168 hours [140]. It was found that all three coatings managed to protect the substrate from corrosion attack during the time interval of the exposure. However, corrosion behavior differed significantly between the coatings. The NiCr coating formed a fast-growing oxide scale, while the NiCrAlY coating displayed a significantly reduced corrosion attack and the NiAl coating seemed to retain the primary protection.

Since the combustion of biomass and waste results in a flue gas with high amounts of both water vapor and alkali compounds (such as alkali chlorides) [75, 141], understanding the corrosion behavior of coatings in an environment containing both of these corrosive species is of the utmost importance. For this reason, the coatings were exposed to water vapor and KCl simultaneously.

The corrosion behavior of the coatings differed greatly when exposed to wet O_2 in the presence of KCl, demonstrated by the mass gains in Figure 70. The NiCr coating exhibited a drastically increased mass gain comparison to the other coatings. The NiAl coating exhibited a negative value for the mass gain, which indicates that the mass gain from oxide formation is lower than the mass loss from evaporation of KCl (found to be high in the studied conditions, see section 8.1.2. 304L bulk samples were exposed under the same conditions as reference and displayed mass gains similar to that of the NiCr coating.

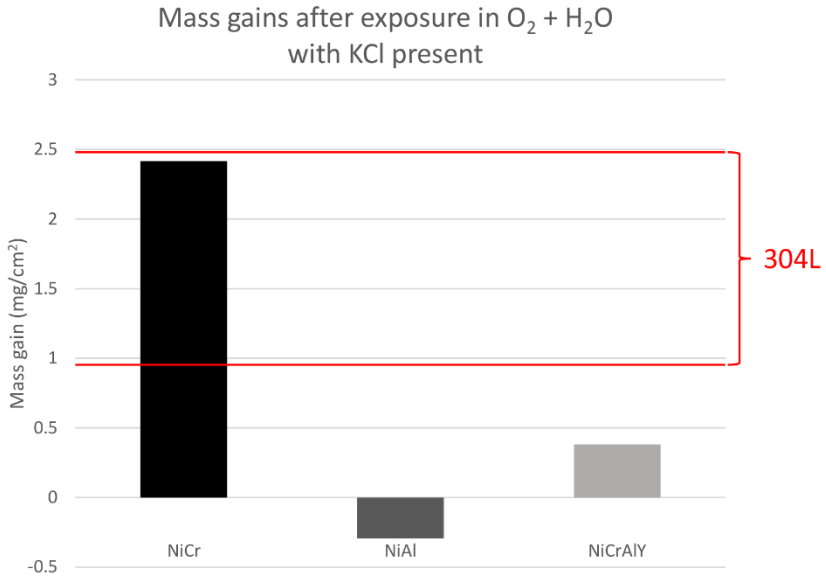

Figure 70: Mass gains of coated samples after exposure to 5% O_2 + 20% H_2O + N_2 at 600 °C in the presence of KCl for 168 hours. The red lines display the mass gain range (based on measured oxide thickness) for a bulk 304L sample exposed under the same conditions for 168 hours.

SEM analysis showed that the NiCr coating had indeed experienced a severe corrosion attack in the presence of KCl and have transitioned into the secondary corrosion regime, see Figure 71. In addition to the formation of a thick multi-layered oxide scale (45-65 µm) and K_2CrO_4, cracks had formed in the coating, which seem to have originated from delamination along splat boundaries. These cracks are expected to further facilitate the diffusion of corrosive species through the coating. Accordingly, Cl had diffused through the coating to a large extent, which was indicated by the formation of metal chlorides close to the coating/substrate interface. The magnified image in Figure 71 (right) shows that Cl was present at the coating/substrate interface, which means that the NiCr coating was no longer fully protecting the substrate from the corrosive environment. The EDX-analysis indicated that the Cl had diffused through the coating along the splat boundaries, see EDX-map in Figure 71.

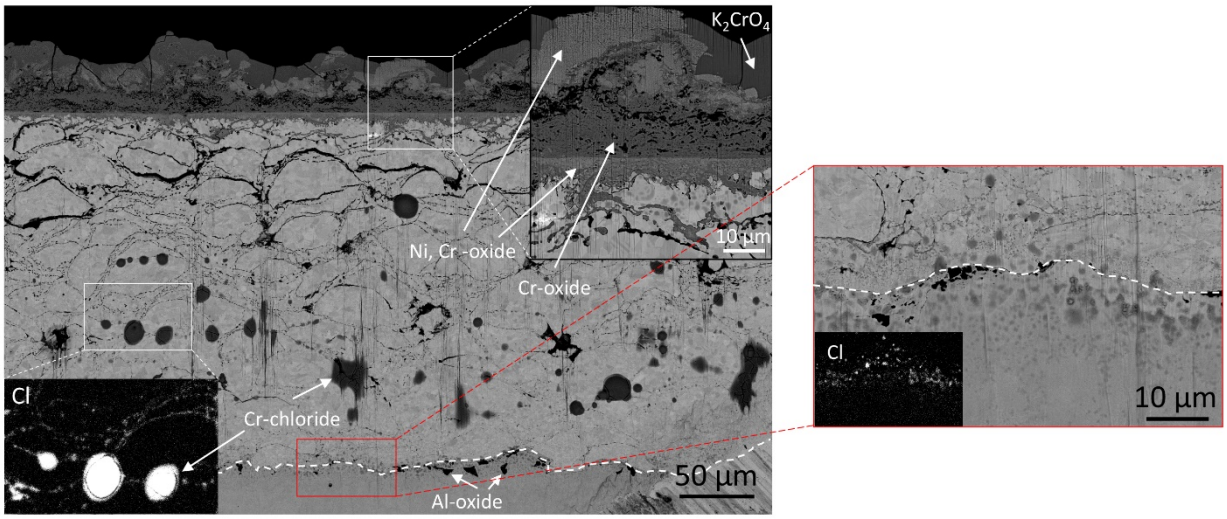

Figure 71: SEM-BSE cross-section image of NiCr coating after exposure to5% O_2 + 20% H_2O + N_2 at 600 °C in the presence of KCl for 168 hours. The dashed line shows the coating/substrate interface. Al-oxide remaining from grit blasting of the substrate was observed at coating/substrate interface.

The NiAl coatings were expected to reveal minor corrosion attacks attributable to the negative mass gain value. Accordingly, SEM analysis showed no significant corrosion attack on the NiAl coating, which indicates that it managed to retain the primary protection, see Figure 72. Only minor oxide formation, rich in Al, was seen close to the surface of the coating. No KCl was seen on the surface of the NiAl coating, which indicates that the majority of the deposited salt evaporated, hence the significantly negative mass gain. NiAl coating was able to fully protect the substrate from exposure to any corrosive species since no Cl was detected within the coating or at the coating/substrate interface. The reason for the large differences in corrosion behavior between the NiCr and the NiAl coating can be attributed to rapid formation of an Al-rich scale on the NiAl coating surface that resists the present corrosive species. Similarly, the NiCrAlY coating displayed a protective behavior and no Cl was detected in the coating or at the coating/substrate interface, see Figure 73. K_2CrO_4 was found on the NiCrAlY coating surface. Cr was found to have accumulated along the splat boundaries underneath the K_2CrO_4, which can be explained by the higher driving force for Cr to diffuse to the coating surface to resupply the protective oxide scale after depletion.

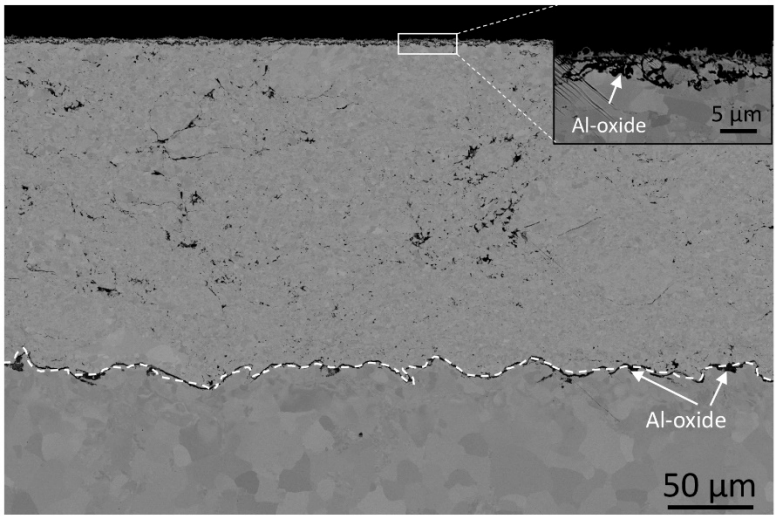

Figure 72: SEM-BSE cross section image of NiAl coating after exposure to 5% O_2 + 20% H_2O + N_2 at 600 °C in the presence of KCl for 168 hours. The dashed line indicates the coating/substrate interface. Al-oxide remaining from grit blasting of the substrate was observed at coating/substrate interface.

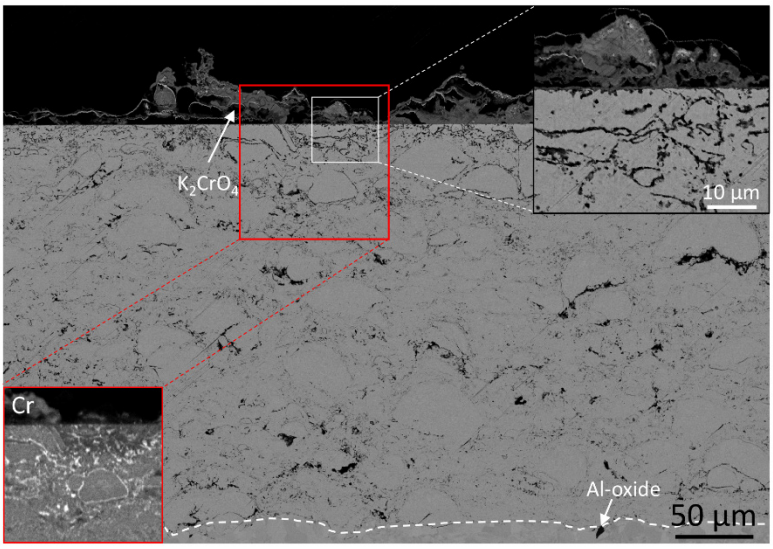

Figure 73: SEM-BSE cross section image of NiCrAlY coating after exposure to 5% O_2 + 20% H_2O + N_2 at 600 °C in the presence of KCl for 168 hours. The box in the bottom left corner shows the EDX-map for Cr. The dashed line indicates the coating/substrate interface. Al-oxide remaining from grit blasting of the substrate was observed at coating/substrate interface.

As mentioned in the beginning of section 8.2.1, the HVAF technique have been shown to produce significantly denser coatings than other thermal-spraying techniques. Nevertheless, the HVAF-sprayed coatings investigated in this work was shown to be significantly more porous than a bulk material. the relatively porous nature was found to be detrimental for the corrosion resistance in the secondary corrosion regime. However, upon rapid formation of a primary protection the coatings displayed excellent corrosion resistance. The ability of the NiCrAlY and NiAl coatings to rapidly form and retain the primary protection in the presence of KCl may be connected to the high Cr and Al content and the fine-grained microstructure that enables fast transport of Cr and Al to the coating surface.

8.2.2 Overlay welds

Overlay welding is a good approach to increasing the corrosion resistance of components used in harsh environments without affecting their pressure-bearing capabilities. Overlay welding can also be used to repair degraded components on-site. Because of these advantages, overlay welding has been utilized in different types of boilers (coal-, biomass- and waste-fired boilers), mainly the water walls but also for superheaters [45, 46, 142, 143]. The majority of studies on overlay welds with a focus on coal-, biomass- and/or waste-fired boilers, examined Inconel 625 (denoted IN625 in this work). This is because Inconel 625 is often chosen in commercial applications when utilizing overlay welding [144]. The studies on Inconel 625 overlay welds have generally been performed in the field and has been found to drastically reduce material degradation of underlying substrates [142, 144-146].

In the present study, the martensitic steel Super VM12 was coated with three different alloys using overlay welding, of which two were FeCrAl alloys and one was a nickel-based alloy (IN 625). These were exposed to a simplified laboratory environment at 600 °C (described in section 6.1.3.2), mimicking the biomass- and waste-fired boiler, for 500 hours. With the laboratory set-up used, the deposited KCl remained on the surface of the samples during the entire exposure. Uncoated Super VM12 was exposed simultaneously as a reference.

The mass gains after 500 hours of exposure are presented in Figure 74. The mass gains of the uncoated SVM12 samples were based on the area of all sides of the samples, while the mass gains of the coated samples were based only on the side with overlay weld. As expected in this relatively harsh

environment, the uncoated SVM12 displayed a very high mass gain (roughly 10-14 mg/cm^2). FeCrAl197 contains 1.3 wt% Si, which was found to significantly reduce the oxidation rate of FeCrAl alloys within the secondary corrosion regime (section 8.1.2). However, the data presented in Figure 74 instead shows that FeCrAl197 exhibited as poor a secondary protection as SVM12 (same mass gain). This could be connected to longer exposure to large amounts of KCl in the present set-up, which was found to significantly inhibit the transition into sub-parabolic oxidation kinetics in section 8.1.2.

Both Kanthal APMT and Inconel 625 (IN625) displayed significantly lower mass gains (about 5 mg/cm^2). Kanthal APMT is a more highly alloyed FeCrAl alloy than the two model FeCrAl alloys and is therefore expected to display a better secondary protection, as shown in section 8.1.2. Israelsson et al. have published several studies on KCl-induced high temperature corrosion of Kanthal APMT at 600 °C [15, 147, 148]. These studies have shown that Kanthal APMT generally exhibits mass gains in the range of 0.1-0.5 mg/cm^2 after 168 hours of exposure (0.1 mg/cm^2 KCl). In previous non-published work, bulk Kanthal APMT samples displayed mass gains of 0.5-0.9 mg/cm^2 after 168 hours exposure to similar conditions (1 mg/cm^2 KCl). However, in contrast to these exposures, the present laboratory set-up was designed to inhibit the evaporation of KCl so that it remains on the surface throughout the entire exposure. The significantly higher corrosion rate of Kanthal APMT in the present study demonstrates the higher corrosivity of the experimental set-up. Previous research on IN 625 in the studied environment is scarce but the available studies showed corrosion rates similar to those observed in the present study [149, 150].

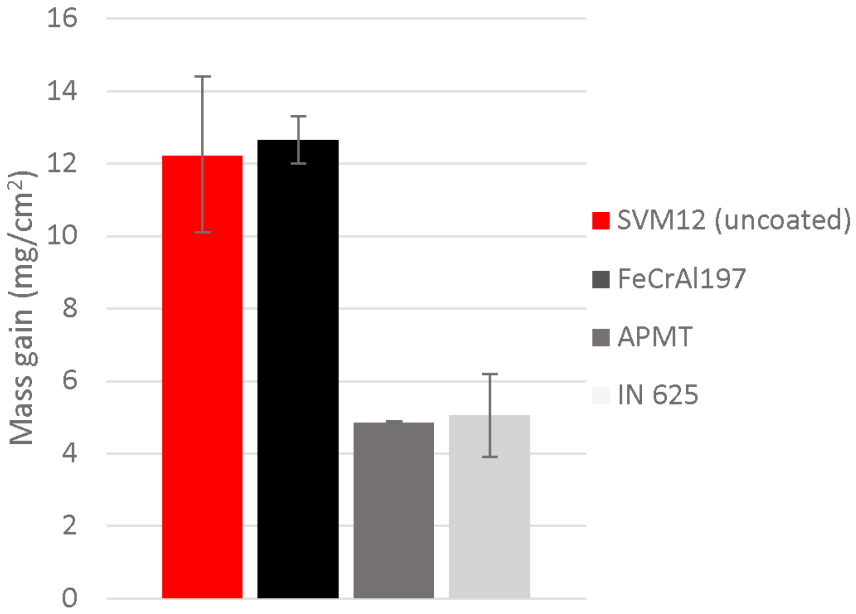

Figure 74: Average mass gains of uncoated and overlay welded SVM12 with error bars showing min. and max. mass gain of each alloy/coating after exposure to 5% O_2 + 20% H_2O + N_2 (bal.) at 600 °C in the presence of KCl for 500 hours.

SEM analysis of the alloys that displayed a poor secondary protection, i.e. SVM12 and FeCrAl197, revealed similar oxide scale thickness (about 130 µm) and microstructure, see Figure 75 and Figure 76. However, FeCrAl197 had formed a slower-growing oxide scale in some areas (about 70 µm). The iron-rich oxide scales consisted of outward-growing iron oxide and inward growing (Fe, Cr, (Al))-oxide scale (interpreted as spinel). Beneath the oxide scale, the alloys had formed reaction zones. However, FeCrAl197 also displayed nitridation zones underneath the reaction zone. SEM-EDX analysis showed that the concentration of Cr was similar for both alloys (30-40 cat%) while FeCrAl197 also contained 15 cat% Al and 5 cat% Si. According to the phase diagrams presented in section 8.1.2, SVM12 is expected to be within the stability region of the reaction zone (Figure 67a-b), while FeCrAl197 may be

in range with the higher Cr concentration at which the reaction zone is stable (Figure 67d). This could explain the presence of both a reaction zone and a nitridation zone for FeCrAl197, which indicates a transition into protective behavior.

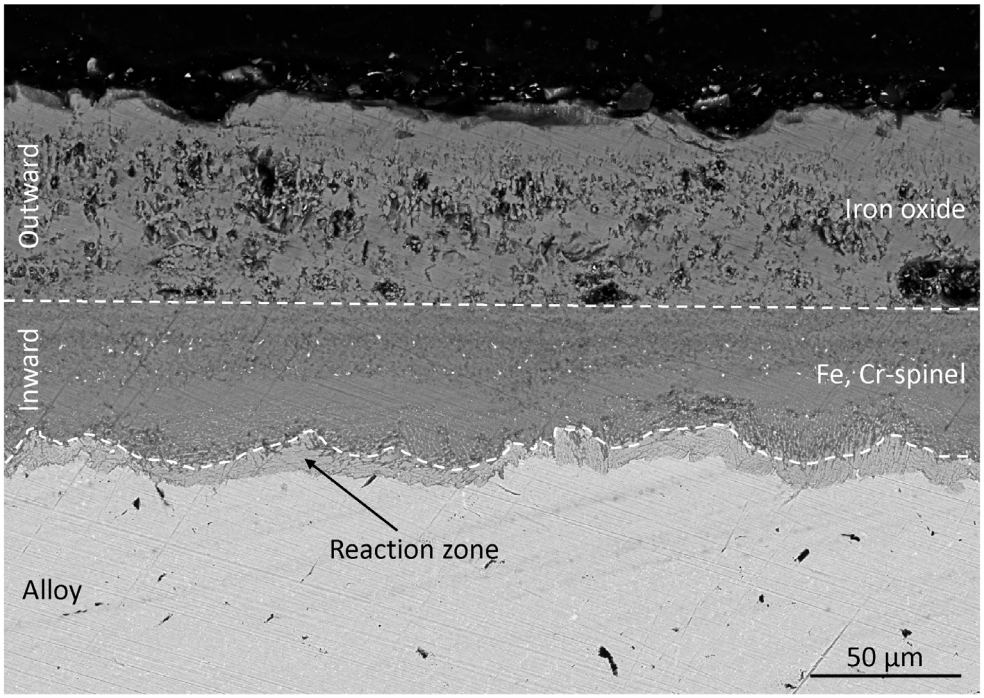

Figure 75: SEM-BSE cross section image of SVM12 after exposure to 5% O_2 + 20% H_2O + N_2 (bal.) at 600 °C in the presence of KCl for 500 hours.

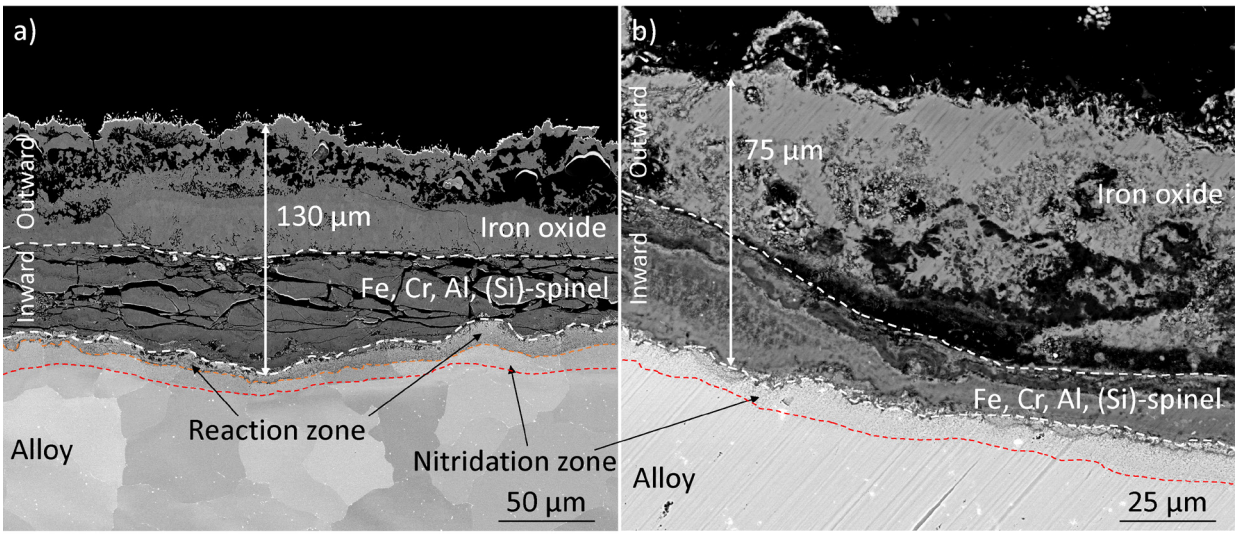

Figure 76: SEM-BSE cross-section images of two FeCrAl 197 overlay welds after exposure to 5% O_2 + 20% H_2O + N_2 (bal.) at 600 °C in the presence of KCl for 500 hours. The cross section in a) was prepared with BIB milling, and the one in b) was prepared with mechanical polishing.

The average oxide scale thickness of Kanthal APMT was found to be much lower than those of SVM12 and FeCrAl197 but was varying greatly over the surface (3-60 µm). Higher oxide scale thickness was found under large amounts of K_2CrO_4, indicating a suppressing effect of KCl similar to that observed in the laboratory studies (section 8.1.2). The absence of a reaction zone indicates that this transition into protective behavior has occurred on the entire sample. The inward-growing scale was found to contain 50-60 cat% Cr and about 20 cat% Al, i.e. Kanthal APMT is expected to be outside of the stability range

(Cr content) for the reaction zone (Figure 67d), which agrees with the observation that no reaction zone was found anywhere on the sample. Higher Cr content was found in areas at which the total oxide scale thickness was lower, which suggests that these regions transitioned into protective behavior at an earlier stage.

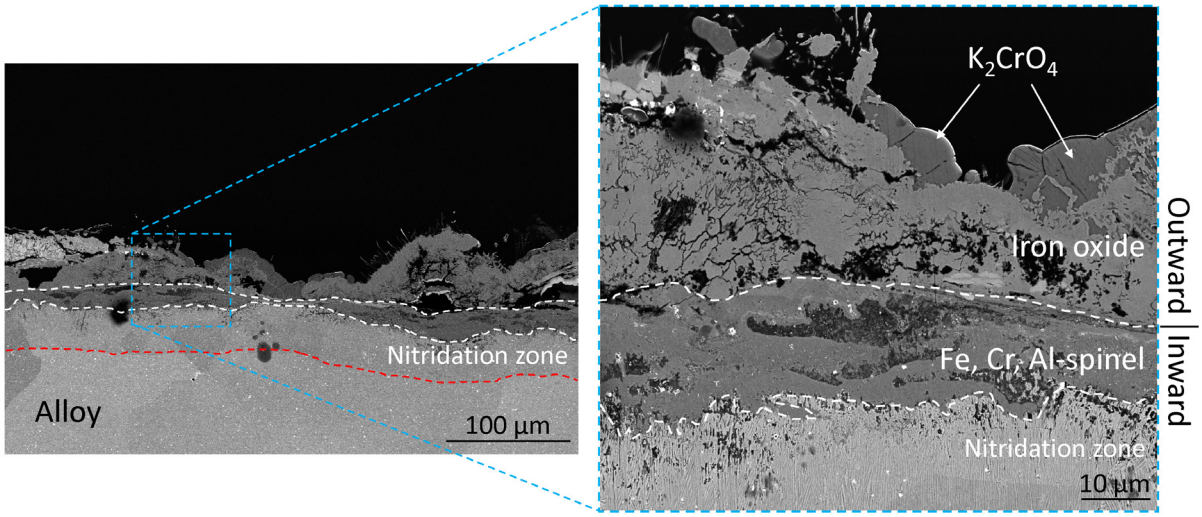

Figure 77: SEM-BSE cross-section images of an APMT overlay weld after exposure to 5% O_2 + 20% H_2O + N_2 (bal.) at 600 °C in the presence of KCl for 500 hours.

The oxide scale thickness of the IN625 overlay weld was found to be in the range 10-40 µm (see Figure 78), i.e. similar to the Kanthal APMT overlay weld. The oxide microstructure differed in relation to the Fe-based alloys. Firstly, the thickness ratio of outward- and inward-growing oxide was roughly 80:20 (outward:inward), i.e. significantly lower proportion of inward-growing scale than for Fe-based alloys. Secondly, the outward-growing oxide was Ni-rich (up to 70 cat%). However, similar to Kanthal AMPT and other Fe-based alloys that displayed low oxidation rates within the secondary corrosion regime, the inward-growing scale of IN625 was enriched in Cr. This was more pronounced in areas with lower oxide scale thickness (up to 60 cat%) while about 40 cat% Cr was found in the thicker oxide scales. This indicates that the Cr content in the inward-growing oxide scale might influence the corrosion resistance of Ni-based alloys similarly to Fe-based alloys in the secondary corrosion regime (formation of a healing layer).

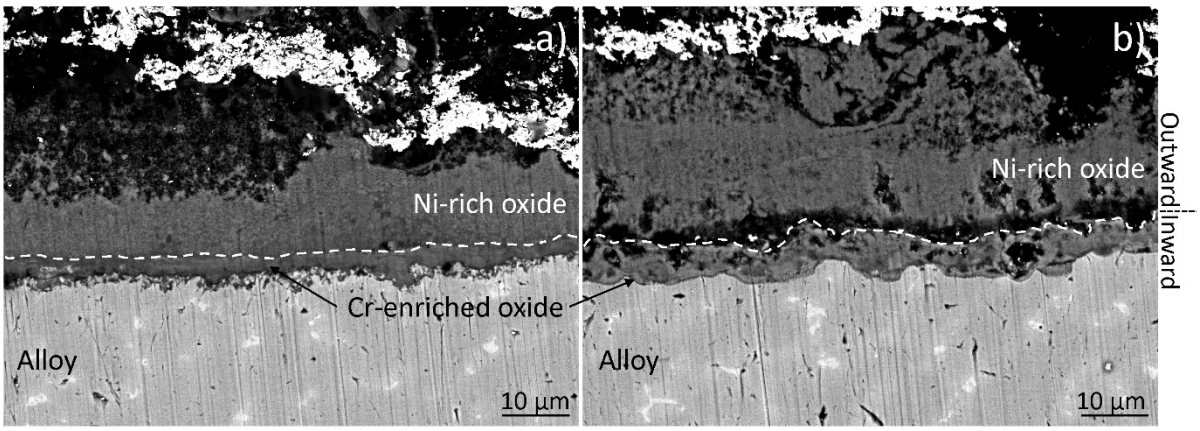

Figure 78: SEM-BSE cross-section images of an IN625 overlay weld after exposure to 5% O_2 + 20% H_2O + N_2 (bal.) at 600 °C in the presence of KCl for 500 hours.

The investigation of the overlay welds presented in this work contributed with several insights. Firstly, overlay welding as a coating technique displayed a density superior to the HVAF-sprayed coatings. This

is one of the most important factors when it comes to protecting a substrate from exposure to corrosive species. Secondly, the observations discussed in section 8.1.2, i.e. that slow-growing oxide scales within the secondary corrosion regime is connected to elevated Cr content in the inward-growing oxide scale and the suppression of a reaction zone, are valid for both Fe-based and Ni-based steels during longer exposures. Additionally, the extended exposure to KCl was found to suppress or postpone the transition into protective behavior which is a relevant aspect for the conditions of an actual biomass- or waste-fired boiler.

8.2.3 Comparison: Overlay welding and HVAF

Because of the different coating chemistries and exposure conditions (exposure time and availability of KCl), no direct comparison can be made between the performance of overlay welds and HVAF-sprayed coatings. However, one of the main differences between the two coatings techniques is density. The HVAF technique was developed with the aim of producing denser and more adherent coatings. This is true when comparing HVAF to other thermal spraying techniques such as HVOF [151, 152]. However, when comparing the density of the HVAF-sprayed coatings with that of the overlay welds, the former displayed a significantly higher degree of porosity. The HVAF-sprayed NiCr coating and the overlay-welded IN625 are similar in composition in terms of being Ni-based with similar Cr content. After 500 hours of exposure, the IN625 overlay weld displayed an oxide scale thickness that was in range with the HVAF-sprayed NiCr coating after 168 hours. The overlay-welded IN625 was exposed for three times as long as the HVAF-sprayed NiCr, which indicates a significantly higher corrosion resistance. However, Lehmusto et al. found that IN625 displayed an average oxide scale thickness of 40 µm after exposure to dry air in the presence of KCl at 600 °C for 168 hours [150], i.e. the oxide scale thickness of IN625 in the present study might not have increased significantly after 168 hours. If so, the most apparent difference between the HVAF-sprayed NiCr coating and the IN625 overlay weld is the inability of the former to prevent diffusion of corrosive species to the substrate.

The two alumina-formers, NiCrAlY (HVAF) and Kanthal APMT (overlay weld) had similar Cr and Al content, with the main difference being that NiCrAlY is Ni-based and APMT is Fe-based. Yet, the corrosion behavior of these differed greatly. Kanthal APMT transitioned into the secondary regime, forming an iron-rich oxide scale, while NiCrAlY seemingly retained the primary protection in the presence of KCl. Bulk APMT samples that were exposed to similar conditions as the HVAF-sprayed coatings (wet O_2 in the presence of KCl for 168 hours) also transitioned into the secondary corrosion regime. This is in agreement with a previous study of Ni-and Fe-based alumina-formers exposed under similar conditions that found that the Fe-based alloys formed iron-rich oxide scales while the Ni-based alloy formed a thin Al-rich scale [153]. In the present study, the seemingly better corrosion resistance of NiCrAlY than for the Kanthal APMT overlay weld could be connected to the more fine-grained microstructure of the NiCrAlY coating (0.2-1 µm) than that of the overlay welded Kanthal APMT (25-250 µm), which enables faster transport of Cr and Al to rapidly form and replenish the primary protection.

It is apparent that many factors influence the corrosion resistance achieved with the investigated coating techniques, including coating chemistry, microstructure and the synergistic effects of these. These, along with the studied environmental parameters, should be considered when choosing the most corrosion resistant option.

8.3 Field studies

A field study is an important concept that provides valuable insights into the most important parameters responsible for a specific phenomenon. This information can be utilized to design a relevant but simplified laboratory set-up. The field studies also verify if the laboratory observations are

valid in the intended application. This work includes two different field-studies, one in a biomass-fired boiler and one in a waste-fired boiler. The materials used in these studies were chosen to ensure an overlap between the laboratory studies (discussed in the previous sections) and the field-studies.

8.3.1 Biomass-fired boiler

As described in section 6.2.2, the biomass-fired boiler in which this field study was performed was a commercial grate-fired CHP boiler. The fuel consisted mainly of wood chips and the boiler environment was therefore expected to be relatively mild in terms of corrosivity. Generally, the flue gas produced when combusting biomass is much less corrosive than the flue gas produced in waste-fired boilers since it contains lower amounts of alkali chlorides [2, 154] which has been attributed to the very low Cl content in biomass and, consequently, a molar ratio Cl/(K+Na) often lower than 1 [2, 155]. In addition, the ash formation is often significantly lower when combusting biomass than when combusting waste. Naturally, the composition of the different types of biomass varies. Among the biofuels, the combustion of straw has been shown to result in one of the more corrosive flue gases (due to a higher concentration of alkali chlorides), while combustion of wood chips or wood pellets has been shown to result in one of the least corrosive flue gases (because of very low concentration of alkali chlorides) [155]. The exposure parameters investigated in this field study were flue gas temperature (at different superheater positions) and material temperature (600 °C and 700 °C, controlled with an air-cooled probe). These parameters can significantly influence flue gas and deposit chemistry. Firstly, the saturation vapor pressure of KCl is higher at a higher flue gas temperature, i.e. a hotter flue gas can contain a higher amount of KCl(g). Secondly, a lower material temperature can result in an increase in the amount of KCl(s) in the deposit since the saturation vapor pressure of KCl is less at lower temperatures, i.e. KCl(g) may condensate to a larger extent on a cooler surface than on a warmer surface if these are exposed to the same flue gas. Thus, a larger temperature difference between flue gas and material may result in higher concentrations of KCl(s) in the deposit. However, the condensation of K_2SO_4(s) and K_2CO_3(s) are also affected by a temperature gradient which can influence the concentration of KCl(s) in the deposit.

Prior to exposure, deposit tests (3 hours) were performed at each superheater position (high and low flue gas temperature) and material temperature. The deposit formation was minor for all parameters (0.02-0.07 g/mm^2) and no clear trends were observed. The extrapolated average deposit formation reached a value of 0.014 g/mm^2 year. The anion concentration (Cl^- and SO_4^{2-}) in the deposit was analyzed using ion chromatography (IC). The measured SO_4^{2-} concentration in the deposit was higher at the position with the higher flue gas temperature (8-12 wt%) than at the position with the lower flue gas temperature (1-4 wt%). The measured Cl^- concentration in the deposit was very low (<1 wt%) and indicated no significant influence by the different parameters. Firstly, the low Cl^- concentration in the deposit indicates a very mild environment. Secondly, the high S/Cl ratio (>8 at high flue gas temperature and >1 at low flue gas temperature) has been shown to prevent or reduce the formation of KCl since the SO_4^{2-} competes with Cl^- for the K^+ to form K_2SO_4 [155]. Salmenoja has shown that the risk of severe corrosion attack is high at S/Cl molar ratios less than 2 but low at S/Cl molar ratios above 4 [156].

As described in section 6.2.1, the material loss measurements were performed by measuring the original sample thickness at 8 points around the sample ring using an ultrasonic thickness gage. The sample thickness after exposure was measured with SEM. The material loss was very low for all alloys and exact comparisons cannot be made because of the relatively low sensitivity of the ultrasonic thickness gage measurements. Oxide formation was not found everywhere around the exposed sample rings with the analytical techniques used but only in certain areas. This can both be a result of spallation of the oxide scale or that the primary protection (very thin oxide scales) was retained in

certain areas. Iron oxide scales were generally detected in areas with larger amounts of deposit (often with traces of KCl).

While the IC analysis of the deposit showed only a minor presence of Cl (less than 1 wt%) regardless of material temperature and superheater position, the SEM analysis indicated a higher presence of KCl in the deposit after exposure at a material temperature of 600 °C and the superheater position with a lower flue gas temperature. This may be connected to the higher S/Cl ratio detected at this superheater position.

The commercial stainless steels 347H, 310 and Sanicro 25 displayed formation of iron-rich oxide scales under both KCl-poor and KCl-rich deposits, see Figure 79, Figure 80 and Figure 81, respectively. The oxide microstructure was similar to those found within secondary corrosion regime in the laboratory studies (section 8.1.2). The average oxide scale thickness was in the range 5-15 µm for all commercial stainless steels, which is in agreement with previous laboratory studies of similar commercial alloys in the presence of KCl at 600 °C [9, 65, 66, 119, 149]. However, the oxide scale thickness was much higher under KCl-rich deposits (up to 110 µm) for 310 and Sanicro 25. It should be noted that the material and flue gas temperature could also influence the growth rate of the oxide scales, but no correlations were observed. Montero et al. found that the corrosion resistance of Sanicro 25 was significantly reduced when exposed in a laboratory environment simulating the conditions during co-firing lignite with biomass (1 wt% KCl in deposit and 500 ppm HCl in gas) in comparison to under lignite-firing conditions [157].

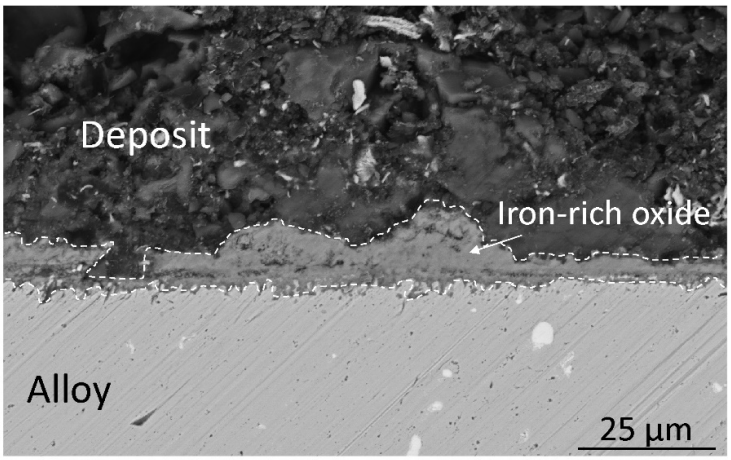

Figure 79: SEM-BSE cross-section image of 347H after exposure inside the biomass-fired CHP boiler at high flue gas temperature and a material temperature of 600 °C for 168 hours.

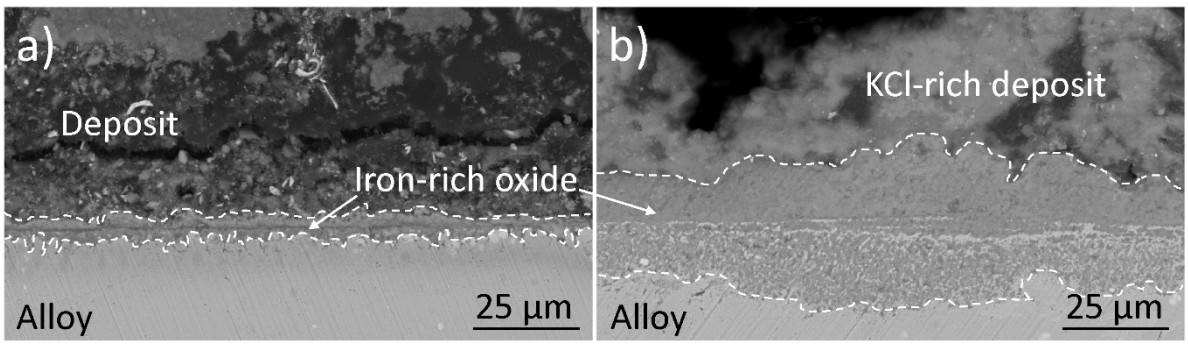

Figure 80: SEM-BSE cross-section images of 310 after exposure inside the biomass-fired CHP boiler at a) low flue gas temperature and a material temperature of 700 °C and b) at high flue gas temperature and material temperature of 600 °C for 168 hours.

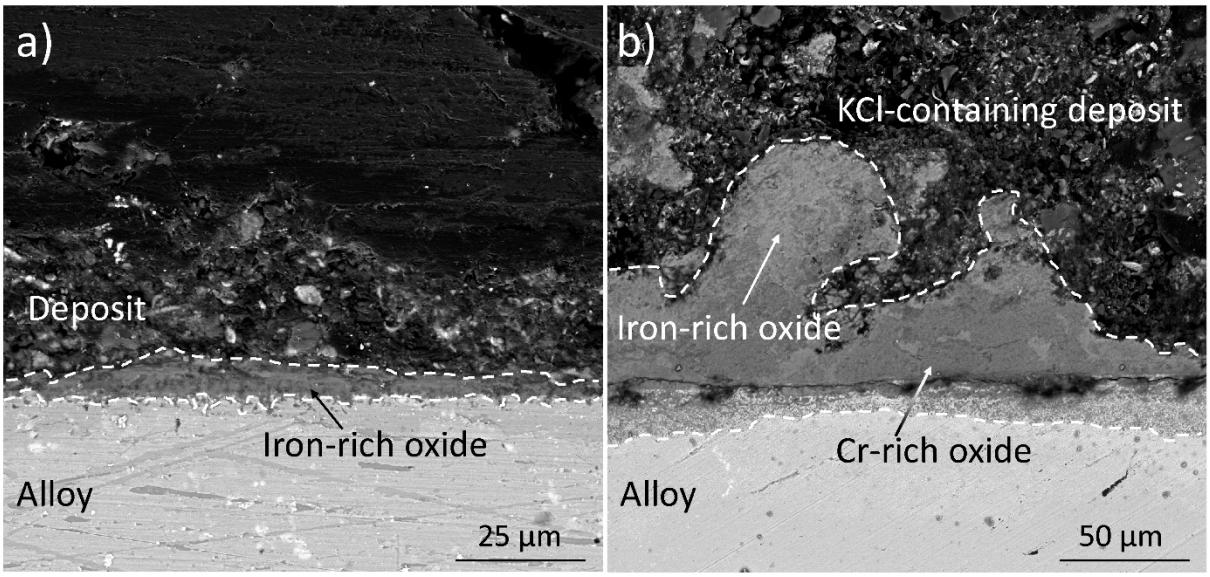

Figure 81: SEM-BSE cross-section images of Sanicro 25 after exposure inside the biomass-fired CHP boiler at a) high flue gas temperature and a material temperature of 700 °C and b) at high flue gas temperature and material temperature of 600 °C for 168 hours.

The FeCrAl alloys displayed a significantly higher corrosion resistance than the commercial stainless steels, see Figure 82, Figure 83, Figure 84 and Figure 85. All FeCrAl alloys were found to retain the primary protection under KCl-poor deposits. The Si-containing FeCrAl alloys were also shown to be able to retain the primary protection (absence of iron-rich oxide scale) under some KCl-rich deposits. The FeCrAl alloys displayed similar oxide scale microstructure (within the secondary corrosion regime) as observed in the laboratory environments. Considering the poor corrosion resistance of the FeCrAl0Si model alloy in the laboratory studies (sections 8.1.1 and 8.1.2), the ability to retain a primary protection when exposed inside the biomass-fired boiler indicates a very mild environment.

The ability of the Si-containing alloys to retain the primary protection under KCl-rich deposits may be connected to the rapid enrichment of Al and Si in the primary scale of FeCrAl alloys observed upon the addition of Si (section 8.1.1). However, the laboratory studies of FeCrAlSi alloys showed that they immediately transitioned into the secondary corrosion regime when exposed in the presence of KCl. This inconsistency can be explained by the higher presence of KCl in the deposit in the laboratory studies (pure KCl salt) than in the biomass-fired boiler (diluted with other compounds), which influences the direct contact between the alloy surface and the KCl salt. The varying corrosion resistance under different KCl-rich deposits may depend on which stage of the exposure that the KCl condensed on the sample surface, i.e. if KCl had condensed at a later stage of the exposure, the primary protection may have had sufficient time to achieve an improved resistance towards the salt. The EDX map in Figure 83 indicates that an Al-rich oxide formed on the surface of FeCrAl2Si. This is agreement with previous research on the effect of the pre-oxidation of FeCrAl alloys, which found that pre-oxidation increased the resistance to KCl [15, 111, 158].

The corrosion resistance of the FeCrAl197 coating was expected to be higher than the corresponding bulk material purely on the basis of the chemical composition of the coating (higher Al and Si content). Accordingly, the HVAF-sprayed FeCrAl197 coating displayed the highest corrosion resistance of all investigated alloys and fully retained the primary protection under all KCl-rich deposits. The microstructure of the HVAF-sprayed FeCrAl197 coating was similar to those presented in section 8.2.1, see Figure 85. The laboratory studies showed that the relatively high porosity of HVAF coatings, in comparison to bulk materials, may be detrimental in the presence of highly corrosive species because

of the higher number of diffusion paths. However, the alumina-forming HVAF-sprayed coatings, NiAl and NiCrAlY, was found to retain the primary protection when exposed to wet O_2 in the presence of KCl (section 8.2.1), which was attributed to rapid transport of Al and/or Cr to the coating surface. Similar mechanisms may be involved in the retention of the primary protection of the FeCrAl197 coating.

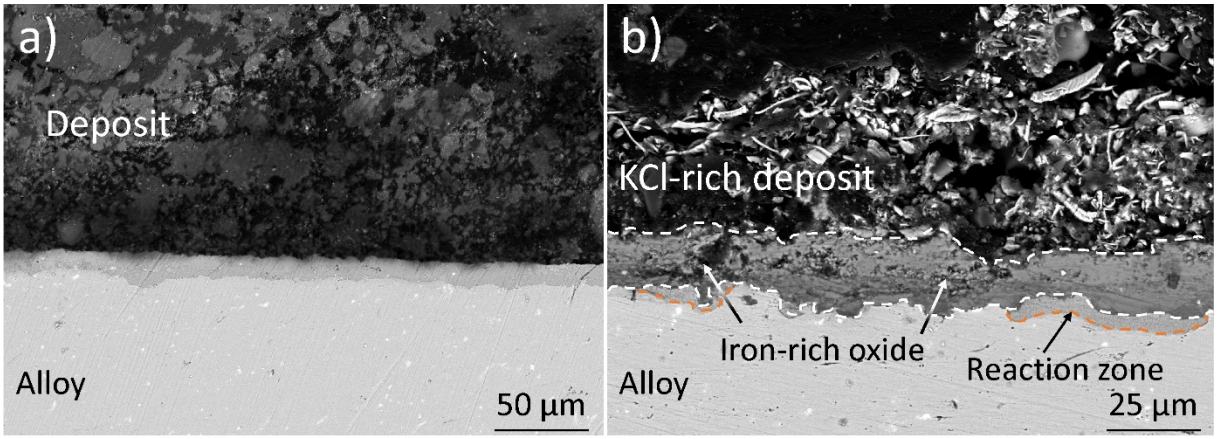

Figure 82: SEM-BSE cross-section images of the FeCrAl0Si model alloy after exposure inside the biomass-fired CHP boiler at a) low flue gas temperature and a material temperature of 700 °C and b) at low flue gas temperature and material temperature of 600 °C for 168 hours.

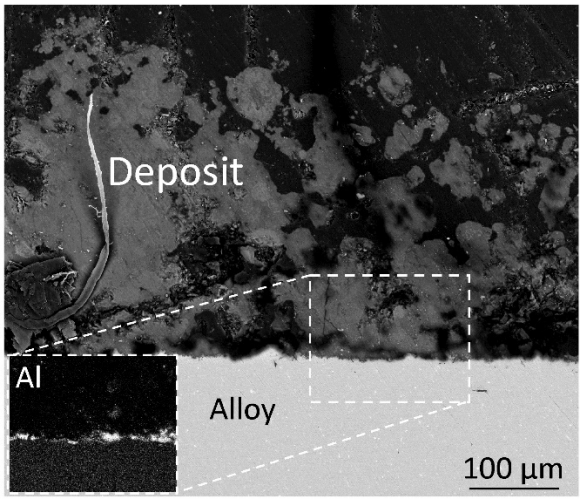

Figure 83: SEM-BSE cross-section images of the FeCrAl2Si model alloy after exposure inside the biomass-fired CHP boiler at high flue gas temperature and a material temperature of 700 °C for 168 hours.

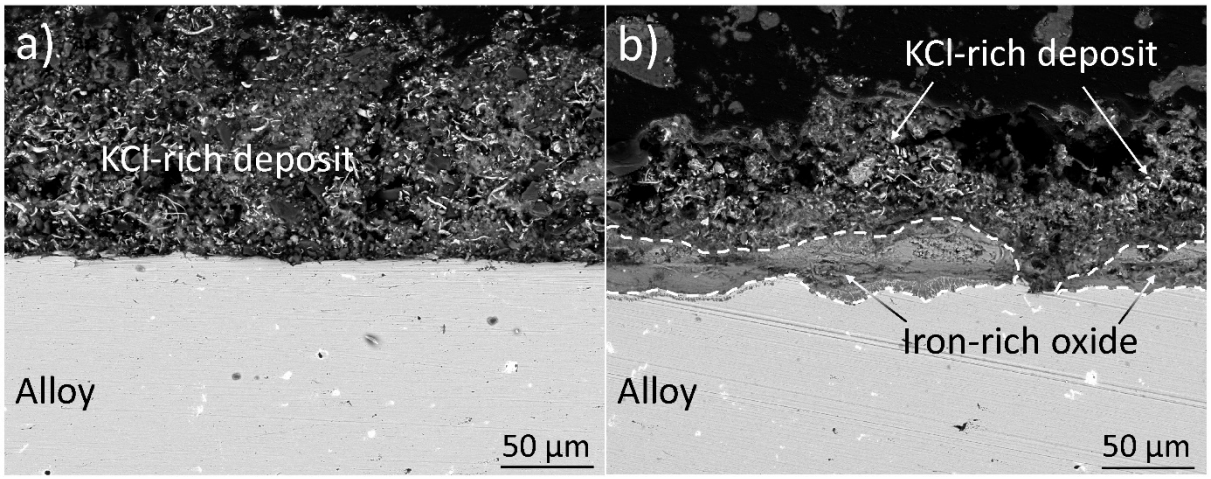

Figure 84: SEM-BSE cross-section images of the FeCrAl197 model alloy after exposure inside the biomass-fired CHP boiler at a) high flue gas temperature and a material temperature of 600 °C and b) at low flue gas temperature and material temperature of 600 °C for 168 hours.

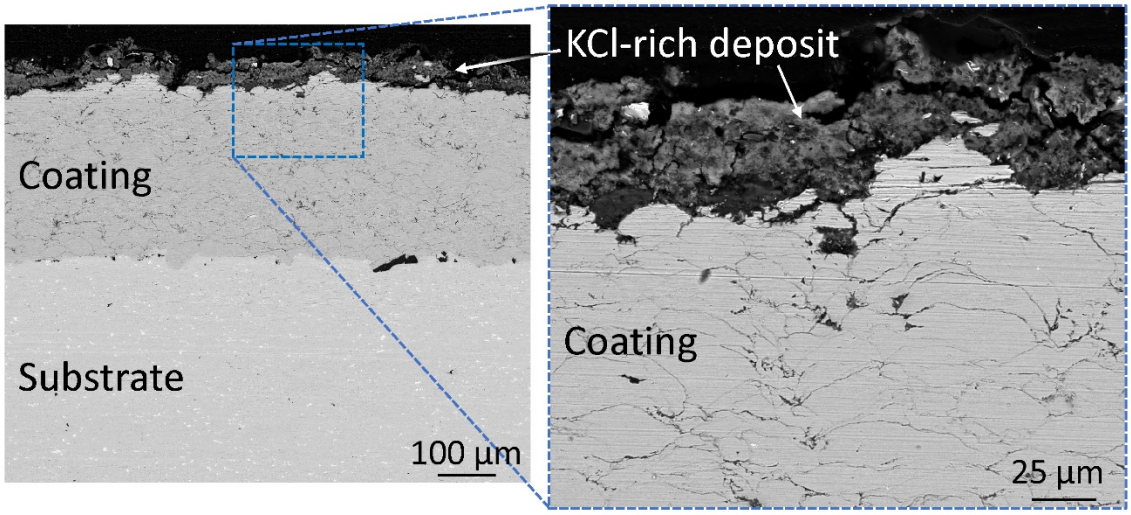

Figure 85: SEM-BSE cross-section images (high and low magnification) of the HVAF-sprayed FeCrAl197 (enhanced) coating after exposure inside the biomass-fired CHP boiler at low flue gas temperature and a material temperature of 600 °C for 168 hours.

The probe exposures inside the biomass-fired boiler displayed a very mild environment, which in some cases resulting in lower corrosion rate than observed in the laboratory studies. This is promising for the flexibility material utilization. In addition, the trends observed in the laboratory studies, i.e. improved corrosion resistance within the primary regime upon the addition of Al and Si, are valid even in this more complex environment.

8.3.2 Waste-fired boiler

One of the most important advantages with combusting waste for heat and electricity generation is the relatively inexpensive fuel. This is because many countries have prohibited land filling with combustible components. However, as mentioned in the previous section, waste-fired boilers have a significantly harsher environment than biomass-fired boilers, resulting in rapid material degradation. This is mainly due to the higher amounts of alkali chlorides produced in the flue gas when waste is combusted [2, 154, 159]. The flue gas composition will vary largely over time because the composition of waste is heterogeneous and, consequently, so will the corrosivity of the environment. Predicting

service stops for maintenance is difficult since the material degradation of boiler components can be more rapid during certain periods.

The present field study in the waste-fired boiler was part of a larger project that aimed to find a superheater positions (Steamboost position) and boiler settings that result in less corrosive flue gas [158]. The Steamboost position was based on Computational Fluid Dynamics (CFD) modelling to identify the position over the grate at which the flue gas has high heat flux and low Cl-concentration. Because of the higher steam temperature and less corrosive flue gas the electrical efficiency of the boiler can be improved without increasing the material degradation of boiler components. The probe exposure of the present study was performed close to the Steamboost position, while the boiler settings were optimized based on a high S/Cl ratio and minimal deposit formation (to achieve optimal heat transfer), see more detailed report in [158]. The flue gas temperature in this position was about 1000 °C. A two-hour deposit test was performed prior to the corrosion test. By extrapolating the collected amount of deposit during the two-hour test, the deposit formation rate was found to be 0.002 g/mm^2 year, which is a relatively slow rate of deposit formation in comparison to the boiler setting that resulted in the highest deposit formation rate (0.035 g/mm^2 year). IC analysis of the collected deposit measured a Cl concentration of 6.5-8 wt%, resulting in a S/Cl ratio of about 0.6. As discussed in the previous section, a S/Cl ratio below 2 indicates a high risk for a severe corrosion attack. However, the relatively low deposit formation rate must also be taken into consideration since this is an important factor that determines the total amount of alkali chlorides present on the samples. However, the present conditions may still be considered very corrosive and a challenging test environment for different materials.

The probe exposure was performed for 672 hours at a material temperature of 600 °C. The exposed alloys were similar to the FeCrAl(Si) model alloys from the laboratory studies (section 8.1.1 and 8.1.2). The aim was to verify the validity of the laboratory observations (improved secondary protection upon addition of Si and Cr) in this much more complex and corrosive environment. The original sample ring thickness was measured at 8 points prior to exposure using an ultrasonic thickness gage as described in section 6.2.1. The sample ring thickness after exposure was measured using SEM analysis. The calculated material loss is illustrated in radar diagrams, see Figure 86 and Figure 89.

FeCrAl0Si and FeCrAl2Si displayed large differences in material loss (Figure 86) after exposure inside the waste-fired boiler, which clearly demonstrates the important influence of Si on corrosion resistance of FeCrAl alloys in harsh environments. This is in good agreement with the laboratory studies in section 8.1.2, which showed that a minor addition of Si greatly improved the secondary protection of the FeCrAl alloys. Both alloys exhibited a higher material loss on the windward side, which was expected because of the direct contact with higher concentrations of corrosive species.

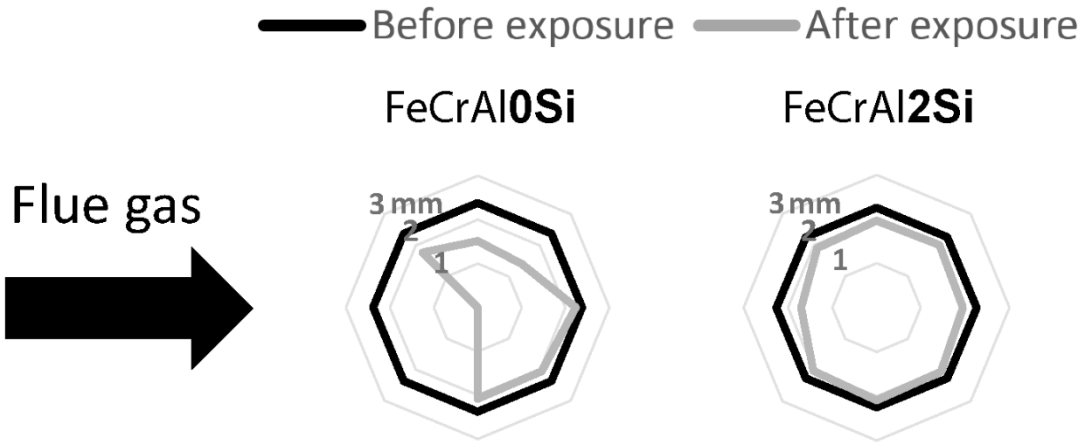

Figure 86: Radar diagrams displaying the material loss around the FeCrAl model alloy sample rings with varying Si content after exposure inside the waste-fired CHP boiler at a material temperature of 600 °C for 672 hours. The arrow on the left illustrates the direction of the flue gas in relation to the sample rings.

FeCrAl0Si performed relatively well on the leeward side where a lower concentration of corrosive species was expected to come in contact with the sample surface. As shown in Figure 87a, the thickness of the iron-rich oxide scale on the leeward side was in the range 80-200 µm. This is in contrast to the windward side, at which the sample ring was almost completely oxidized, see Figure 87b. Meanwhile, FeCrAl2Si displayed a relatively even material loss around the sample ring. A 40-200 µm thick iron-rich oxide scale was found on the surface of FeCrAl2Si on the leeward side (Figure 88a), and a thicker oxide scale (up to 400 µm) was found on the windward side (Figure 88a). Neither of the alloys displayed a multi-layered scale (outward-growing and inward-growing scales). The outward-growing scale might have detached along with the deposit when removing the sample from the air-cooled probe. The significantly higher corrosion rate on the windward side observed for FeCrAl0Si than for FeCrAl2Si showed that the former is more sensitive to the direct contact with the very hot and corrosive flue gas.

Exact comparisons of the corrosion behavior of these alloys under laboratory conditions and inside the waste-fired boiler are difficult to make due to the highly complex environment of the boiler. However, the significant improvement of the secondary protection upon the addition of Si was clear even under extremely corrosive conditions.

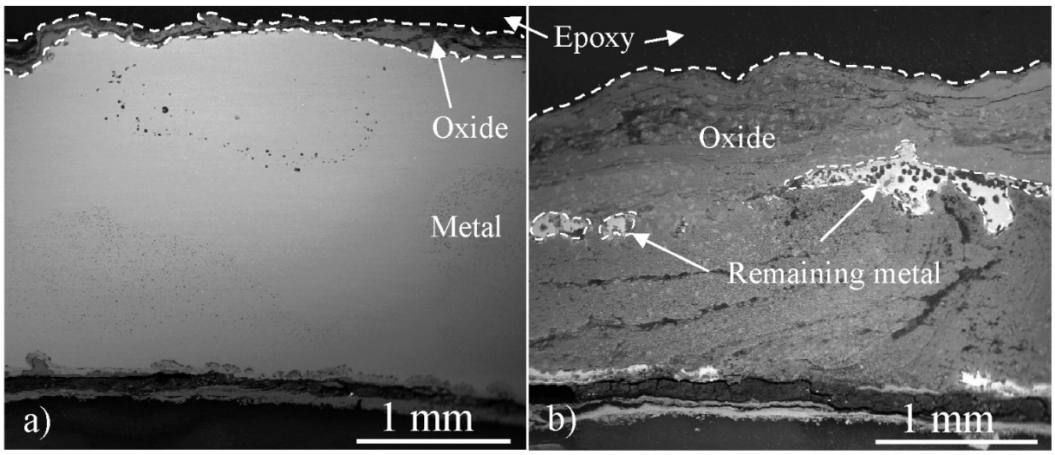

Figure 87: SEM-BSE cross-section images of the FeCrAl0Si sample ring on a) the leeward side and b) the windward side after exposure inside the waste-fired CHP boiler at a material temperature of 600 °C for 672 hours.

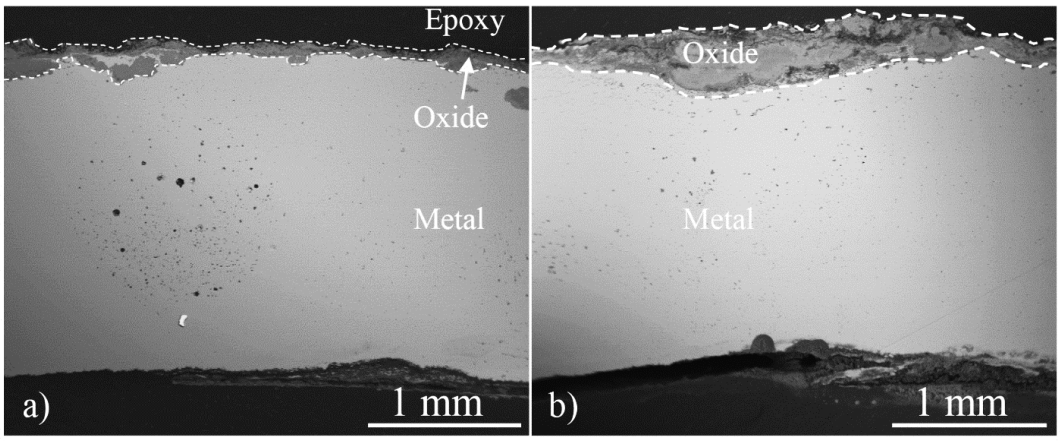

Figure 88: SEM-BSE cross-section images of the FeCrAl2Si sample ring on a) the leeward side and b) the windward side after exposure inside the waste-fired CHP boiler at a material temperature of 600 °C for 672 hours.

Increasing the Cr content of FeCrAl(Si) alloys was shown to significantly change the corrosion behavior during exposure under laboratory conditions (section 8.1.2), by reducing the corrosion rate within the secondary corrosion regime. The FeCrAlSi alloys displayed drastically reduced material degradation with an increase in Cr content when exposed inside the waste-fired boiler, see Figure 89. The Fe5CrAlSi sample ring displayed an average material loss corresponding to about 9 mm/year, while the alloys with Cr content ≥15 wt% displayed a significantly lower average material loss corresponding to 0.6-0.9 mm/year. All alloys exhibited higher material loss on the windward side in comparison to the leeward side. However, the accelerated material loss on the windward side was more pronounced with higher Cr content in the alloy.

Part of the Fe20CrAlSi sample ring cracked and detached during removal from the sample probe, as shown by the missing data points in Figure 89. This indicates that the elevated Cr content caused embrittlement since this did not occur for any of the other alloys. The combined detrimental effect of Cr, Al and Si on the mechanical properties of steels has been mentioned throughout this thesis and was one of the main reasons to keep the Cr and Al content relatively lean, especially for Si-containing alloys. However, results have not demonstrated this until now. The embrittlement of alloys with elevated Cr and Si content at high temperatures has been attributed to rapid formation of the brittle σ-phase [26]. The formation of σ-phase was also discussed in section 8.1.2 in relation to the increased grain boundary attack found on alloys with elevated Cr content when exposed to oxidizing environments in the presence of KCl. However, similar to the laboratory studies no σ-phase was found along the grain boundaries, as expected at this relatively low temperature.

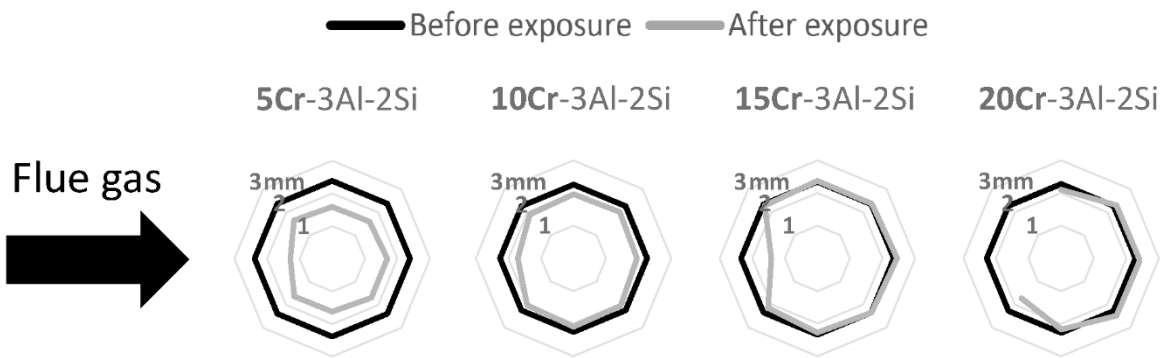

Figure 89: Radar diagrams displaying the material loss around the FeCrAlSi model alloy sample rings with varying Cr content after exposure inside the waste-fired CHP boiler at a material temperature of 600 °C for 672 hours. The arrow on the left illustrates the direction of the flue gas in relation to the sample rings.

Roughly 600 µm and 800 µm thick iron-rich oxide scales were found on the leeward and windward side of the Fe5CrAlSi sample ring, respectively, see Figure 90. The oxide scale formation originating from the steam side (bottom part of the ring) was not considered in the material loss measurements. Metal chlorides were observed at various positions around the sample ring, see Figure 90a. The metal chlorides observed in the oxide scale of the Fe5CrAlSi sample ring are not only formed close to the oxide/metal interface but are distributed evenly within the scale. Their influence on the protectiveness of the oxide is not clear.

A 10-20 µm thick iron-rich oxide scale was found on the majority of the Fe15CrAlSi sample ring, see Figure 91a. The elevated material degradation found on the windward side displayed an undulating nature and reached depths of up to 700 µm, see Figure 91b. The corrosion front was also found to be highly enriched in Cl, which indicates the presence of metal chlorides.

The Fe20CrAlSi alloy exhibited only minor material loss in the remaining part of the sample ring, and no oxide scale was found with SEM analysis on the majority of the sample ring. A multi-layered oxide scale, consisting of inward- and outward-growing scales, was found seemingly incorporated into remaining KCl-rich deposit, see Figure 92. A Cl-rich layer was found underneath the oxide scale and displayed characteristics similar to the ones found on the windward side on the Fe15CrAlSi sample ring. Similar Cl-rich layers were observed on about 50% of the Fe20CrAlSi sample ring, but no oxide scale was found in these areas. Similar to FeCrAl0Si and FeCrAl2Si, neither of the alloys displayed a multi-layered scale, except Fe20CrAlSi, indicating that the outward-growing scale might have detached along with the deposit during handling of the samples.

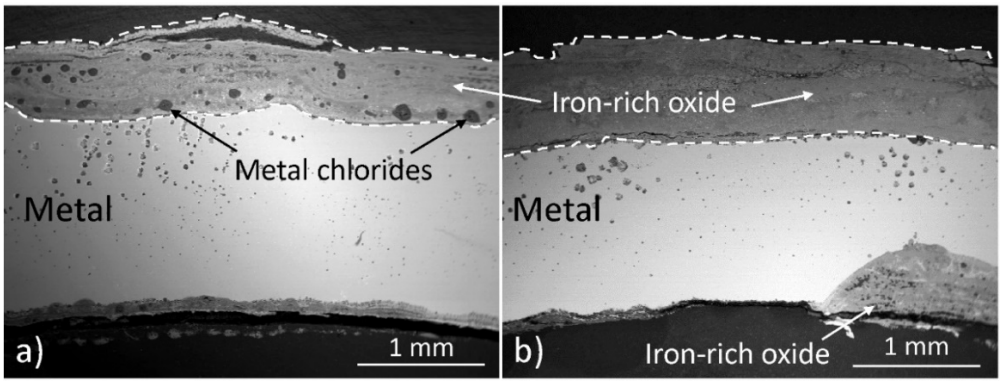

Figure 90: SEM-BSE cross-section images of the Fe5CrAlSi sample ring on a) the leeward side and b) the windward side after exposure inside the waste-fired CHP boiler at a material temperature of 600 °C for 672 hours.

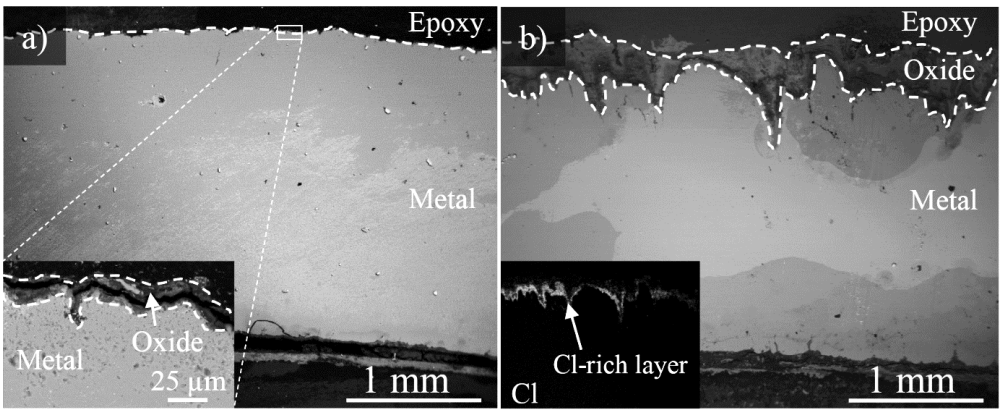

Figure 91: SEM-BSE cross-section images of the Fe15CrAlSi sample ring on a) the leeward side and b) the windward side after exposure inside the waste-fired CHP boiler at a material temperature of 600 °C for 672 hours. An EDX-map for Cl is shown in the bottom left corner of b).

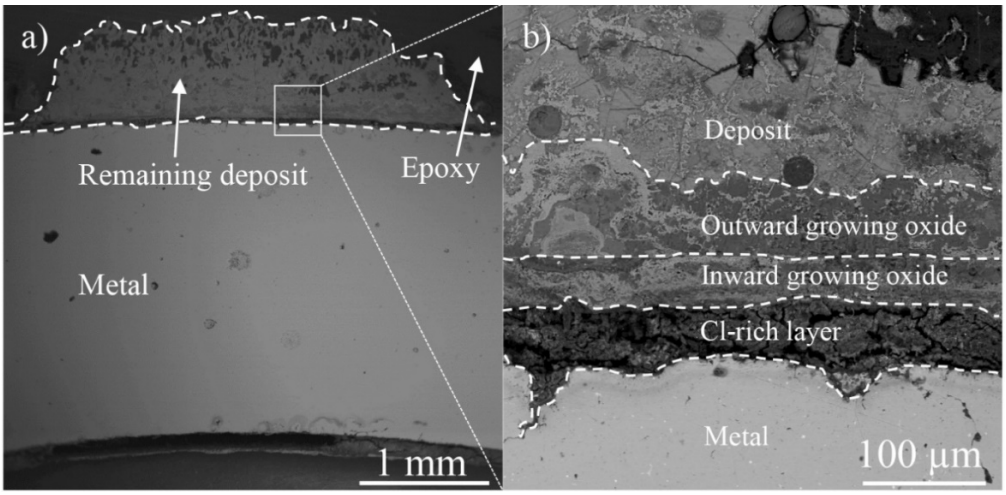

Figure 92: SEM-BSE cross-section images of the Fe20CrAlSi sample ring at the leeward side after exposure in the waste-fired CHP boiler at a material temperature of 600 °C for 672 hours.

The corrosion resistance of a 16Mo3 sample ring overlay welded with IN625 was investigated in addition to the FeCrAl model alloys. IN625 has been exposed in similar field studies due to its excellent corrosion resistance [72, 145, 160-162] and can therefore act as a reference to gage the performance of the FeCrAl model alloys. IN625 also acts as an important link between the present laboratory studies of overlay welded alloys and the performance of this type of coating in the field. No material loss measurements were performed on the IN625/16Mo3 sample ring due to the undulating nature of the overlay welding. However, the oxide thickness serves as a strong indication of the magnitude of the material loss. A roughly 150 µm thick Ni-rich oxide scale was observed on the leeward side on the IN625 sample, while the oxide scales (also Ni-rich) were found to be twice as high on the windward side (300 µm), see Figure 93. Metal chlorides were found in the metal of IN625 alloy underneath the oxide scale on the windward side.

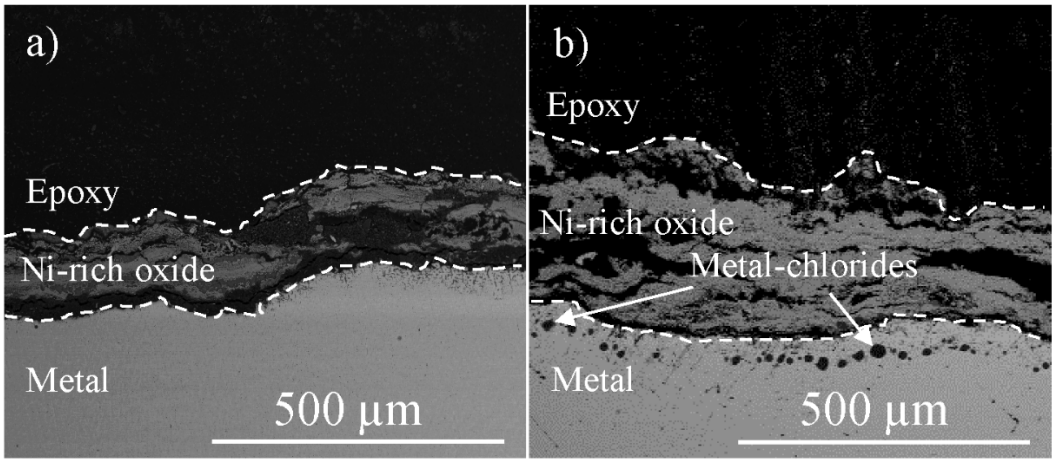

Figure 93: SEM-BSE cross-section images of the 16Mo3/IN625 sample ring on a) the leeward side and b) the windward side after exposure inside the waste-fired CHP boiler at a material temperature of 600 °C for 672 hours.

As mentioned above, the majority of the oxide scales found on the exposed samples did not display a multi-layered structure. The observed oxide scales were assumed to be inward-growing scales, and that the outward-growing scale detached along with the deposit during handling of the samples. Metal chloride formation was observed close to the metal/oxide interface on many of the samples, especially on the windward side. The FeCrAl alloys with elevated Cr content displayed an increased sensitivity to direct contact with the flue gas and more pronounced enrichment of Cl at the metal/oxide interface.

As mentioned in section 4.4.2, metal chlorides are often found in the presence of high levels of HCl(g) and/or alkali chlorides and are often associated with a severe corrosion attack [163]. The accelerated corrosion attack associated with the formation of metal chlorides is not fully understood, but has been suggested to be caused by a reduced scale/metal adhesion, resulting in crack formation and spallation of the oxide scale [84, 163, 164]. The metal chlorides have also been suggested to increase the outward flux of species through the grain boundaries, resulting in void formation and selective attack of these. The more pronounced acceleration of the corrosion attack on the windward side displayed by the FeCrAl alloys with elevated Cr content can be connected to the higher proneness of the grain boundaries to be selectively attacked in the presence of large amounts of KCl, as was shown in section 8.1.2. Nevertheless, the general corrosion attack was greatly reduced with increasing Cr content, which agrees with laboratory studies.

All investigated alloys displayed a significantly accelerated corrosion attack when exposed inside the waste-fired boiler than in the laboratory studies (sections 8.1.2 and 8.2.2). This demonstrates the high corrosivity of the waste-fired boiler. The probe exposure contributed with several important insights. Most importantly, the improved corrosion resistance within the secondary corrosion regime by increasing the Cr and Si contents in FeCrAl alloys is valid even in this very harsh environment, which confirms the relevance of the laboratory studies. The importance of balancing the beneficial and detrimental effects of elevated Cr content, both from the perspective of corrosion resistance and mechanical properties, was further emphasized by the obtained results and contributes vital understanding for material development for harsh environments.

8.3.3 Comparison: biomass- and waste-fired boilers

As mentioned in the beginning of Section 8.3, field studies are vital to verify the relevance of laboratory studies, i.e. that the same trends and concepts are valid in the intended application. Comparisons are often complicated because of significant differences in complexity. It is therefore necessary to isolate the most important differences and similarities. The concept of a primary and secondary corrosion regime has been discussed throughout this work. It is apparent from the field studies that these concepts are valid for the intended applications. In the biomass-fired boiler, in which the combustion of wood chips resulted in a relatively mild environment, the FeCrAl alloys partly or fully retained a primary protection and was further improved upon the addition of Si. After transitioning into the secondary corrosion regime, the oxide scales were found to have similar microstructure and growth rates as observed in the laboratory studies. As expected, the highly corrosive environment of the waste-fired boiler forced all alloys to transition into the secondary corrosion regime. The Cr and Si contents of the FeCrAl alloys were found to significantly reduce the material degradation, indicating an improved secondary protection even in this harsh environment. The propagation rate after transitioning into the secondary corrosion regime was significantly higher in the waste-fired boiler than inside the biomass-fired boiler and the laboratory set-up. This is attributed to the high temperature and high concentration of corrosive species in the flue gas produced in the waste-fired boiler.

9 Summary

A broad range of steels (mainly iron-based FeCr(Al) alloys) in the form of bulk materials and coatings, has been investigated in several corrosive environments, ranging from simplified laboratory environments to the complex environment of biomass- and waste-fired boilers. In this chapter, the findings of this thesis will be summarized and put into a broader perspective.

9.1 Primary and Secondary protection

The concept of a primary and a secondary protection of iron-based stainless steels at medium high temperatures (i.e. about 600 °C) has been shown to be important. This is because of the different criteria that needs to be fulfilled in order to achieve a high corrosion resistance within the primary and secondary corrosion regimes. A material with a good primary protection does not necessarily translate to a good secondary protection. This knowledge provides the potential to optimize material selection/development depending on the environment a material is intended for.

The primary protection, i.e. the ability to form and retain a protective Cr and/or Al-rich corundum type oxide (M_2O_3), is generally known to be improved by increasing the Cr and Al content. The type of primary protection (Cr-rich or Al-rich) that is necessary to prevent breakdown of the oxide scale largely depends on the surrounding environment and the temperature. In this thesis and in previous research in the literature, humid environments have been found to be challenging for FeCr(Al) alloys at medium high temperatures (around 600 °C) because of the volatilization of Cr. To retain the primary protection in these environments, the Cr and/or Al content of the alloy has to be higher to increase the reservoir of Cr or to form a more Al-rich oxide respectively. This was demonstrated by Fe18Cr6Al, which retained the primary protection in the presence of K_2CO_3. However, combinations of high Cr and Al content is often accompanied with other issues, associated with the mechanical properties of the alloy. The beneficial effect of Si on the primary protection of stainless steels has been reported in previous research. However, the mechanism behind this effect on FeCrAl alloys at medium-high temperatures (about 600 °C) has not been fully understood. Thus, the present study investigated the underlying mechanism of the effect of Si on the primary protection. Minor additions of Si were shown to significantly improve the primary protection of lean FeCrAl alloys (relatively low Cr and Al content) in both dry and wet O_2. In dry conditions, the addition of Si enabled more rapid formation of a primary protection while the addition of Si prevented breakaway oxidation, i.e. transition from primary to secondary protection, in humid conditions. Detailed microstructural investigations revealed that the concentration of Al in the corundum type oxide scale was increased while the concentration of Cr was reduced upon the addition of Si. These observations may be explained by thermodynamic calculations, indicating that the activity of Al in the alloys was increased upon addition of Si while the activity of Cr was reduced. The reduced Cr content in the oxide scale was suggested to reduce the sensitivity to Cr evaporation in the humid environment. The potential of enabling leaner FeCrAl alloys to provide a corrosion resistance similar to more highly alloyed steels is of great importance for material development in a range of different applications, such as auto thermal reforming and the Balance of Plant (BOP) components of Solid Oxide Fuel Cells (SOFC).

Even though the results showed that the primary protection can be greatly improved, various applications, such as waste-fired boilers, often exhibit extremely corrosive conditions. These environments are known to force iron-based alloys to transition into the secondary corrosion regime, i.e. the formation of an iron-rich multi-layered oxide scale, at an early stage of the material lifetime. The present study showed that while the general oxide microstructure was similar for all iron-based alloys, the secondary corrosion regime could be divided into two different behaviors, i.e. the formation of slow- or fast-growing oxide scales. Understanding the mechanisms involved in the transition from fast to slow oxide scale growth is therefore of great importance in order to identify the criteria for a

good secondary protection. The alloys that formed fast-growing oxide scales displayed similar oxidation kinetics, regardless of the alloying composition. This was attributed to their formation of a reaction zone beneath the oxide scale, consisting of Cr-rich spinel precipitates surrounded by Cr-depleted metal (iron-rich), and the subsequent formation of a porous inward-growing spinel. Thus, the rate-limiting factor of the fast-growing oxide scales is suggested to be the oxidation of iron. Upon exceeding a critical Cr content (≥25 wt%Cr for FeCr alloys, ≥18 wt%Cr for FeCrAl alloys ≥10 wt% Cr for FeCrAlSi alloys), the alloys formed slow-growing oxide scales that displayed a sub-parabolic transition at an early stage of the oxidation process. Detailed microstructural analysis suggested that the formation of slow-growing oxide scales is connected to the ability of an alloy to rapidly transition out of the stability region of the reaction zone through enrichment of Cr in the inward-growing scale. Thermodynamic calculations indicated that the stability region of the reaction zone was shifted to lower Cr concentration upon the addition of Al, which could explain why the FeCrAl alloys displayed a good secondary protection at a lower Cr content than the FeCr alloys. The addition of Si further reduced the Cr content at which FeCrAl alloys transition into a protective behavior within the secondary corrosion regime. This was not caused by the formation of a protective SiO_2 scale but is instead suggested to be connected to the incorporation of Si in the spinel. High presence of KCl was found to suppress or postpone the transition into sub-parabolic behavior and induced grain boundary attack in the more highly alloyed FeCrAlSi alloys. These findings contribute to new insights and perspectives on improving the corrosion resistance and predicting the lifetime of iron-based alloys in harsh environments.

9.2 Mitigating High Temperature Corrosion with Corrosion Resistant Coatings

Utilizing corrosion resistant coatings is an appealing method to overcome the alloying limitations of bulk materials, such as fabricability and pressure-bearing capabilities. However, as was demonstrated in this thesis, this method is associated with both pros and cons. The corrosion resistance of coatings deposited with two different methods, thermal spraying (HVAF) and overlay welding, has been investigated in harsh laboratory environments. The Ni-based HVAF-sprayed coatings displayed significantly higher degree of porosity than the overlay welded coatings. Accordingly, the former failed to protect the underlying substrate after losing the primary protection (NiCr coating) because of the diffusion of corrosive species along expanded splat boundaries. However, both the NiAl and NiCrAlY coatings seemingly retained the primary protection, which was attributed to the formation of an Al-rich oxide scale. It was suggested that the fine-grained structure and the alloying chemistry of the coatings enabled rapid transport of Al and Cr to quickly form and sustain the primary protection.

Overlay welded coatings has higher limitations than thermally sprayed coatings because of the criteria for weldability. The coating chemistries were therefore chosen to assimilate those of commercial steels and model alloys. The overlay-welded coatings were exposed to harsher conditions and for a longer time than the HVAF-sprayed coatings. As expected, all coatings transitioned into the secondary corrosion regime. However, the higher density of the overlay welded coatings prevented corrosive species to diffuse towards the underlying substrate through microstructural defects even after transitioning into the secondary regime. The leaner FeCrAl alloy coating FeCrAl197 displayed similar corrosion rate as the SVM12 reference material, i.e. rapid oxidation and the formation of a reaction zone. The inability of FeCrAl197 to fully transition into a protective behavior was attributed to the suppression by the high amount of KCl. However, the more highly alloyed steels Kanthal APMT and Inconel 625 displayed significantly reduced corrosion rates and formed Cr-enriched inward-growing scales and no reaction zone. These observations demonstrate that the suggested concept of improving the corrosion resistance within the secondary corrosion regime can be extended to even harsher environments.

9.3 High Temperature Corrosion in Biomass and Waste-fired Boilers

The validity of the concept of improving the corrosion resistance of FeCrAl alloys through optimization of the alloying composition and the potential of utilizing coatings to mitigate high temperature corrosion in harsh environments was investigated in commercial biomass- and waste-fired boilers. The corrosivity varied greatly in the two applications.

Material temperature and flue gas temperature was found to have minor influence on the corrosivity inside the biomass-fired boiler. However, SEM analysis indicated higher amounts of KCl at a material temperature of 600 °C and the low flue gas temperature position, which was attributed to a lower S/Cl ratio. The commercial stainless steels displayed relatively poor corrosion resistance inside the biomass-fired boiler and lost the primary protection both under KCl-poor and KCl-rich deposits. In contrast, the FeCrAl alloys managed to retain the primary protection under KCl-poor deposits while the addition of Si increased the resistance to KCl-rich deposits. The enhanced HVAF-sprayed FeCrAl197 coating (higher Al and Si content) was found to fully retain the primary protection (under KCl-rich deposits).

The corrosivity was significantly higher in the waste-fired boiler than in the biomass-fired boiler. This was attributed to the lower S/Cl ratio and higher flue gas temperature in the waste-fired boiler than in the biomass-fired boiler. Consequently, all alloys lost the primary protection during exposure in the waste-fired boiler. The corrosion rate was significantly accelerated at the windward side, attributed to the high temperature of the flue gas and the direct contact with corrosive species. Increasing the Cr and Si content of FeCrAl alloys was found to drastically reduce the material degradation. However, the accelerated corrosion attack on the windward side was more pronounced at elevated Cr content.

9.4 Concluding remarks

A new concept for distinguishing the corrosion behavior of iron-based alloys in mild and harsh environments at medium-high temperatures (about 600 °C) have been established in this thesis. This concept permeates all parts of the thesis, extending from simplified laboratory environments to the extremely harsh and complex environment of a waste-fired boiler. The concept of a primary and secondary protection of FeCr(Al) alloys and the improved understanding of how to influence these contributes to new perspectives in material development and the prediction of high temperature corrosion in harsh environments. The promising performance of coatings facilitates the utilization of this concept by reducing the alloying limitations of bulk materials.

10 Future Work

In the present work, the influence of different alloying elements on the corrosion resistance of FeCr(Al) alloys within the primary and secondary corrosion regimes was investigated.

Si was shown to have the most prominent influence on the primary protection, providing resistance towards the corrosive effect of humid environments which was attributed to the significantly reduced Cr content. However, the mechanism behind this and the high enrichment of Si in the oxide scale in the presence of water vapor is not fully understood. Investigating the initiation of the enrichment and the phase in which Si is present may give valuable insights into the underlying mechanism.

The corrosion behavior within the secondary regime was shown to be influenced by Cr, Al and Si in different ways. Cr was suggested to reduce the growth rate by suppressing the formation of a reaction zone, enabling the formation of a healing layer. Time resolved microstructural analysis for examining the evolution of the Cr-rich scale, from the initial oxide scale to the stabilized oxide scale (long-term) could be performed to evaluate the proposed mechanism. Al and Si were shown to reduce the amount of Cr needed for the formation of a slow-growing oxide scale within the secondary corrosion regime. While the influence of Al on the stability of phases was confirmed by thermodynamic calculations, the mechanism behind the influence of Si is not fully understood. Si in the spinel was suggested to induce cation vacancies, thereby reducing the concentration of Fe while increasing the concentration of Cr and Al. This was indicated by SEM-EDX analysis but should further investigated, utilizing thermodynamic calculations and/or Density-Functional Theory (DFT) modelling. In addition, X-ray absorption near edge structure (XANES) can be used to examine the influence of Si on the valency, lattice site occupancy and concentration of the di- and trivalent Fe-ions within the spinel crystal structure.

The corrosion resistance of various coatings and the feasibility of utilizing these for corrosion protection in harsh environments was investigated in this work. The HVAF-sprayed and overlay welded coatings displayed different pros and cons. While the former exhibited poor corrosion resistance within the secondary regime, the Al-containing coatings retained the primary protection, attributed to rapid transport of Cr and/or Al to the coating surface. Similarly, an HVAF-sprayed FeCrAl coating retained the primary protection when exposed in the biomass-fired boiler. To further test the performance of these coatings, long-term exposures and more challenging environments (waste-fired boiler) should be considered.

11 References

1. *Global Warming*. [cited 2018 05-17]; Available from: https://earthobservatory.nasa.gov/Features/GlobalWarming/page2.php.
2. J. Pettersson, *Alkali Induced High Temperature Corrosion of Stainless Steel-Experiences from Laboratory and Field*. 2008: Chalmers University of Technology.
3. *Sea level*. 2018-05-16 [cited 2018 05-17]; Available from: https://climate.nasa.gov/vital-signs/sea-level/.
4. *Extreme Weather*. [cited 2018 05-17]; Available from: https://nca2014.globalchange.gov/highlights/report-findings/extreme-weather.
5. J.J. McCarthy, *Climate change 2001: impacts, adaptation, and vulnerability: contribution of Working Group II to the third assessment report of the Intergovernmental Panel on Climate Change*. 2001: Cambridge University Press.
6. M. Parry, O. Canziani, J. Palutikof, P.J. van der Linden, and C.E. Hanson, *Climate change 2007: impacts, adaptation and vulnerability*. Vol. 4. 2007: Cambridge University Press Cambridge.
7. C.B. Field, V.R. Barros, D. Dokken, K. Mach, M. Mastrandrea, T. Bilir, M. Chatterjee, K. Ebi, Y. Estrada, and R. Genova, *IPCC, 2014: Climate Change 2014: Impacts, Adaptation, and Vulnerability. Part A: Global and Sectoral Aspects. Contribution of Working Group II to the Fifth Assessment Report of the Intergovernmental Panel on Climate Change*. 2014, Cambridge University Press, Cambridge, United Kingdom and New York, NY, USA.
8. H. Asteman, K. Segerdahl, J.E. Svensson, L.G. Johansson, M. Halvarsson, J.E. Tang, and p. trans tech, *Oxidation of stainless steel in H2O/O-2 environments - Role of chromium evaporation*, in *High Temperature Corrosion and Protection of Materials 6, Prt 1 and 2, Proceedings*, P. Steinmetz, et al., Editors. 2004, Trans Tech Publications Ltd: Zurich-Uetikon. p. 775-782.
9. J. Pettersson, N. Folkeson, L.-G. Johansson, and J.-E. Svensson, *The Effects of KCl, K2SO4 and K2CO3 on the High Temperature Corrosion of a 304-Type Austenitic Stainless Steel.* Oxidation of Metals, 2011. **76**(1): p. 93-109.
10. C. Pettersson, L.G. Johansson, and J.E. Svensson, *The Influence of Small Amounts of KCl(s) on the Initial Stages of the Corrosion of Alloy Sanicro 28 at 600 °C.* Oxidation of Metals, 2008. **70**(5): p. 241-256.
11. S. Karlsson, J. Pettersson, L.G. Johansson, and J.E. Svensson, *Alkali Induced High Temperature Corrosion of Stainless Steel: The Influence of NaCl, KCl and CaCl2.* Oxidation of Metals, 2012. **78**(1): p. 83-102.
12. P. Kofstad, *High temperature corrosion*. 1988, London; New York, N.Y.: Elsevier applied science.
13. H. Götlind, F. Liu, J.E. Svensson, M. Halvarsson, and L.G. Johansson, *The Effect of Water Vapor on the Initial Stages of Oxidation of the FeCrAl Alloy Kanthal AF at 900 °C.* Oxidation of Metals, 2007. **67**(5): p. 251-266.
14. F. Liu, H. Josefsson, J.-E. Svensson, L.-G. Johansson, and M. Halvarsson, *TEM investigation of the oxide scales formed on a FeCrAlRE alloy (Kanthal AF) at 900°C in dry O2 and O2 with 40% H2O.* Materials at High Temperatures, 2005. **22**(3-4): p. 521-526.
15. N. Israelsson, J. Engkvist, K. Hellström, M. Halvarsson, J.-E. Svensson, and L.-G. Johansson, *KCl-Induced Corrosion of an FeCrAl Alloy at 600 °C in O2 + H2O Environment: The Effect of Pre-oxidation.* Oxidation of Metals, 2015. **83**(1): p. 29-53.
16. N. Israelsson, K. Hellström, J.-E. Svensson, and L.-G. Johansson, *KCl-Induced Corrosion of the FeCrAl Alloy Kanthal ® AF at 600 °C and the Effect of H2O.* Oxidation of Metals, 2015. **83**(1): p. 1-27.
17. H. Josefsson, F. Liu, J.E. Svensson, M. Halvarsson, and L.G. Johansson, *Oxidation of FeCrAl alloys at 500–900°C in dry O2.* Materials and Corrosion, 2005. **56**(11): p. 801-805.

18. A. Persdotter, J. Eklund, J. Liske, and T. Jonsson, *Beyond Breakaway Corrosion - Influence of Chromium, Nickel and Aluminium on Corrosion of Iron-based Alloys at 600 ◦C.* Corrosion Science, 2020: p. 108961.
19. T. Jonsson, S. Canovic, F. Liu, H. Asteman, J.E. Svensson, L.G. Johansson, and M. Halvarsson, *Microstructural investigation of the effect of water vapour on the oxidation of alloy 353 MA in oxygen at 700 and 900°C.* Materials at High Temperatures, 2005. **22**(3-4): p. 231-243.
20. S.N. Basu and G.J. Yurek, *Effect of alloy grain size and silicon content on the oxidation of austenitic Fe-Cr-Ni-Mn-Si alloys in pure O2.* Oxidation of Metals, 1991. **36**(3): p. 281-315.
21. Y. Wouters, G. Bamba, A. Galerie, M. Mermoux, and J.-P. Petit, *Oxygen and Water Vapour Oxidation of 15Cr Ferritic Stainless Steels with Different Silicon Contents.* Materials Science Forum, 2004. **461-464**: p. pp. 839-848.
22. T.D. Nguyen, J. Zhang, and D.J. Young, *Effects of Silicon and Water Vapour on Corrosion of Fe–20Cr and Fe–20Cr–20Ni Alloys in CO2 at 650 °C.* Oxidation of Metals, 2017. **87**(3): p. 541-573.
23. D.P. Whittle and J. Stringer, *Improvements in High Temperature Oxidation Resistance by Additions of Reactive Elements or Oxide Dispersions.* Philosophical Transactions of the Royal Society of London. Series A, Mathematical and Physical Sciences, 1980. **295**(1413): p. 309-329.
24. B.A. Pint, *Progress in understanding the reactive element effect since the Whittle and Stringer literature review*. 2001. 9-19.
25. D. Naumenko, B.A. Pint, and W.J. Quadakkers, *Current Thoughts on Reactive Element Effects in Alumina-Forming Systems: In Memory of John Stringer.* Oxidation of Metals, 2016. **86**(1): p. 1-43.
26. C.-C. Hsieh and W. Wu, *Overview of Intermetallic Sigma () Phase Precipitation in Stainless Steels.* ISRN Metallurgy, 2012. **2012**: p. 16.
27. S. Chen and L. Rong, *Effect of silicon on the microstructure and mechanical properties of reduced activation ferritic/martensitic steel.* Journal of Nuclear Materials, 2015. **459**: p. 13-19.
28. L. Song, E. Guo, L. Wang, and D. Liu, *Effects of Silicon on Mechanical Properties and Fracture Toughness of Heavy-Section Ductile Cast Iron*. Vol. 5. 2015. 150-161.
29. E. Sadeghimeresht, N. Markocsan, and P. Nylén, *Microstructural and electrochemical characterization of Ni-based bi-layer coatings produced by the HVAF process.* Surface and Coatings Technology, 2016. **304**: p. 606-619.
30. E. Sadeghimeresht, J. Eklund, J. Phother Simon, J. Liske, N. Markocsan, and S.V. Joshi, *Effect of water vapor on the oxidation behavior of HVAF-sprayed NiCr and NiCrAlY coatings*. 2018.
31. G.J. Van Wylen, R.E. Sonntag, and C. Borgnakke, *Fundamentals of classical thermodynamics*. Vol. 1. 1994: John Wiley & Sons.
32. C.L. Senior, A.F. Sarofim, T. Zeng, J.J. Helble, and R. Mamani-Paco, *Gas-phase transformations of mercury in coal-fired power plants.* Fuel Processing Technology, 2000. **63**(2): p. 197-213.
33. S. Karlsson, L.-E. Åmand, and J. Liske, *Reducing high-temperature corrosion on high-alloyed stainless steel superheaters by co-combustion of municipal sewage sludge in a fluidised bed boiler.* Fuel, 2015. **139**: p. 482-493.
34. H. Kassman, J. Pettersson, B.-M. Steenari, and L.-E. Åmand, *Two strategies to reduce gaseous KCl and chlorine in deposits during biomass combustion — injection of ammonium sulphate and co-combustion with peat.* Fuel Processing Technology, 2013. **105**: p. 170-180.
35. H.P. Nielsen, F.J. Frandsen, K. Dam-Johansen, and L.L. Baxter, *The implications of chlorine-associated corrosion on the operation of biomass-fired boilers.* Progress in Energy and Combustion Science, 2000. **26**(3): p. 283-298.
36. J. Pettersson, C. Pettersson, N. Folkeson, L.G. Johansson, E. Skog, and J.E. Svensson, *The Influence of Sulfur Additions on the Corrosive Environments in a Waste-Fired CFB Boiler.* Materials Science Forum, 2006. **522-523**: p. 563-570.

37. N. Folkeson, J. Pettersson, C. Pettersson, L.G. Johansson, E. Skog, B.Å. Andersson, S. Enestam, J. Tuiremo, A. Jonasson, B. Heikne, and J.E. Svensson, *Fireside Corrosion of Stainless and Low Alloyed Steels in a Waste-Fired CFB Boiler; The Effect of Adding Sulphur to the Fuel.* Materials Science Forum, 2008. **595-598**: p. 289-297.
38. J. Bott, H. Yin, J. Zhu, and S. Sridhar, *Al N formation in Fe-A l alloys in N2-O 2 atmospheres.* Materials and Corrosion, 2014. **65**(3): p. 296-304.
39. R. Prescott and M.J. Graham, *The oxidation of iron-aluminum alloys.* Oxidation of Metals, 1992. **38**(1): p. 73-87.
40. D.J. Young, *High Temperature Oxidation and Corrosion of Metals*. 2008: Elsevier.
41. K.G. Field, M.A. Snead, Y. Yamamoto, and K.A. Terrani, *Handbook on the Material Properties of FeCrAl Alloys for Nuclear Power Production Applications.* 2017.
42. C. Lyphout, S. Björklund, M. Karlsson, M. Runte, G. Reisel, and P. Boccaccio, *Screening Design of Supersonic Air Fuel Processing for Hard Metal Coatings.* Journal of thermal spray technology, 2014. **23**(8): p. 1323-1332.
43. T.C. Hanson, C.M. Hackett, and G.S. Settles, *Independent control of HVOF particle velocity and temperature.* Journal of Thermal Spray Technology, 2002. **11**(1): p. 75-85.
44. P. Fauchais, *Understanding plasma spraying.* Journal of Physics D: Applied Physics, 2004. **37**(9): p. R86.
45. Y. Kawahara, M. Nakamura, H. Tsuboi, and K. Yukawa, *Evaluation of new corrosion-resistant superheater tubing in high-efficiency waste-to-energy plants.* Corrosion, 1998. **54**(7): p. 576-589.
46. Y. Kawahara, *Application of High Temperature Corrosion-Resistant Materials and Coatings Under Severe Corrosive Environment in Waste-to-Energy Boilers.* Journal of Thermal Spray Technology, 2007. **16**(2): p. 202-213.
47. N. Birks, G.H. Meier, and F.S. Pettit, *Introduction to the high temperature oxidation of metals*. 2006: Cambridge University Press.
48. *The Ellingham diagram*. [cited 2018 06-12]; Available from: https://www.doitpoms.ac.uk/tlplib/ellingham_diagrams/ellingham.php.
49. C.W. D Jr, *Materials science and engineering: an introduction.* John Wiley & Sons. Inc.–New York, USA, 2007.
50. M.H.J. Ågren, *Diffusion and Equilibria An Advanced Course in Metallurgy*. 2002: KTH.
51. C. Wagner, *Beitrag zur theorie des anlaufvorgangs.* Zeitschrift für physikalische Chemie, 1933. **21**(1): p. 25-41.
52. D.A. Jones, *Principles and Prevention of Corrosion*. 1996: Prentice Hall.
53. T. Jonsson, H. Larsson, S. Karlsson, H. Hooshyar, M. Sattari, J. Liske, J.E. Svensson, and L.G. Johansson, *High-Temperature Oxidation of FeCr(Ni) Alloys: The Behaviour After Breakaway.* Oxidation of Metals, 2017. **87**(3-4): p. 333-341.
54. T. Jonsson, S. Karlsson, H. Hooshyar, M. Sattari, J. Liske, J.E. Svensson, and L.G. Johansson, *Oxidation After Breakdown of the Chromium-Rich Scale on Stainless Steels at High Temperature: Internal Oxidation.* Oxidation of Metals, 2016. **85**(5): p. 509-536.
55. A.S. Khanna, *Introduction to high temperature oxidation and corrosion*. 2002: ASM international.
56. E.W.A. Young, P.C.M. Stiphout, and J.H.W. de Wit, *n-Type Behavior of Chromium (III) Oxide.* Journal of The Electrochemical Society, 1985. **132**(4): p. 884-886.
57. E.J. Opila, D.L. Myers, N.S. Jacobson, I.M. Nielsen, D.F. Johnson, J.K. Olminsky, and M.D. Allendorf, *Theoretical and experimental investigation of the thermochemistry of CrO2 (OH) 2 (g).* The Journal of Physical Chemistry A, 2007. **111**(10): p. 1971-1980.
58. B.B. Ebbinghaus, *Thermodynamics of gas phase chromium species: the chromium oxides, the chromium oxyhydroxides, and volatility calculations in waste incineration processes.* Combustion and Flame, 1993. **93**(1-2): p. 119-137.
59. J.F. RADAVICH, *Effect of Silicon on High Temperature Oxidation Of Stainless Steels.* CORROSION, 1959. **15**(11): p. 73-77.

60. T. Jonsson, F. Liu, S. Canovic, H. Asteman, J.-E. Svensson, L.-G. Johansson, and M. Halvarsson, *Influence of H[sub 2]O(g) on the Oxide Microstructure of the Stainless Steel 353MA at 900°C in Oxygen*. Vol. 154. 2007.
61. T. Jonsson, F. Liu, S. Canovic, H. Asteman, J.-E. Svensson, L.-G. Johansson, and M. Halvarsson, *Microstructural Investigation of the Effect of Water Vapour on the Oxidation of the Si-Containing FeCrNi Steel 353MA at 900 (Degree Sign) C in Oxygen.* Meeting Abstracts, 2006. **MA2006-02**(18): p. 949.
62. A. Zahs, M. Spiegel, and H.J. Grabke, *Chloridation and oxidation of iron, chromium, nickel and their alloys in chloridizing and oxidizing atmospheres at 400–700°C.* Corrosion Science, 2000. **42**(6): p. 1093-1122.
63. H. Asteman, J.E. Svensson, L.G. Johansson, and M. Norell, *Indication of Chromium Oxide Hydroxide Evaporation During Oxidation of 304L at 873 K in the Presence of 10% Water Vapor.* Oxidation of Metals, 1999. **52**(1): p. 95-111.
64. H. Asteman, J.E. Svensson, and L.G. Johansson, *Evidence for Chromium Evaporation Influencing the Oxidation of 304L: The Effect of Temperature and Flow Rate.* Oxidation of Metals, 2002. **57**(3): p. 193-216.
65. J. Pettersson, H. Asteman, J.E. Svensson, and L.G. Johansson, *KCl Induced Corrosion of a 304-type Austenitic Stainless Steel at 600°C; The Role of Potassium.* Oxidation of Metals, 2005. **64**(1-2): p. 23-41.
66. S. Karlsson, J. Pettersson, L.-G. Johansson, and J.-E. Svensson, *Alkali Induced High Temperature Corrosion of Stainless Steel: The Influence of NaCl, KCl and CaCl2.* Oxidation of Metals, 2012. **78**(1): p. 83-102.
67. M.J. McNallan, W.W. Liang, S.H. Kim, and C.T. Kang. *ACCELERATION OF THE HIGH TEMPERATURE OXIDATION OF METALS BY CHLORINE*. in *International Corrosion Conference Series*. 1983.
68. H.J. Grabke, E. Reese, and M. Spiegel, *The effects of chlorides, hydrogen chloride, and sulfur dioxide in the oxidation of steels below deposits.* Corrosion Science, 1995. **37**(7): p. 1023-1043.
69. N. Folkeson, L.-G. Johansson, and J.-E. Svensson, *Initial Stages of the HCl-Induced High-Temperature Corrosion of Alloy 310.* Journal of The Electrochemical Society, 2007. **154**(9): p. C515-C521.
70. N. Folkeson, T. Jonsson, M. Halvarsson, L.G. Johansson, and J.E. Svensson, *The influence of small amounts of KCl(s) on the high temperature corrosion of a Fe-2.25Cr-1Mo steel at 400 and 500°C.* Materials and Corrosion, 2010. **62**(7): p. 606-615.
71. A.P. Sutton, *Interfaces in crystalline materials.* Monographs on the Physice and Chemistry of Materials, 1995: p. 414-423.
72. N. Henriksen, M. Montgomery, and O.H. Larsen, *High temperature corrosion in biomass-fired boilers*. 2002. 111-133.
73. N. Folkeson, *Chlorine Induced Corrosion in Biomass and Waste Fired Boilers: Laboratory and Field Investigations*. 2010: Chalmers University of Technology, Chalmers tekniska högskola. Department of Chemical Biological Engineering
74. S.C. Okoro, M. Montgomery, F.J. Frandsen, and K. Pantleon, *Time and Temperature Effects on Alkali Chloride Induced High Temperature Corrosion of Superheaters during Biomass Firing.* Energy & Fuels, 2018. **32**(7): p. 7991-7999.
75. P. Steinmetz and C. Rapin, *Corrosion of Metallic Materials in Waste Incinerators.* Materials Science Forum, 1997. **251-254**: p. 505-518.
76. J. Eklund, M.D. Paz, B. Jönsson, J. Liske, J.-E. Svensson, and T. Jonsson, *Field exposure of FeCrAl model alloys in a waste-fired boiler at 600°C: The influence of Cr and Si on the corrosion behaviour.* 2019. **70**(8): p. 1476-1485.

77. J. Eklund, B. Jönsson, A. Persdotter, J. Liske, J.E. Svensson, and T. Jonsson, *The influence of silicon on the corrosion properties of FeCrAl model alloys in oxidizing environments at 600 °C.* Corrosion Science, 2018. **144**: p. 266-276.
78. A. Persdotter, J. Eklund, J. Liske, and T. Jonsson, *Beyond breakaway corrosion - Influence of Cr, Ni and Al on corrosion of Fe-based alloys at 600 °C.* Corrosion Science, Accepted.
79. J. Eklund, B. Jönsson, J. Liske, J.-E. Svensson, and T. Jonsson, *High temperature corrosion of Si-containing FeCrAl alloys in the presence of water vapour and KCl at 600 °C – The influence of chromium content*. Manuscript to be submitted.
80. J.O. Andersson, T. Helander, L.H. Hoglund, P.F. Shi, and B. Sundman, *THERMO-CALC & DICTRA, computational tools for materials science.* Calphad-Computer Coupling of Phase Diagrams and Thermochemistry, 2002. **26**(2): p. 273-312.
81. H. Larsson and A. Engstrom, *A homogenization approach to diffusion simulations applied to alpha+gamma Fe-Cr-Ni diffusion couples.* Acta Materialia, 2006. **54**(9): p. 2431-2439.
82. H. Larsson and L. Hoglund, *Multiphase diffusion simulations in 1D using the DICTRA homogenization model.* Calphad-Computer Coupling of Phase Diagrams and Thermochemistry, 2009. **33**(3): p. 495-501.
83. S. Bigdeli, L. Kjellqvist, R. Naraghi, L. Höglund, H. Larsson, and T. Jonsson, *Strategies for high-temperature corrosion simulations of Fe-based alloys using the Calphad approach - Part I*, in *Journal of phase equilibria and diffusion*. Submitted.
84. A. Persdotter, M. Sattari, E. Larsson, M.A. Olivas Ogaz, J. Liske, and T. Jonsson, *Oxidation of Fe-2.25Cr-1Mo in presence of KCl(s) at 400 °C – Crack formation and its influence on oxidation kinetics.* Corrosion Science, 2020. **163**: p. 108234.
85. M.D. Paz, J. Phother, T. Jonsson, and L. Mikkelsen, *Increased steam temperature with Steamboost superheater - The effect of the combustion in deposits and high temperature corrosion*, in *Nordic Flame Days 2017*. 2017: Stockholm.
86. M.D. Paz, *Increased steam temperature with Steamboost superheater in grate fired boilers – linking deposit formation and high temperature corrosion*, in *Impacts of Fuel Quality on Power Production*. 2016: Prague.
87. T. Jonsson, *Microscopy of high temperature oxidation of iron and some stainless steels*. 2007: Chalmers University of Technology.
88. J. Goldstein, D. Newbury, D. Joy, C. Lyman, P. Echlin, E. Lifshin, L. Sawyer, and J. Michael, *Scanning electron microscopy and x-ray microanalysis. Kluwwer Academic*. 2003, Plenum Publishers: New York, etc.
89. D.L. Barr and W.L. Brown, *A channel plate detector for electron backscatter diffraction.* Review of scientific instruments, 1995. **66**(6): p. 3480-3482.
90. B.D. Cullity, *Elements of X-ray Diffraction.*
91. L. Kaufman and J. Ågren, *CALPHAD, first and second generation–Birth of the materials genome.* Scripta Materialia, 2014. **70**: p. 3-6.
92. H. Larsson, T. Jonsson, R. Naraghi, Y. Gong, R.C. Reed, and J. Ågren, *Oxidation of iron at 600 °C – experiments and simulations.* Materials and Corrosion, 2016. **68**(2): p. 133-142.
93. S. Hallström, M. Halvarsson, L. Höglund, T. Jonsson, and J. Ågren, *High temperature oxidation of chromium: Kinetic modeling and microstructural investigation.* Solid State Ionics, 2013. **240**: p. 41-50.
94. S. Hallström, L. Höglund, and J. Ågren, *Modeling of diffusion in wustite and simulation of oxidation of iron at 600°C*, in *European Stainless Steel Conference Science and Market Helsinki, Finland, June 10–13, 2008*, K. Pentti and H. Staffan, Editors. 2008, Jernkontoret: Helsinki. p. 273-278.
95. J.O. Andersson, T. Helander, L. Höglund, P. Shi, and B. Sundman, *Thermo-Calc & DICTRA, computational tools for materials science.* Calphad, 2002. **26**(2): p. 273-312.
96. H. Larsson and A. Engström, *A homogenization approach to diffusion simulations applied to α+γ Fe–Cr–Ni diffusion couples.* Acta Materialia, 2006. **54**(9): p. 2431-2439.

97. J. Lim, I.S. Hwang, and J.H. Kim, *Design of alumina forming FeCrAl steels for lead or lead–bismuth cooled fast reactors.* Journal of Nuclear Materials, 2013. **441**(1): p. 650-660.
98. B. Pujilaksono, T. Jonsson, H. Heidari, M. Halvarsson, J.E. Svensson, and L.G. Johansson, *Oxidation of Binary FeCr Alloys (Fe–2.25Cr, Fe–10Cr, Fe–18Cr and Fe–25Cr) in O2 and in O2 + H2O Environment at 600 °C.* Oxidation of Metals, 2011. **75**(3): p. 183-207.
99. T.D. Nguyen, J. Zhang, and D.J. Young, *Effects of Silicon on High Temperature Corrosion of Fe–Cr and Fe–Cr–Ni Alloys in Carbon Dioxide.* Oxidation of Metals, 2014. **81**(5): p. 549-574.
100. Y. Inoue, N. Hiraide, and K. Ushioda, *Effect of Si Addition on Oxidation Behavior of Nb containing Ferritic Stainless Steel.* Tetsu-to-Hagane, 2016. **advpub**.
101. J. Engkvist, U. Bexell, M. Grehk, and M. Olsson, *High temperature oxidation of FeCrAl-alloys – influence of Al-concentration on oxide layer characteristics.* 2009. **60**(11): p. 876-881.
102. T. Sand, A. Edgren, C. Geers, V. Asokan, J. Eklund, T. Helander, J.-E. Svensson, and L.-G. Johansson, *Exploring the silicon effect on the high temperature corrosion behaviour of FeCrAl alloys in humid air.* Submitted to Oxidation of Metals, 2020.
103. A. Edgren, *High Temperature Corrosion of FeCrAl Alloys in Humidified Environment*, in *Department of Chemistry and Chemical Engineering*. 2019, Chalmers University of Technology.
104. T. Sand, C. Geers, Y. Cao, J.E. Svensson, and L.G. Johansson, *Effective Reduction of Chromium-oxy-hydroxide Evaporation from Ni-Base Alloy 690.* Oxidation of Metals, 2019. **92**(3): p. 259-279.
105. T. Jonsson, B. Pujilaksono, H. Heidari, F. Liu, J.E. Svensson, M. Halvarsson, and L.G. Johansson, *Oxidation of Fe–10Cr in O2 and in O2+H2O environment at 600°C: A microstructural investigation.* Corrosion Science, 2013. **75**: p. 326-336.
106. T. Gheno, D. Monceau, and D.J. Young, *Mechanism of breakaway oxidation of Fe–Cr and Fe–Cr–Ni alloys in dry and wet carbon dioxide.* Corrosion Science, 2012. **64**: p. 222-233.
107. T. Gheno, D. Monceau, and D.J. Young, *Kinetics of breakaway oxidation of Fe–Cr and Fe–Cr–Ni alloys in dry and wet carbon dioxide.* Corrosion Science, 2013. **77**: p. 246-256.
108. A.N. Hansson, M. Montgomery, and M.A.J. Somers, *Development of the inner oxide zone upon steam oxidation of an austenitic stainless steel.* Materials at High Temperatures, 2009. **26**(1): p. 39-44.
109. N. Otsuka, Y. Shida, and H.J.O.o.M. Fujikawa, *Internal-external transition for the oxidation of Fe-Cr-Ni austenitic stainless steels in steam.* 1989. **32**(1-2): p. 13-45.
110. B. Pujilaksono, T. Jonsson, M. Halvarsson, J.-E. Svensson, and L.-G. Johansson, *Oxidation of iron at 400–600°C in dry and wet O2.* Corrosion Science, 2010. **52**(5): p. 1560-1569.
111. N. Israelsson, *High Temperature Oxidation and Chlorination of FeCrAl Alloys*. 2014, Chalmers University of Technology.
112. S. Kiamehr, K.V. Dahl, M. Montgomery, and M.A.J. Somers, *KCl-induced high temperature corrosion of selected commercial alloys.* Materials and Corrosion, 2015. **67**(1): p. 26-38.
113. Y.S. Li, Y. Niu, and M. Spiegel, *High temperature interaction of Al/Si-modified Fe–Cr alloys with KCl.* Corrosion Science, 2007. **49**(4): p. 1799-1815.
114. Y.S. Li, M. Spiegel, and S. Shimada, *Effect of Al/Si addition on KCl induced corrosion of 9% Cr steel.* Materials Letters, 2004. **58**(29): p. 3787-3791.
115. H. Larsson, T. Jonsson, R. Naraghi, Y. Gong, R. Reed, and J. Ågren, *Oxidation of iron at 600 °C - experiments and simulations.* Materials and Corrosion, 2017. **68**: p. 133–142.
116. J. Phother-Simon, T. Jonsson, and J. Liske, *Continuous KCl addition in high temperature exposures of 304 L - A way to mimic a boiler environment.* Corrosion Science, 2020. **167**: p. 8.
117. J.P. Simon, *High Temperature Corrosion Behavior in Biomass- and Waste-Fired Boilers - Insights into catastrophic corrosion and corrosion mitigation techniques*, in *Chemistry and Chemical Engineering*. 2020, Chalmers University of Technology.
118. Y.C. Malede, K.V. Dahl, M. Montgomery, F.B. Grumsen, and J. Hald, *Effect of service exposure on KCl corrosion attack of AISI 347H FG steel.* Journal of Materials Science, 2019. **54**(21): p. 13787-13809.

119. Y.C. Malede, M. Montgomery, K.V. Dahl, and J. Hald, *Effect of microstructure on KCl corrosion attack of modified AISI 310 steel.* Materials at High Temperatures, 2018. **35**(1-3): p. 243-254.
120. P. Duhaj, J. Ivan, and E.J.J.I.S.I. Makovicky, *Sigma-phase precipitation in austenitic steels.* 1968. **206**(12): p. 1245-1251.
121. M.E. Wilms, V.J. Gadgil, J.M. Krougman, and F.P. Ijsseling, *The effect of σ-phase precipitation at 800°C on the corrosion resistance in sea-water of a high alloyed duplex stainless steel.* Corrosion Science, 1994. **36**(5): p. 871-881.
122. H.D. Solomon and T. Devine Jr. *Duplex Stainless Steels--A Tale of Two Phases*. in *Duplex stainless steels*. 1982.
123. E. Folkhard, *Welding metallurgy of stainless steels*. 2012: Springer Science & Business Media.
124. S. Mishra and R. Datta, *Embrittlement of Steel*, in *Encyclopedia of Materials: Science and Technology*, K.H.J. Buschow, et al., Editors. 2001, Elsevier: Oxford. p. 2761-2768.
125. T. Jonsson, N. Folkeson, M. Halvarsson, J.E. Svensson, and L.G. Johansson, *Microstructural Investigation of the HCl-Induced Corrosion of the Austenitic Alloy 310S (52Fe26Cr19Ni) at 500 °C.* Oxidation of Metals, 2014. **81**(5): p. 575-596.
126. J. Robertson, M.J.M.s. Manning, and technology, *Healing layer formation in Fe–Cr–Si ferritic steels.* 1989. **5**(8): p. 741-753.
127. C. Pascal, V. Parry, E. Fedorova, M. Braccini, P. Chemelle, N. Meyer, D. Oquab, D. Monceau, Y. Wouters, and M.J.C.S. Mantel, *Breakaway oxidation of austenitic stainless steels induced by alloyed sulphur.* 2015. **93**: p. 100-108.
128. A. Col, V. Parry, and C. Pascal, *Oxidation of a Fe–18Cr–8Ni austenitic stainless steel at 850°C in O2: Microstructure evolution during breakaway oxidation.* Corrosion Science, 2017. **114**: p. 17-27.
129. B. Pujilaksono, T. Jonsson, M. Halvarsson, I. Panas, J.-E. Svensson, and L.-G. Johansson, *Paralinear Oxidation of Chromium in O2 + H2O Environment at 600–700 °C.* Oxidation of Metals, 2008. **70**(3): p. 163.
130. W.H.J.T.L. Bragg, Edinburgh,, D.P. Magazine, and J.o. Science, *XXX. The structure of the spinel group of crystals.* 1915. **30**(176): p. 305-315.
131. X. Liang, Y. Zhong, S. Zhu, H. He, P. Yuan, J. Zhu, and Z. Jiang, *The valence and site occupancy of substituting metals in magnetite spinel structure Fe3−xMxO4 (M = Cr, Mn, Co and Ni) and their influence on thermal stability: An XANES and TG-DSC investigation.* Solid State Sciences, 2013. **15**: p. 115-122.
132. R. Grau-Crespo, A.Y. Al-Baitai, I. Saadoune, and N.H. De Leeuw, *Vacancy ordering and electronic structure of γ-Fe2O3(maghemite): a theoretical investigation.* Journal of Physics: Condensed Matter, 2010. **22**(25): p. 255401.
133. G.J.R.i.M. Waychunas, *Oxide Minerals: Petrologic and magnetic significance.* 1991. **25**: p. 38-46.
134. L. Bindi, W.L. Griffin, W.R. Panero, E. Sirotkina, A. Bobrov, and T. Irifune, *Synthesis of inverse ringwoodite sheds light on the subduction history of Tibetan ophiolites.* Scientific Reports, 2018. **8**(1): p. 5457.
135. D. Whittle, G. Wood, D. Evans, and D.J.A.M. Scully, *Concentration profiles in the underlying alloy during the oxidation of iron-chromium alloys.* 1967. **15**(11): p. 1747-1755.
136. D. Young, J. Zurek, L. Singheiser, and W.J.C.S. Quadakkers, *Temperature dependence of oxide scale formation on high-Cr ferritic steels in Ar–H2–H2O.* 2011. **53**(6): p. 2131-2141.
137. A. Hjörnhede and A. Nylund, *Adhesion testing of thermally sprayed and laser deposited coatings.* Surface and Coatings Technology, 2004. **184**(2): p. 208-218.
138. A. Hjörnhede, P. Sotkovszki, and A. Nylund, *Erosion-corrosion of laser and thermally deposited coatings exposed in fluidised bed combustion plants.* Materials and Corrosion, 2006. **57**(4): p. 307-322.
139. E. Sadeghimeresht, N. Markocsan, M. Huhtakangas, and S. Joshi, *Isothermal oxidation of HVAF-sprayed Ni-based chromia, alumina and mixed-oxide scale forming coatings in ambient air.* Surface and Coatings Technology, 2017. **316**: p. 10-21.

140. R. Jafari, E. Sadeghimeresht, T.S. Farahani, M. Huhtakangas, N. Markocsan, and S. Joshi, *KCl-Induced High-Temperature Corrosion Behavior of HVAF-Sprayed Ni-Based Coatings in Ambient Air.* Journal of Thermal Spray Technology, 2018. **27**(3): p. 500-511.
141. H. Kassman, M. Broström, M. Berg, and L.-E. Åmand, *Measures to reduce chlorine in deposits: Application in a large-scale circulating fluidised bed boiler firing biomass.* Fuel, 2011. **90**(4): p. 1325-1334.
142. R.F.A. Pettersson, J. Storesund, and M. Nordling, *Corrosion of overlay weld cladding in waterwalls of waste fired CFB boiler.* Corrosion Engineering, Science and Technology, 2009. **44**(3): p. 218-226.
143. Y. Kawahara, *Development and application of high-temperature corrosion-resistant materials and coatings for advanced waste-to-energy plants.* Materials at High Temperatures, 1997. **14**(3): p. 261-268.
144. M. Montgomery, O. Biede, and O.H. Larsen, *Experiences with Inconel 625 in Biomass and Waste Incineration Plants.* Materials Science Forum, 2006. **522-523**: p. 523-530.
145. Y. Alipour, P. Henderson, and P. Szakálos, *The effect of a nickel alloy coating on the corrosion of furnace wall tubes in a waste wood fired power plant.* Materials and Corrosion, 2014. **65**(2): p. 217-225.
146. Y. Alipour and P. Henderson, *Corrosion of furnace wall materials in waste-wood fired power plant.* Corrosion Engineering, Science and Technology, 2015. **50**(5): p. 355-363.
147. N. Israelsson, K.A. Unocic, K. Hellström, T. Jonsson, M. Norell, J.-E. Svensson, and L.-G. Johansson, *A Microstructural and Kinetic Investigation of the KCl-Induced Corrosion of an FeCrAl Alloy at 600 °C.* Oxidation of Metals, 2015. **84**(1): p. 105-127.
148. N. Israelsson, *High temperature oxidation and chlorination of FeCrAl alloys*. 2014, Chalmers University of Technology: Göteborg.
149. S. Kiamehr, K.V. Dahl, M. Montgomery, and M.A.J. Somers, *KCl-induced high temperature corrosion of selected commercial alloys.* Materials and Corrosion, 2015. **66**(12): p. 1414-1429.
150. J. Lehmusto, P. Yrjas, B.J. Skrifvars, and M. Hupa, *High temperature corrosion of superheater steels by KCl and K2CO3 under dry and wet conditions.* Fuel Processing Technology, 2012. **104**: p. 253-264.
151. L.N. Moskowitz, *Application of HVOF thermal spraying to solve corrosion problems in the petroleum industry—an industrial note.* Journal of Thermal Spray Technology, 1993. **2**(1): p. 21-29.
152. E. Sadeghimeresht, N. Markocsan, and P. Nylén, *Microstructural characteristics and corrosion behavior of HVAF- and HVOF-sprayed Fe-based coatings.* Surface and Coatings Technology, 2017. **318**: p. 365-373.
153. S. Kiamehr, K.V. Dahl, M. Montgomery, and M.A.J. Somers, *KCl-induced high temperature corrosion of selected commercial alloys.* Materials and Corrosion, 2016. **67**(1): p. 26-38.
154. P. Viklund, *Superheater corrosion in biomass and waste fired boilers: Characterisation, causes and prevention of chlorine-induced corrosion*. 2013, KTH Royal Institute of Technology.
155. H. Kassman, *Strategies to reduce gaseous KCl and chlorine in deposits during combustion of biomass in fluidised bed boilers*. 2012: Chalmers University of Technology.
156. K. Salmenoja, *Field and laboratory studies on chlorine-induced superheater corrosion in boilers fired with biofuels.* 2003.
157. X. Montero, A. Ishida, M. Rudolphi, H. Murakami, and M.C. Galetz, *Breakaway corrosion of austenitic steel induced by fireside corrosion.* Corrosion Science, 2020. **173**: p. 108765.
158. L. Mikkelsen, T. Jonsson, M.D. Paz, J. Eklund, J. Liske, B. Jönsson, N. Israelsson, S. Selin, J. Hernblom, J. Högberg, and J. Nockert Olovsjö, *Increased steam temperature in grate-fired boilers - Steamboost*. 2018, Energiforsk.
159. M. Broström, *Aspects of alkali chloride chemistry on deposit formation and high temperature corrosion in biomass and waste fired boilers*. 2010, Umeå universitet, Institutionen för tillämpad fysik och elektronik ….

160. M. Montgomery, O. Biede, and O.H. Larsen. *Experiences with Inconel 625 in biomass and waste incineration plants*. in *Materials science forum*. 2006. Trans Tech Publ.
161. M. Montgomery, A. Hansson, S. Jensen, T. Vilhelmsen, and N. Nielsen, *In situ corrosion testing of various nickel alloys at Måbjerg waste incineration plant.* Materials and Corrosion, 2013. **64**(1): p. 14-25.
162. M. Montgomery and O.H. Larsen. *Field Investigation of Various Weld Overlays in a Waste Incineration Plant*. in *CORROSION 2005*. 2005. NACE International.
163. E. Larsson, *The Corrosive Effect of Chlorine Containing Species on Waterwalls and Superheater Materials in Waste and Biomass-Fired Power Plants*. 2017: Chalmers University of Technology.
164. T. Jonsson, N. Folkeson, J.-E. Svensson, L.-G. Johansson, and M.J.C.S. Halvarsson, *An ESEM in situ investigation of initial stages of the KCl induced high temperature corrosion of a Fe–2.25 Cr–1Mo steel at 400 C.* 2011. **53**(6): p. 2233-2246.